The Opposing Planar Jet Oscillator

THE OPPOSING PLANAR JET OSCILLATOR

BY

ERIC SALT, B.EngM.

A THESIS

SUBMITTED TO THE DEPARTMENT OF MECHANICAL ENGINEERING

AND THE SCHOOL OF GRADUATE STUDIES

OF MCMASTER UNIVERSITY

IN PARTIAL FULFILMENT OF THE REQUIREMENTS

FOR THE DEGREE OF

DOCTOR OF PHILOSOPHY

Doctor of Philosophy (2018)   McMaster University

(Mechanical Engineering)   Hamilton, Ontario, Canada

TITLE: The Opposing Planar Jet Oscillator

AUTHOR: Eric Salt

                          B.EngM., (Mechanical Engineering)

                          McMaster University, Hamilton, Ontario, Canada

SUPERVISOR: Dr. Samir Ziada

NUMBER OF PAGES: xix, 196

To my wife, Laura

Abstract

The fundamental nature of the flow oscillations which are generated by two opposing planar jets is investigated. Particular attention is given to the underlying mechanism which sustains the oscillations over a wide range of flow parameters. The jet columns are observed to undergo large lateral deflection oscillations once in each direction per cycle, in an asymmetric manner. Extensive characterization of the jet oscillations over a wide range of flow parameters is established, including both the aeroacoustic response, as well as the unique flow features which are synchronized with the oscillations. The impingement region and circulation regions in each quadrant of the flow field are shown to play essential roles in sustaining the oscillations, as the pressurization of the impingement region causes the jets to initially deflect away from the centerline, while the low-pressure regions which form in the circulation zones drive the jet columns back towards, and ultimately across, the centerline. A number of interesting observations are made regarding the oscillation characteristics, including a dependence of the oscillation frequency on the jet aspect ratio, which helps explain much of the discrepancy in the Strouhal numbers reported in the literature to date. Furthermore, the nature of the sound-source field is investigated including the directionality of the various frequency components which are radiated.

Unique mitigation strategies of the opposing planar jet oscillations are also explored by

attempting to disrupt the circulation regions through the use of splitter plates. The oscillations are weakened considerably as the development and convection of the circulation zones is impeded. Preventing the circulation flow from interacting with the jet exit region drastically increases the effectiveness of the splitter plates, as even short splitter plates are shown to completely eliminate the oscillations. This demonstrates a very effective mitigation strategy of the opposing planar jet oscillator which is ideal for a variety of practical applications.

One of the main challenges of the current investigation into the opposing planar jet oscillator is the extent to which the detailed time-varying pressure field can be resolved. Since it is not possible to experimentally detail the time-varying pressure field of the opposing planar jets, a novel PIV-based pressure field mapping technique is developed and benchmarked. A separate apparatus consisting of a planar jet impinging on a v-shaped plate is utilized to benchmark the proposed technique. This technique effectively resolves the features of the time-varying pressure field which are synchronized with the flow oscillations and helps circumvent many of the challenges which existing PIV pressure field mapping techniques face. It also provides a valuable tool for researchers to simultaneously determine the kinematic and dynamic aspects of various flow phenomena in a variety of fields, especially those in the area of aeroacoustics and fluid-structure-interaction.

Acknowledgments

First and foremost, I owe my deepest gratitude to my supervisor and friend, Dr. Samir Ziada, who has had a profound influence in both my academic and professional career. This research would not have been possible without his continuous encouragement, support and enthusiasm, as well as his immense knowledge and experience. I would also like to thank my supervisory committee members, Dr. Marilyn Lightstone and Dr. Dave Novog, for their insightful advice and direction throughout the course of this investigation.

I am also very grateful to my wife, Laura, who has been my inspiration and motivation throughout my academic career. I am especially thankful for her support and understanding in every way possible and for being the constant joy in my life. My parents deserve special thanks for their love and support over the years. They taught me the value of education and provided me with every opportunity to succeed. To my parents-in-law, who have been there from the early years of my education, I am grateful for their guidance and unwavering support throughout the entire process.

I am also forever indebted to my colleagues in the Aeroacoustics Research Group, many of whom have become life-long friends. I am particularly thankful for their ideas, encouragement and many fruitful discussions. Despite all the late nights and early mornings in the lab, it has been a pleasure to work and collaborate with them.

Nomenclature

A_i	Amplitude of ith frequency component	P_{max}	Max pressure amplitude $[kPa]$
b	Jet spread $[mm]$	P_{rms}	RMS pressure amplitude $[kPa]$
c	Speed of sound $[m/s]$	P_{∞}	Ambient pressure $[kPa]$
f	Frequency $[Hz]$	Q	Quality factor
f_c	Convective source terms $[1/s^2]$	R	Ideal gas constant $[J/kgK]$
f_f	Fluctuating source terms $[1/s^2]$	Re	Reynolds number
f_n	Fundamental frequency $[Hz]$	S_l	Splitter length $[m]$
h	Slot width $[mm]$	S_x	Downstream location of splitter $[m]$
h_r	Spatial resolution $[mm]$	S_y	Cross-stream location of splitter $[m]$
L	Impingement length $[mm]$	St	Strouhal number
L_e	Effective impingement length $[m]$	t	Time $[s]$
$\frac{L}{h}$	Impingement ratio	T	Temperature $[K]$
M	Mach number	u	Streamwise velocity $[m/s]$
n	Integer stage number	$\overline{u_i}$	Mean component
N	Number of model frequency components	$\overline{u_s}$	Mean steady velocity $[m/s]$
p	Pressure $[kPa]$	$\overline{u_t}$	Mean transient velocity $[m/s]$
$\overline{p_s}$	Steady pressure component $[kPa]$	u_i'	Fluctuating component
P	Static pressure $[kPa]$	$\overline{u_i'^2}$	Variance of fluctuating component

$\overline{u'v'}$	Covariance of velocity components $[m^2/s^2]$
v	Cross-stream velocity $[m/s]$
V	Jet exit velocity $[m/s]$
V_{cl}	Centerline velocity $[m/s]$
w	Velocity in normal direction $[m/s]$
W	Jet span $[mm]$
$\frac{W}{h}$	Jet aspect ratio
x	Streamwise direction $[mm]$
y	Cross-stream direction $[mm]$
Y_r	Cross-stream location of circulation zone $[m]$
z	Normal direction $[mm]$
γ	Ratio of specific heats
Δt	Temporal resolution $[s]$
ϵ	RMS error
η	Isentropic efficiency of the nozzle
θ	Phase in oscillation cycle $[°]$
λ	Wavelength $[mm]$
μ	Dynamic Viscosity $[kg/m\ s]$
ρ	Density $[kg/m^3]$
τ	Oscillation period $[s]$
ϕ	Phase shift $[rad]$
ϕ_i	Phase of ith frequency component $[rad]$

Contents

List of Figures

Chapter 1

Introduction

1.1 Motivation

Impinging streams are a useful tool and have become increasingly popular among engineers in recent decades. Impinging streams, as it pertains to the current study, consists of two counter-flowing fluids which share a common axis. These streams collide with one another in a region often referred to as the *impingement plane*. The interaction of the two fluids at impingement facilitates enhanced mass and heat transfer (Tamir, 2014). The ability of these streams to create excellent mixing conditions without any mechanical input makes them ideal for a range of applications including premixed turbulent combustion (Kostiuk *et al.*, 1993b,a), impinging stream dryers (Sathapornprasath *et al.*, 2007; Kudra and Mujumdar, 2009), reaction injection molding (Santos *et al.*, 2005), a variety of chemical processing equipment (Santos and Sultan, 2013; Johnson and Wood, 2000) and gasification of fossil fuels (Wang *et al.*, 2007). Traditionally, *axisymmetric jets* have been more prominent in practice as a result of their presumed higher mass transfer rates corresponding to the high momentum
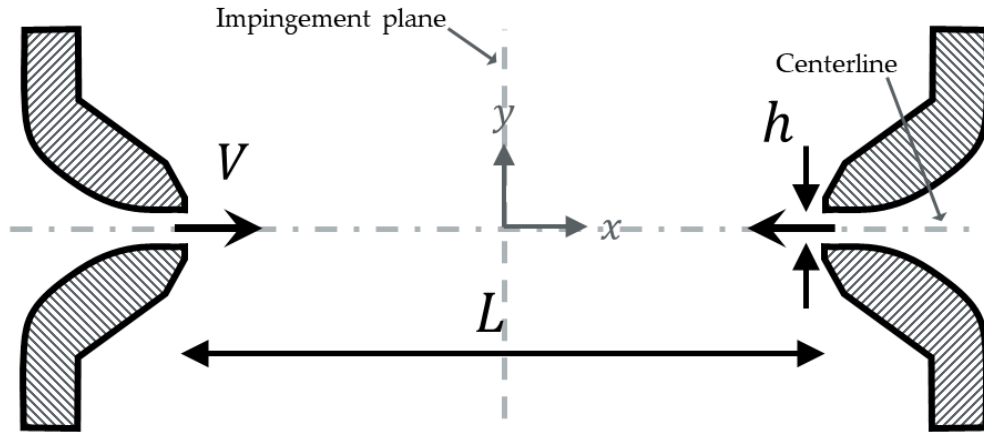
Figure 1.1: Schematic of opposing planar jets with relevant parameters

transfer from the streamwise to the cross-stream direction, as well as more substantial three-dimensional characteristics. However, recent efforts have shown that considerably higher mixing rates occur under the impingement of *planar jets* due to the well organized and persistent oscillations in the resulting flow field. Two such applications are the development of T-jet reactors as a prismatic design which replaces traditional impinging jet reactors (Santos and Sultan, 2013), as well as various forms of micromixers which take advantage of the strong self-sustained oscillations as traditional methods become less feasible (Tesař, 2009). However, opposing planar jet oscillations are sometimes not a welcome phenomenon, as they have been reported to undesirably occur in a number of applications. Even at modest Mach numbers, these oscillations can create piercing noise levels which can result in worker fatigue and violation of noise regulations. Furthermore, the presence of these oscillations in a variety of processes can generate extensive pressure pulsations which can create process inefficiencies and defects, such as overcoating near the edge of film coatings (Kim *et al.*, 2003).

The basic orientation of two opposing planar jets is shown in Figure 1.1. The spacing
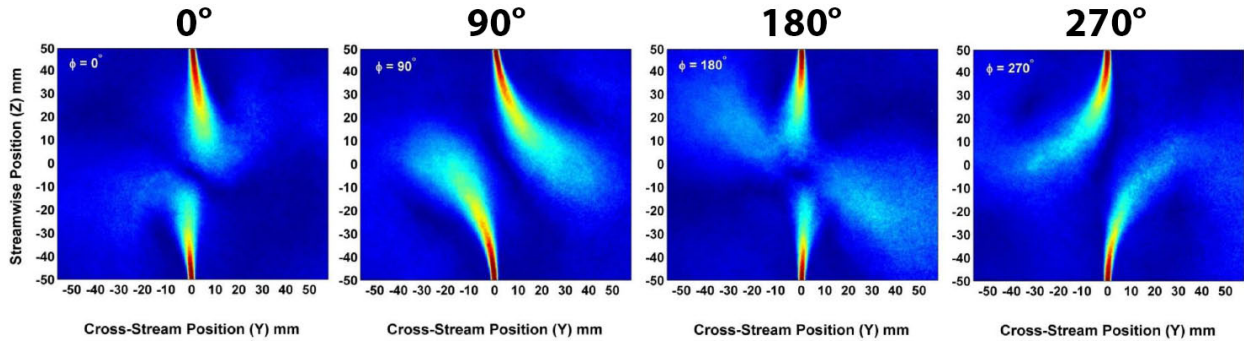
Figure 1.2: Phase-averaged velocity magnitude at four phases in the oscillation cycle of two planar opposing jets ($h = 2\ mm$, $L/h = 50$, $V = 200\ m/s$) (Hassaballa and Ziada, 2015)

between the two jet nozzles (L) will often be scaled using the jet slot width (h) hereafter referred to as the impingement ratio ($\frac{L}{h}$). Other key parameters include the velocity of the fluid exiting either jet (V) and the spanwise length of the jets (W) which is used to define the aspect ratio ($\frac{W}{h}$). Figure 1.2 shows the phase-averaged velocity field at four equally spaced instants in the oscillations cycle observed by Hassaballa and Ziada (2015). One can observe at $\theta = 0°$, the two jets are oriented along the common centerline. At this point, a high stagnation pressure region is formed at the impingement plane which pushes the two jets apart in opposite directions. At $\theta = 90°$ the two jets are at maximum deflection amplitudes and the jets begin to return back towards the centerline. At $\theta = 180°$, the jets are again oriented along the centerline, where they then deflect once again, but in the opposite directions. The underlying mechanism which causes these oscillations to occur at repeatable and well-defined frequencies is not understood, especially what causes the jets to return to the common centerline.

1.2   Scope of work

This thesis comprises a series of fundamental investigations of the opposing planar jet oscillator, with specific focus on the underlying mechanism which sustains the repeatable and robust oscillations over a wide range of flow conditions, which until now has remained largely unexplored. While the focus of the present investigations surrounds the opposing planar jet oscillator, the need for a novel experimental pressure field mapping methodology is necessary to detail the time-varying pressure field which powers these jet oscillations. Thus, an original Particle Image Velocimetry (PIV) pressure field mapping technique is first developed and benchmarked against traditional pressure measurement techniques.

1.2.1   Benchmarking PIV-based pressure field mapping technique

PIV-based pressure field mapping offers a number of unique benefits over traditional measurements techniques as a result of its non-intrusive nature and ability to resolve detailed pressure maps. However, current pressure field mapping techniques are either only capable of resolving steady pressure fields or require expensive and not readily available PIV systems to resolve time-varying characteristics. Therefore, an original PIV pressure field mapping technique is developed, capable of resolving time-varying pressure data for flow phenomena which demonstrate strong periodic features. An independent apparatus, in the *planar jet impinging on a v-shaped plate*, is used to benchmark the technique because of the presence of physical boundaries in the flow field which facilitate traditional pressure measurement techniques for purposes of validation. Furthermore, the planar jet impinging on a v-shaped plate demonstrates a number of similar flow features to the opposing planar jets, specifically low frequency deflection oscillations of the jet column. The proposed PIV pressure field

mapping technique is particularly valuable to the fields of aeroacoustics and fluid-structure-interaction, as it allows for the detailed time-varying pressure field, which is synchronized with flow oscillations, to be resolved experimentally. This technique provides not only a non-intrusive means of depicting the detailed pressure field data, but also a complete understanding of the flow behaviour as it allows the kinematic and dynamic aspects of the flow field to be resolved simultaneously. Details of the PIV measurement and pressure calculation procedures are discussed. High resolution time and spectra measurements are taken using fast-response pressure transducers at multiple locations along the plate and are subsequently used to evaluate the pressure data obtained using the PIV-based technique.

1.2.2   Investigation of the opposing planar jet oscillator

The investigation of the opposing planar jet oscillator is divided into three main tasks; characterization of the oscillations, analysis of the role of the pressure field in the self-sustaining mechanism and the development of effective oscillation mitigation strategies. The oscillations are characterized for various parametric conditions, both in terms of the acoustic response in the far-field, as well as the periodic flow conditions. The main purpose of this task is to evaluate the observed features in the oscillations over a more comprehensive range of flow parameters to help draw links between the few studies which exist in the literature on the opposing planar jet oscillation. To help resolve some of the variation in the Strouhal number over the tested parameters, a corrected impingement length is proposed which accounts for the existence of the jet cores. Interesting trends of varying Strouhal number with the jet aspect ratio helps explain some of the discrepancy in the Strouhal numbers reported in the literature for the opposing planar jet oscillator. Phase-resolved flow measurements are presented to reveal the unique features of the flow field which are synchronized with the

oscillations and provide insight into the variation in the flow field behaviour over the range of investigated parameters. Particular focus is given to the impingement region dynamics and the periodic growth and dissipation of the circulation zones in each quadrant of the flow field.

The role of the impingement region and circulation zones is further extended to discuss the role of the unsteady pressure field in the self-sustaining mechanism. Details of the pressure field calculation are provided and the phase-resolved pressure field is presented. For the first time, details of the self-sustaining mechanism which drives the jet columns back and forth throughout the oscillation cycle are presented. Additional details of the sound-source field which is generated by the fluctuation pressure are also discussed in terms of the various tones produced.

Finally, with knowledge of the essential role the circulation zones play in sustaining the jet oscillations, effective countermeasures are investigated in the form of splitter plates strategically located throughout the flow field. As the splitter plates are only located within the circulation regions, direct interaction with the jet column and the impingement region is avoided. By disrupting the development and dissipation of the circulation zones, the self-sustaining mechanism is disrupted and the resulting oscillations are shown to be significantly weakened, and even eliminated all together for some cases. This provides a practical mitigation strategy to help suppress and eliminate the oscillation in a wide range of applications where these oscillations are unwanted.

1.3   Thesis outline

This thesis contains seven chapters. Chapter 2 outlines the existing literature as it pertains to jet instabilities, self-sustained oscillations of jets, opposing planar jet oscillations, as well

as the development of PIV-based pressure field mapping. The experimental facility, as well as various equipment and methodologies, are then outlined in Chapter 3. Chapter 4 discusses the development and benchmarking of the original PIV-based pressure field mapping technique, including the evaluation of the pressure field calculations for the planar jet impinging on a v-shaped plate. The focus then shifts the opposing planar jets in Chapter 5, as the acoustic response characteristics, as well as the phase-resolved velocity and pressure fields are discussed in detail, with particular focus on how they relate to the self-sustaining mechanism. The development of mitigation strategies in the form of splitter plates situated in the circulation regions and their impact on the opposing planar jet oscillator is presented in Chapter 6. Finally, Chapter 7 summarizes the main conclusions resulting from this work and the associated contributions to the field, as well as provides recommendations for future work.

Chapter 2

Literature review

This chapter will outline the relevant literature as it pertains to the fundamental investigation of the self-sustained oscillations of opposing planar jets. The unstable nature of jet flows is a necessary prerequisite for the onset of self-sustained oscillations and as such, a broad review on the vast topic of jet instabilities will first be discussed. Even though little is known about the opposing planar jet oscillator, the state of knowledge regarding other self-sustained jet oscillators is fairly rich, such as the jet-edge, jet-plate and jet-slot. While the underlying mechanism of these other oscillators appears to be very different, knowledge of these cases will prove valuable throughout the course of the current investigation, and therefore will be discussed next. Following, the few studies which make up the current state of knowledge of the opposing planar jet oscillator will be reviewed in detail. Finally, since a novel approach to PIV-based pressure field mapping is developed in Chapter 4, a review of the existing techniques and methodologies will be examined.

2.1 Jet instabilities

The stability of a fluid flow is defined by its ability to return to its initial state, despite the influence of small disturbances. Jet flows are inherently unstable as a result of the free shear layers formed between the jet and the neighbouring fluid body. These shear layers often possess an inflection point in the mean velocity profile, which is related to the source of the instability. Linear stability theory has been extremely successful in predicting flow instabilities, including the most unstable disturbance frequency, disturbance amplification rate, wave number and the Reynolds number at which the flow becomes unstable. This is accomplished by linearizing the perturbed form of the Navier-Stokes equations (Orr-Sommerfeld equations) and using basic stability theory to observe the behaviour of the flow when a finite disturbance is introduced (Orr, 1907a,b; Sommerfield, 1908). These equations take a similar form to the wave equation when approximated for high Reynolds numbers, referred to as the Rayleigh's stability equation (Rayleigh, 1880). To analytically solve these equations, the disturbance must be assumed to either grow in space or time. While early investigations into free shear layer instability assumed temporal growth, Freymuth (1966) showed that as a result of the large disturbance amplification rates in fluid instabilities, spatial growth theory more accurately predicts the most unstable frequency, amplification rates and phase velocities of the disturbances. Therefore, the general solution to the aforementioned equations assumes the wave number is complex while the wave speed remains entirely real. Moreover, the disturbance can be determined to be stable, neutral or unstable if the imaginary component of the wave number is positive, zero or negative, respectively.

In practice, there are two separate instabilities which exist in both an axisymmetric and planar jet flow. The first of which is the *shear layer instability*, which is associated with the shear layer at the initial separation point immediately downstream of the nozzle lip and has

been shown to be related to the momentum thickness (θ_m) of the shear layer. As these initial disturbances grow and propagate downstream, they roll up into larger coherent structures which appear to be more related to the width of the jet than the momentum thickness, often referred to as the *preferred mode instability*. Sato (1960) studied the shear layer instability for a planar jet and found that the nature of the instability is strongly related to the initial conditions of the flow, more specifically the nozzle geometry. For jets which are more fully developed at the nozzle exit, usually a result of longer and more tapered nozzles, there are two well defined modes of oscillations which exist; a symmetric and an antisymmetric mode. The symmetric mode is observed closer to the nozzle exit and near the centerline, while the antisymmetric oscillations appear near the outer region of the shear layer and further downstream. The exact locations where the two modes are observed is dependent on the nozzle shape. In practice, most jet flows are created with much shorter nozzle geometries (or wide slot widths), which results in thinner shear layers. Bajaj and Garg (1977) showed that the shear layer instability in these flows agrees more with that of the hyperbolic tangent velocity profile, which is used to predict instabilities in the classical mixing layer formed between two parallel streams. For this later case, linear stability theory predicts the most unstable Strouhal number (dimensionless frequency), based on the momentum thickness, to be $St_{\theta_m} = 0.017$, which agrees very well with experimental data, as the largest oscillations were observed for Strouhal numbers from 0.012 to 0.017 for a planar jet (Gutmark and Ho, 1983).

While the behaviour of the shear layer instability appears to be predictable, the preferred mode instability is often the focus of studies pertaining to jet instabilities. Crow and Champagne (1971) first studied the preferred mode in depth, and found that the oscillations appear to be related more to the global oscillations of the jet column, and therefore is related

to the jet width (h) as a length scale and not the momentum thickness. The most unstable Strouhal number of this instability for the planar jet is usually around $St_h = 0.3$, which is approximately half of that observed for the axisymmetric jet (Ho and Huerre, 1984). However, very large scatter has been observed in the literature due to external influences and initial conditions present in each study (Gutmark and Ho, 1983). Specifically, Ho and Hsiao (1983) showed for smaller slot widths ($\frac{h}{\theta} < 140$), the velocity profile becomes more fully developed. Consequently, the scale of the momentum thickness relative to the slot width can influence the observed behaviour of the preferred mode instability. Most notably, the observed Strouhal number can be significantly smaller than predicted.

Figure 2.1 a) depicts the growth of a typical flow instability with particular focus on the amplification of the individual harmonic components at various downstream locations. While linear stability theory has been successful in predicting both of the aforementioned instabilities, it has only been able to predict the growth rates in the linear growth region, which is relatively early in the growth cycle. In this region, the disturbance grows at a constant exponential rate, however after this region the growth becomes non-linear and the harmonics and sub-harmonics begin to emerge. Specifically, at the end of the linear growth region, the fluid structures pair which form the subharmonics. This process is represented in Figure 2.1 b) by a rapid growth in the first sub-harmonic ($\frac{\beta_0}{2}$). As these structures grow, they become strongly two-dimensional and scale with the size of the shear layer (Brown and Roshko, 1974). Further downstream, the structures begin to break apart, giving rise to the different harmonics. This process continues until the flow has completely transitioned to turbulence. Husain and Hussain (1983) studied the transition process for various flow configurations, including the planar jet, and showed the transition to turbulence occurs in a very similar process, irrespective of the configuration.
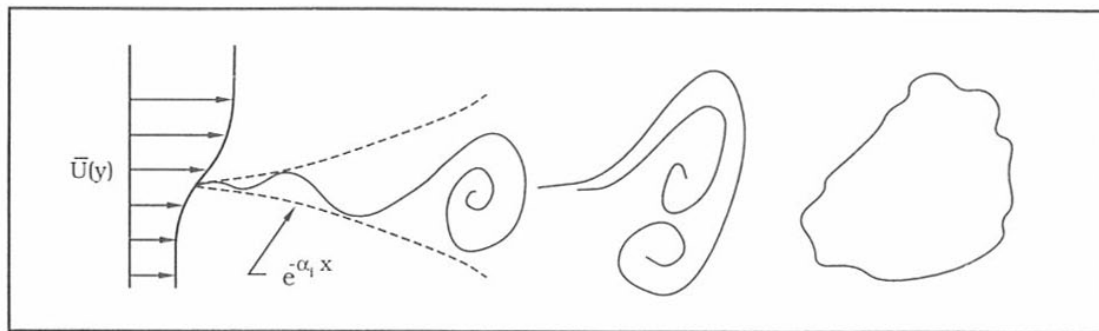
(a) Schematic illustrating essential features.
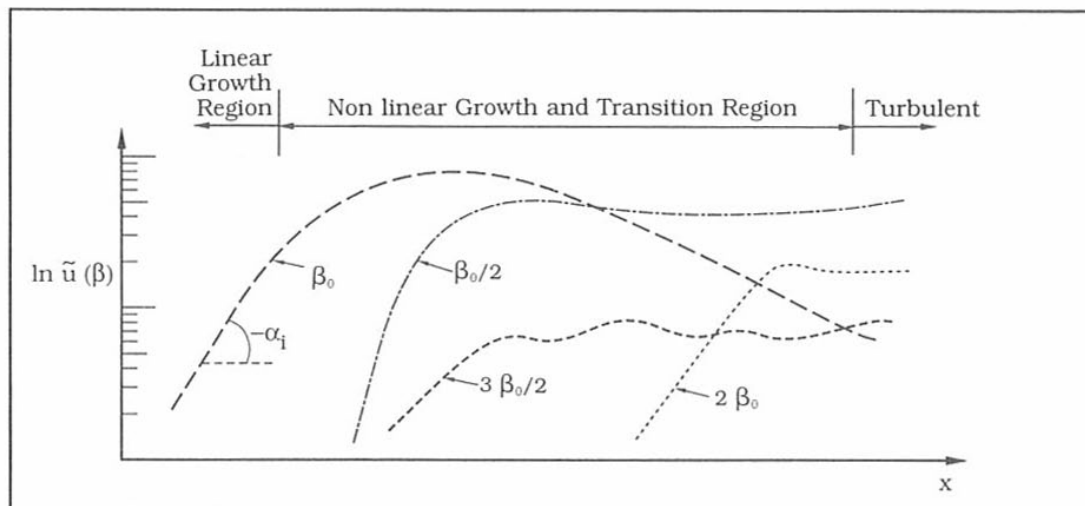
(b) Streamwise disturbance growth rates.

Figure 2.1: Disturbance growth in plane mixing layer (Lucas *et al.*, 1995)
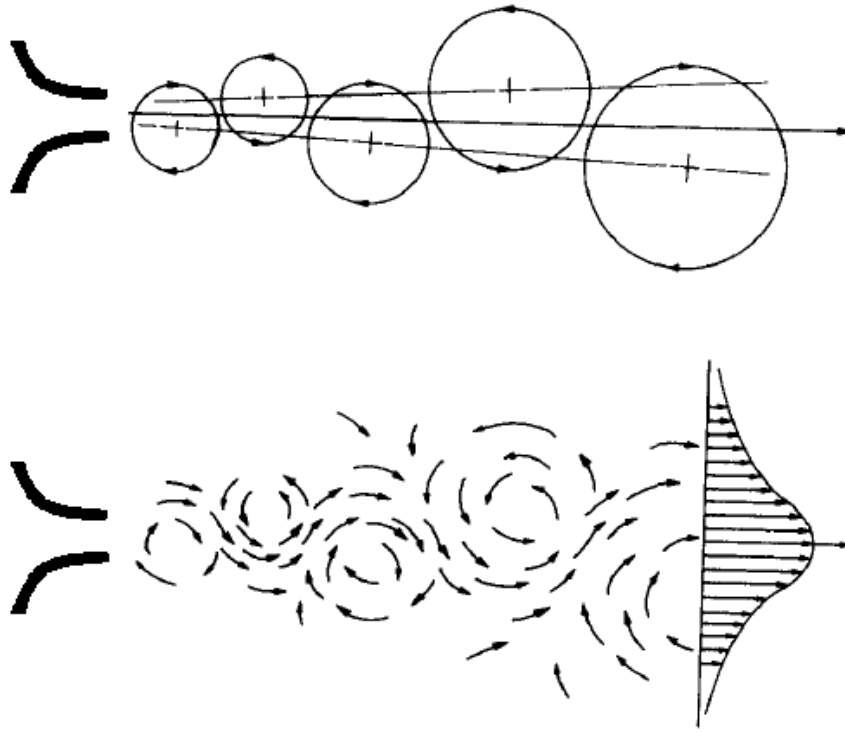
Figure 2.2: Propagation of large coherent structures which cause apparent flapping motion (Goldschmidt *et al.*, 1983)

One other instability characteristic which shall be discussed due to its remarkable similarity to the opposing planar jet oscillations is the apparent *flapping* motion the planar free jet is known to exhibit in its self-similar region. This mode of oscillation was first called flapping due to its resemblance of the flapping of a flag, but in actuality it is a byproduct of the asymmetrical propagation of large counter-rotating vortical structures on either side of the jet, as shown in Figure 2.2. While the previously discussed instabilities are present in both the axisymmetric and planar jets, the flapping motion is a product of the two-dimensionality of the flow and as such is only observed in the planar jet. The flapping motion of the planar jet was first observed by Goldschmidt and Bradshaw (1973), as they defined the motion by the strong negative correlation between the centerline velocity at a given downstream

distance and the velocity along the outer edge of the jet at the same downstream location. de Gortari and Goldschmidt (1981) performed extensive correlation measurements in a variety of configurations and confirmed the flapping like motion of the jet which produced lateral oscillations, often up to 20% of the local jet spread. While they expected this was a result of organized motion of the structures in the jet, it was not until Goldschmidt *et al.* (1983) performed extensive flow visualization of the planar jet, that it was confirmed that this motion was indeed a result of large counter-rotating coherent structures antisymmetrically oriented on either side of the jet centerline. It was later observed by Antonia *et al.* (1983) that these structures actually originate from the symmetric instability near the nozzle exit previously observed by Sato (1960). While it is not clear if the antisymmetric structures observed by Sato play a role in the flapping mode, Antonia *et al.* (1983) and Thomas and Goldschmidt (1986) both show a sudden switch from symmetric to antisymmetric orientation of the disturbances just downstream of the end of the potential core. It is conjectured in these studies that there is a roll up of these structures near the point where the shear layers on either side of the jet core intersect. This develops into the counter-rotating antisymmetric structures which create this apparent flapping motion. Thomas and Goldschmidt (1986) revealed the Strouhal number of the flapping motion continuously decreased downstream when scaled using the jet exit velocity and slot width according to $St_h = 2.43(\frac{x}{h})^{-1.5}$. However, similar to other characteristics in the self-similar region, the Strouhal number is shown to remain constant when scaled with the local centerline velocity (V_{cl}) and the local jet spread (b) as $St_b = \frac{fb}{V_{cl}} \approx 0.11$ throughout the self-similar region.

2.2   Self-sustained jet oscillations

Unstable flows, such as those discussed previously, are highly susceptible to external influences due to their inherent instability. Consequently, a disturbance introduced to the sensitive region at separation near the nozzle exit can considerably influence the behaviour of the resulting flow. More interestingly, these flows can be impacted by disturbances generated by their own downstream flow, ultimately allowing the flow to create a closed-loop feedback cycle which enhances and organizes the flow features, termed *self-sustained fluid oscillations*. Rockwell and Naudascher (1979) and Rockwell (1983) extensively reviewed much of the early work surrounding self-sustained fluid oscillations resulting from impinging shear flows. Various arrangements in which these oscillations exist are reviewed, including both jets and mixing layers (axisymmetric and planar) impinging on different downstream geometries (i.e. plates, edges, corners and slots). Irrespective of the flow conditions, there is a remarkably similar process in which these oscillations are initiated and sustained. However, it should be noted that almost all the literature related to self-sustained oscillations of jets focuses on oscillations generated by fluid flows impinging on solid bodies and not fluid flows impinging on other fluid bodies. Even though the proposed investigation pertains to the latter, it is essential to detail the former as well, as the findings may be extended to the proposed investigation. Powell (1961) was one of the first to detail the generic jet oscillator process and did so for the case of a fluid jet impinging upon an upstream facing wedge (jet-edge). From Powell's investigation, which included the periodic loading on the downstream edge and the associated sound field produced, he noted two key regions which were necessary to sustain these oscillations; a well defined separation region and an impingement region. The self-sustaining cycle begins with the phenomenon discussed in Section 2.1, where inherently unstable flows, such as the jet, are susceptible to the formation of coherent

disturbances at separation which ultimately grow at an exponential rate as they propagate downstream. The development of these disturbances into flow structures is similar to the previous discussion, until they begin to be distorted near the impingement region, followed by a complex interaction with the downstream surface. The impingement generates a distortion in the velocity, vorticity and ultimately the pressure field, which results in the propagation of a disturbance from this region, usually in the form of an acoustic wave. As this disturbance propagates upstream, it interacts with the initial separation region, in particular the sensitive shear layer. This interaction results in the formation of a new disturbance which again grows and passes downstream, thus completing the self-sustaining cycle. The presence of the feedback mechanism is essential for these oscillations to persist, as it ensures strong and well organized oscillations. Furthermore, oscillation *stages* have been observed by a number of authors, which are defined by sudden and repeatable jumps in the frequency of oscillation defined by $n = \frac{L}{\lambda} + \phi$, where n is the integer stage number, λ is the wavelength associated with the oscillation frequency, L is the impingement length and ϕ is a phase shift parameter which is specific to the initial flow conditions and impingement geometries (Ziada and Rockwell, 1982a).

Early investigations by Powell (1961) revealed that each stage of oscillation is associated with the coupling of an acoustic mode with a different hydrodynamic mode, meaning for each jump in the frequency, often an additional fluid structure is observed between the separation and impingement region, as shown in Figure 2.3. The mode which is observed is highly dependent on the velocity and impingement distance. Additionally, hysteresis is often observed, as for the exact same configuration and flow parameters, different stages may be observed depending on how the flow condition was established. Specifically, this phenomenon is often defined by the jump-up in the frequency occurring at a higher flow
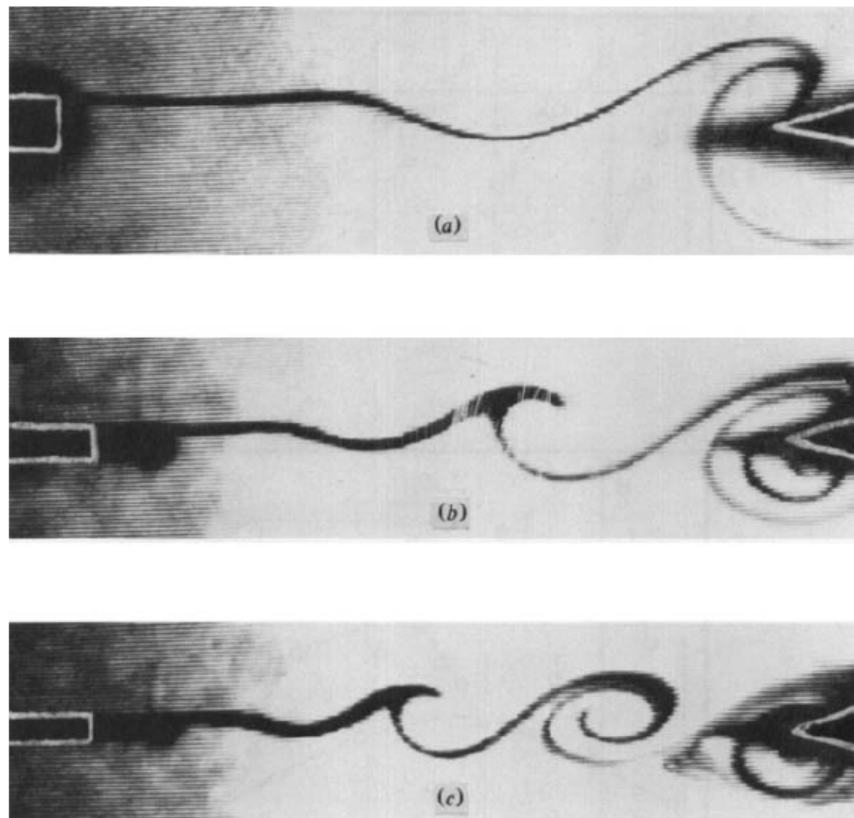
Figure 2.3: Flow visualization of the classical mixing layer-edge arrangement for stages a) $n = 1$, b) $n = 2$ and c) $n = 3$ (Ziada and Rockwell, 1982a)
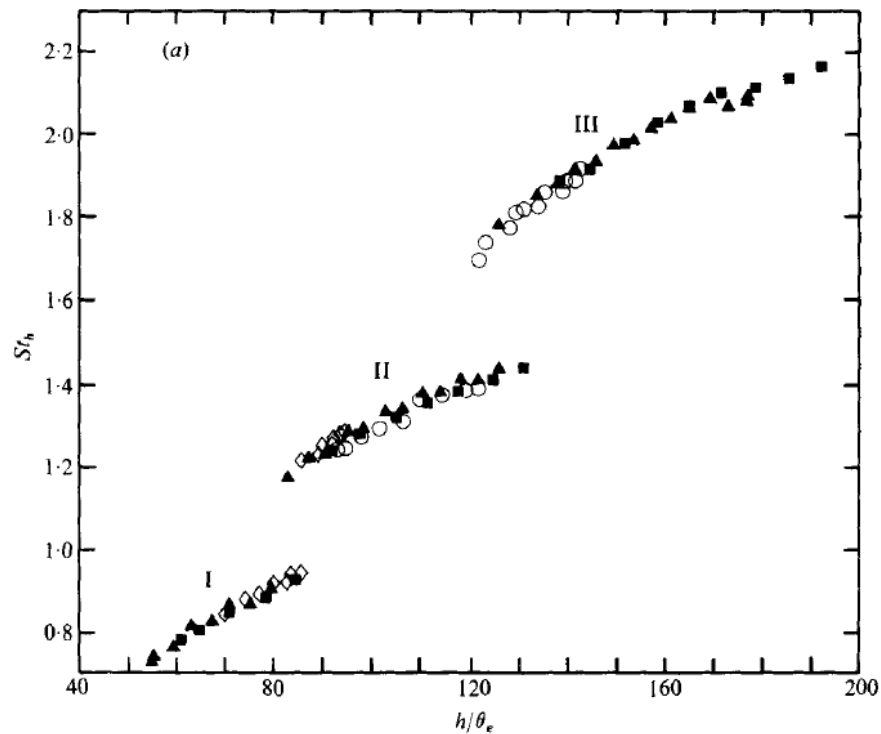
Figure 2.4: Frequency response of the self-sustaining oscillations showing jet switching (Hussain and Zaman, 1978)

velocity than the jump-down in the frequency between the same two stages. It shall be noted that the frequencies at which these oscillations occur are far below that of the original shear layer instability for a free jet, discussed earlier. Figure 2.4 shows the selective frequency behaviour of the jet-edge oscillator, as there are sudden jumps between the various stages of oscillations. This figure also depicts the hysteresis effects as the end of one stage overlaps with the onset of the subsequent stage.

The interaction of the coherent structures and the boundary at impingement was explored by Ziada and Rockwell (1982a,b) for the case of the classical mixing layer impinging on an edge. It is observed that the resulting oscillations are fairly robust, as the vortex formation and propagation from the separation region was not significantly influenced by its

18

impingement location/orientation on the edge, even though the nature of the impingement can change drastically for slight changes in the location of the edge relative to the center of the impinging vortical structure. This study also provided a clear indication of the dipole nature of the feedback source, as the perturbed streamwise velocity on either side of the shear layer created by the upstream splitter plate consistently remained 180° out of phase. Kaykayoglu and Rockwell (1986a,b) extensively detailed the unsteady pressure radiating from the impingement region (flow impinging on an edge) and noted that early separation of the flow shortly downstream of the edge resulted in a second source being generated further downstream. Therefore, the integral location of the source was further downstream than the tip of the edge, providing some reasoning for the different phase shifting for various flow configurations. Walker *et al.* (1987), and more recently Rockwell (1998), have extensively reviewed this vortex-body interaction.

Controlling the self-sustained oscillations has long been a goal among participants in the field. Staubli and Rockwell (1987) accurately controlled the amplitude and frequency of the edge oscillations in the transverse direction. The self-sustained oscillations were able to be controlled and attenuated, but only for a narrow range of excitation frequencies. More astonishingly, Ziada (1995) showed that the self-sustained oscillations can be controlled by introducing a small disturbance in the separation region in the form of a phase-shifted pressure signal from the impingement region. This was accomplished for both the jet-edge and jet-slot configurations, by focusing loud speakers upon a very small region near the jet exit. By effectively canceling the feedback acoustic wave from the impingement region, the oscillations were considerably reduced. This provides valuable insight into the nature of the mechanism and helps facilitate the development of predictive models.

There have been a number of attempts to model these self-sustained oscillations. Despite

containing a number of crude assumptions, one of the early models which accurately predicted a number of features of the oscillations, including the noise radiated at the surface, is that introduced by Holger *et al.* (1977, 1980). The model assumes the edge to be a flat plate and the periodic force is produced by a fully developed vortex sheet. While the model does prove to be successful, it shares one of the common flaws of many of the models, as it requires a number of parameters which are found empirically. The most widely accepted model is that of Crighton (1992), which is completely based on linear stability theory and does not depend on any adjustment of parameters. However, the usefulness of the model only extends to predicting frequency response characteristics and not amplitude or noise aspects.

Almost all the aforementioned studies, as they pertain to self-sustained oscillations, were performed at relatively low Mach numbers. However, the effect of Mach number, in particular in the high subsonic range, have been found to have considerable influence on the resulting oscillations. Ho and Nosseir (1981) and Nosseir and Ho (1982) for example, investigated the jet-plate oscillator over a full range of subsonic Mach numbers. The study revealed the oscillations are much stronger and narrow-banded for the high subsonic range, as compared to the lower subsonic range. It was determined that the cause of this phenomenon was the onset of resonance. More specifically, Arthurs and Ziada (2012, 2014) found it was a result of the excitation of trapped acoustic modes between the nozzle and the plate. Furthermore, the unsteady pressure field radiating, resolved by Nosseir and Ho (1982), determined that the high frequency oscillations were accompanied by a lower frequency when resonance was present. This was attributed to a 'collective interaction' process where a series of smaller vorticies formed in each shear layer rolled into each other, forming one larger coherent structure. Lucas and Rockwell (1984) and Lin and Rockwell (2001) also
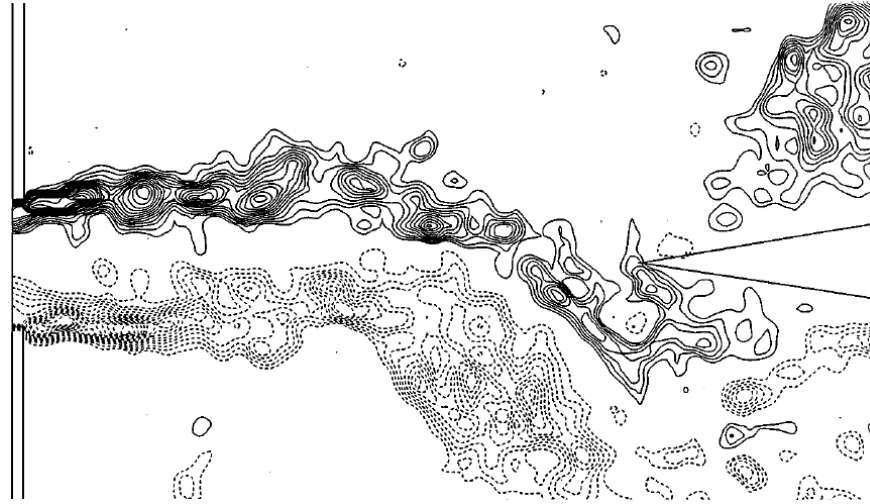
Figure 2.5: Instantaneous vorticity field showing two clear modes of instability at higher Mach numbers (Lin and Rockwell, 2001)

investigated the multi-frequency response for high Mach number jet-edge oscillations. They found that the higher frequency was consistently three times that of the lower frequency. The coalesce of vortices caused the lower frequency oscillations to be much more organized and stronger, resulting in the production of large rollers. Figure 2.5 shows an instantaneous depiction of the vorticity field for the high Mach number jet-edge oscillations. This figure shows this phenomenon as there are small vorticies which scale with the shear layer and they coalesce to form larger structures near impingement.

2.3   Oscillation of opposing planar jets

Even though opposing jets have a wide range of applications, our understanding of flow oscillations produced in these flows is relatively limited. While most of the work has been recent, the unique flow oscillations of planar opposing jets were first depicted by Denshchikov *et al.* (1978, 1983). The studies showed that the oscillations are strongly related to the

jet Reynolds number and the jet impingement distance, while other parameters such as fluid properties and jet slot widths were assumed to not be as important. The oscillation frequency was seen to increase linearly with jet exit velocity and be inversely proportional to jet separation. Furthermore, such oscillations were not observed for small impingement distances, nor small Reynolds numbers. While this study did define critical values where these oscillations were observed, later studies further investigated these values for different cases. Pawlowski *et al.* (2006) numerically investigated bifurcation and stability over a range of laminar Reynolds numbers and impingement ratios for planar opposing jets and compared it to the axisymmetric case. They noted a number of stable steady-state solutions over a range of small Reynolds numbers and impingement ratios. As well, the solutions predicted periodic flow regimes in regions similar to Denshchikov *et al.* (1978, 1983), however the dimensionless frequency of the oscillation was much larger. The study was only conducted for laminar flows ($Re_h < 1500$) and no experimental validations were reported.

More recently, Li *et al.* (2011) experimentally investigated the various flow regimes where flow oscillations are observed. Two distinct instabilities were observed, a 'horizontal instability' at small impingement distances and 'deflection oscillations' at larger impingement distances. The horizontal instability is described as random and chaotic oscillations of the impingement plane along the jets' common centerline, while the deflection oscillations pertain to the aforementioned lateral asymmetric oscillations of the two jets. The oscillation mechanism is not clear as they initially assumed the periodic asymmetric vortex structures created an oblique impact between the two jets at impingement, which ultimately caused the jets to 'deflect' away from one another. However, later work concluded that coherent structures are not a prerequisite of the deflection oscillations (Tu *et al.*, 2014a; Hassaballa and Ziada, 2015). Li *et al.* (2013) further extended this work to investigate the effect of
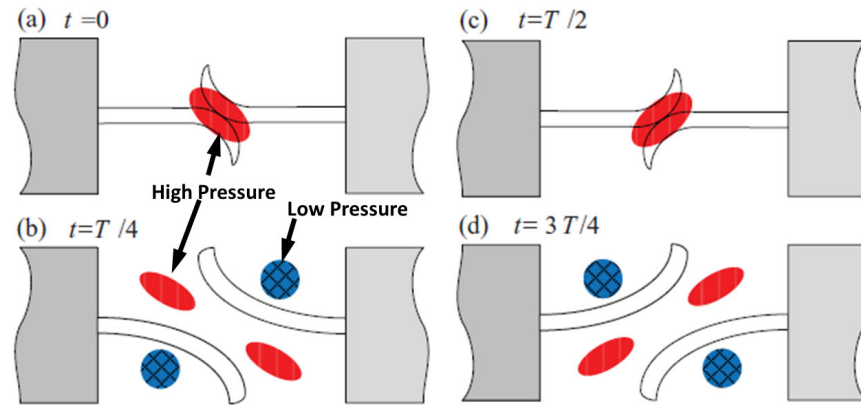
Figure 2.6: Opposing planar jet pressurizing and release process as proposed by Li *et al.* (2013)

confinement. This was done by adding 'sleeves', which extended on either side of both jets and were oriented parallel to the jets' common centerline. As the sleeves extended further, the oscillations were 'delayed', effectively decreasing the frequency of the oscillations until they disappeared entirely. The authors conjectured the oscillations were sustained based on two processes. The first was the interaction of the two jets at impingement which created a strong positive pressure region causing the jets to deflect away from one another. While the second was a negative pressure region formed near the jet exit as a result of the bowing of the jet, which effectively acted to pull the jet away from the common centerline. At this point, the positive pressure region was assumed to split into two separate regions and were ultimately emitted away from the impingement plane on an oblique trajectory. This allowed the jets to return to the common centerline, and inertia caused the jets to flip orientation as the process repeats. The process is depicted in Figure 2.6. The aforementioned sleeves were said to obstruct the pressure release process as these positive pressure regions were not able to escape. Tu *et al.* (2014a,b) further investigated the effect of confinement by containing

the flow in various directions and then shrinking the confinement. While the effect of confinement on the strength and consistency of the oscillations was not reported, the addition of large walls behind the jet exits decreased the frequency of oscillation slightly. Adding confinement in the other directions only impacted the jet oscillations when the confinement was small enough to directly impede the flow, where the frequency further decreased until the oscillations disappeared completely.

To this point, all the studies were focused on small Reynolds numbers and often investigated the effects of external influences, such as acoustic excitation and confinement. However, our understanding of the underlying mechanism responsible for such oscillations is extremely limited. Hassaballa and Ziada (2015) conducted the first PIV study on the opposed planar jets which resolved the flow field vectors, as opposed to just flow visualization. This study was conducted at higher Reynolds numbers, however very similar results were observed as compared to the aforementioned deflection oscillations, with a few exceptions. These exceptions include; the reported non-dimensional frequency (Strouhal number) of oscillation was approximately $30 - 40\%$ smaller than the previous studies, the dimensionless frequency of oscillation increased as the flow approached smaller impingement distances ($\frac{L}{h} < 30$) and finally, there was no coherent vortical structures observed in the flow. The smaller Strouhal number could be a result of a number of different reasons including Mach number effects or the larger aspect ratio. The increase in the frequency at smaller impingement distances was believed to be a result of the existence of the jet core, which has larger effects at smaller impingement distances. The final difference, the absence of propagating coherent structures in the flow, is the most interesting, as all the previous opposing planar jet studies, as well as the previous jet impingement studies (jet-plate and jet-edge) rely on the presence of these coherent structures to impinge on downstream objects and create the well-defined feedback

Table 2.1: Summary of previous investigations of opposing planar jet deflection oscillations

Study	h	L/h	W/h	Re_h	St_L	Notes
Denshchikov *et al.* (1978, 1983)	$4 - 7\ mm$	$5 - 25$	$11.4 - 20.0$	≤ 4800	0.17	water
Pawlowski *et al.* (2006)	-	$1 - 20$	-	< 1500	0.83	numerical
Li *et al.* (2011)	$10\ mm$	$1 - 20$	15	$786 - 6288$	0.17	air
Li *et al.* (2013)	$2.77\ mm$	$1 - 30$	12	$242 - 2419$	0.195	air
Tu *et al.* (2014a)	?	$2 - 40$	$1 - 20$	$16 - 5000$	0.196	air
Hassaballa and Ziada (2015)	$2\ mm$	$7 - 130$	50	$0.18 - 0.3 \times 10^5$	0.118	air

mechanism which is ultimately responsible for organized self-sustained oscillations. The absence of these features makes this mechanism unique from classical self-sustained oscillation mechanisms. A summary of the aforementioned studies and the key findings as it relates to the deflecting oscillations is reported in Table 2.1.

The only investigation which shows flow phenomena similar to the present case is that of Lin *et al.* (1993), who investigated the case of a planar jet impinging on a v-shaped plate and observed flapping of the jet column at relatively low frequencies. The oscillations do not appear to follow that of the coherent structures forming in the shear layers as the Strouhal number is shown to vary from 0.1 to 0.12 and does not appear to be highly sensitive to the plate angle. While similar Strouhal numbers and flow features to that of the opposing planar jet are observed, very little is known about the phenomenon as this is the only investigation reported in the literature. Further discussion of this jet oscillator is provided in Section 4.1.

2.4   PIV pressure field mapping

With the rapidly advancing capabilities of PIV, there has become increasing interest in estimating dynamic characteristics of flow fields, including pressure and fluid dynamic loading. This is achieved by measuring the kinematic velocities of the flow using PIV and interpreting the forces which the fluid is experiencing through the use of momentum conservation. Some

flow cases which have been the topic of such analysis includes bluff body wakes (Fujisawa *et al.*, 2005; Ragni *et al.*, 2012; Dabiri *et al.*, 2014; McClure and Yarusevych, 2017) flow over airfoils (Violato *et al.*, 2011; Villegas and Diez, 2014; Auteri *et al.*, 2015), boundary layers (Ghaemi *et al.*, 2012), flow over cavities (Liu and Katz, 2006; Murray *et al.*, 2007), surface waves (Jakobsen *et al.*, 1997; Jensen and Pedersen, 2004) and turbulent jets (Gurka *et al.*, 1999; de Kat and Ganapathisubramani, 2012). PIV-based pressure field mapping techniques replace traditional methods of measuring pressure such as pressure orifices, transducers, microphones, multi-hole pressure probes and pressure sensitive paint, each of which are unable to measure pressure away from a physical boundary or are intrusive in nature. PIV pressure field mapping offers a number of advantages over these traditional techniques as a result of its ability to experimentally realize the entire pressure field in a nonintrusive manner.

2.4.1   Methodology

In principle, PIV pressure field mapping is straight forward, as it combines the highly resolved velocity data from PIV with governing equations to determine the pressure field which is observed by the flow. Specifically, the Navier-Stokes equations provides a direct relationship between the velocity and pressure fields.

$$-\nabla p = \rho \frac{\partial U}{\partial t} + \rho \left(U \cdot \nabla \right) U - \mu \nabla^2 U \tag{2.1}$$

These equations can be rewritten in Cartesian coordinates for two-dimensional flow as,

$$\rho \left(\frac{\partial u}{\partial t} + u \frac{\partial u}{\partial x} + v \frac{\partial u}{\partial y} \right) = -\frac{\partial p}{\partial x} + \mu \left(\frac{\partial^2 u}{\partial x^2} + \frac{\partial^2 u}{\partial y^2} \right) \tag{2.2}$$

$$\rho \left(\frac{\partial v}{\partial t} + u \frac{\partial v}{\partial x} + v \frac{\partial v}{\partial y} \right) = -\frac{\partial p}{\partial y} + \mu \left(\frac{\partial^2 v}{\partial x^2} + \frac{\partial^2 v}{\partial y^2} \right) \tag{2.3}$$

By taking the divergence of the Navier-Stokes equations, one can obtain,

$$
-\left(\frac{\partial^2 p}{\partial x^2} + \frac{\partial^2 p}{\partial y^2}\right)
$$
$$
= \rho\left[\frac{\partial}{\partial t}\left(\frac{\partial u}{\partial x} + \frac{\partial v}{\partial y}\right) + u\frac{\partial}{\partial x}\left(\frac{\partial u}{\partial x} + \frac{\partial v}{\partial y}\right) + v\frac{\partial}{\partial y}\left(\frac{\partial u}{\partial x} + \frac{\partial v}{\partial y}\right)\right]
$$
$$
+ \rho\left[\left(\frac{\partial u}{\partial x}\right)^2 + 2\frac{\partial u}{\partial y}\frac{\partial v}{\partial x} + \left(\frac{\partial v}{\partial y}\right)^2\right] - \mu\left[\frac{\partial^2}{\partial x^2}\left(\frac{\partial u}{\partial x} + \frac{\partial v}{\partial y}\right) + \frac{\partial^2}{\partial y^2}\left(\frac{\partial u}{\partial x} + \frac{\partial v}{\partial y}\right)\right] \quad (2.4)
$$

For incompressible flow, each term containing $\frac{\partial u}{\partial x} + \frac{\partial v}{\partial y}$ is equal to zero. The result is the pressure Poisson equation, which is often used to calculate the pressure field from the PIV velocity data.

$$
-\nabla^2 p = \rho\left[\left(\frac{\partial u}{\partial x}\right)^2 + 2\frac{\partial u}{\partial y}\frac{\partial v}{\partial x} + \left(\frac{\partial v}{\partial y}\right)^2\right] \quad (2.5)
$$

One of the key benefits of using the pressure Poisson equation to solve for the pressure field is the absence of the temporal and viscous terms which exist in the Navier-Stokes equations. While a time and viscous dependence does not appear in Equation 2.5, it is still valid for transient and viscous flows, as these terms canceled out in the formulation and no simplifications are made. The time and viscous dependence is often incorporated through the boundary conditions, usually through the use of Neumann boundary conditions defined through the Navier-Stokes equations. While in theory PIV-based pressure field mapping is straight forward, in practice there are a number of challenges in determining the pressure field. These challenges include obtaining a sufficient sampling rate to determine the time dependence of the material derivative, minimizing the propagation of error and efficiently solving the governing equations.

2.4.2   Material derivative

While PIV provides high spatial resolution velocity data which can be used to determine the spatial gradients in Equation 2.5, current capabilities are limiting in temporal resolution as a result of the low sampling rates associated with PIV systems. As a result, much of the effort to date regarding PIV pressure field mapping has been directed towards developing various methods of dealing with the material derivative in the Navier-Stokes equations. Typically, it is either assumed that the flow is steady and the time dependence is ignored altogether, or utilize more sophisticated PIV systems and techniques which have limited capabilities and are not readily available.

There have been a number of approaches to avoid the calculation of the time-dependence of the flow field. Imaichi and Ohmi (1983), who investigated low Reynolds number Kármán vortex shedding from a cylinder in crossflow, neglected the unsteady term of the Navier-Stokes equations altogether, but noted considerable error in many of the cases as a result. Gurka *et al.* (1999) investigated both the cases of laminar pipe flow and turbulent jet flow and used Reynolds averaging of the pressure Poisson equations to determine the time-averaged mean pressure field. For the turbulent case, Reynolds averaging the pressure Poisson equation revealed,

$$-\nabla^2 \overline{p} = \rho \left[\left(\frac{\partial \overline{u}}{\partial x} \right)^2 + 2\frac{\partial \overline{u}}{\partial y}\frac{\partial \overline{v}}{\partial x} + \left(\frac{\partial \overline{v}}{\partial y} \right)^2 + \left(\frac{\partial u'}{\partial x} \right)^2 + 2\frac{\partial u'}{\partial y}\frac{\partial v'}{\partial x} + \left(\frac{\partial v'}{\partial y} \right)^2 \right] \qquad (2.6)$$

They noted using the mean and fluctuating components of the velocity data to solve the Reynolds averaged equation significantly reduced the sensitivity of the pressure measurements to the error in the PIV measurements, as well as resulted in a considerably faster processing times. Ragni *et al.* (2012) investigated the mean load from the pressure field

which acts on a rotating propeller blade and avoided calculating the time dependence by phase-locking the PIV system with the rotating blade, thus allowing the flow to be assumed to be quasi-steady.

There has been considerable effort in the literature to utilize the advancing PIV technology to improve the pressure estimation, either by using PIV systems which contain high enough sampling rates to capture time resolved velocity fields when relatively low speed flows are being considered (Ghaemi *et al.*, 2012; de Kat and Ganapathisubramani, 2012; Auteri *et al.*, 2015), or to attempt to capture four consecutive exposures in order to determine both the velocity and acceleration of the fluid particles. There have been a number of creative approaches to generating multiple exposures within short time intervals. One of the earliest techniques developed was that of Jakobsen *et al.* (1997) who developed a four-CCD camera approach to resolve four successive frames to determine the fluid forces exerted on a boundary by a surface wave. However, Jensen and Pedersen (2004) noted considerable uncertainty associated with the calibration and processing of the image sets, and thus proposed an improved two-camera approach which allowed each camera to capture two frames. Liu and Katz (2006) further reduced the error by recording four exposures of the velocity field using two "cross-correlated" cameras. The result was two sets of images with overlapping time frames which reduced the particle tracking error. Unfortunately, four exposure PIV systems still require considerable development and as a result are not widely used to date.

2.4.3   Uncertainty

Most of the discussion surrounding uncertainty of PIV pressure field mapping has pertained to the calculation of the instantaneous pressure fields, specifically the influence of the temporal and spatial resolution and the method invoked to interpret the velocity field (Lagrangian

vs. Eulerian), which both significantly influence the propagation of error in the pressure calculations. However, the error propagation is highly dependent on the flow type being considered and no one solver is best for all flow cases (Charonko *et al.*, 2010). Specifically, when the pressure Poisson equation is used, the error propagation is dominated by the error within the flow field when the domain is large and dominated by the error in the boundary conditions when the domain is small (Pan *et al.*, 2016). Furthermore, the size, shape and type of boundary conditions plays a role as well, as Neumann boundary conditions are best suited for square domains, while Dirichlet boundary conditions are best for larger aspect ratio domains. There have been few studies which specifically compare the use of Lagrangian vs Eulerian characterization of the flow field. Subsequently, there is little agreement as to which approach is best as it appears to be highly depending on the flow type being considered. Jakobsen *et al.* (1997) investigated simple two-dimensional wave phenomena and noted considerably less error when Eulerian approaches are utilized, however Violato *et al.* (2011) compared both characterization methods for more complex three-dimensional flow associated with flow around a rod-airfoil structure and noted Lagrangian resulted in less error. However, this was only true for cases with small out-of-plane velocity component, as larger out-of-plane components resulted in considerably more particle tracking error. De Kat and Van Oudheusden (2012) extensively reviewed both the Eulerian and Lagrangian approaches in an attempt to quantify the error propagation for both cases to help provide guidelines for spatial and temporal resolutions. Specifically, the error in the material derivative for Eulerian characterization is related to the PIV velocity uncertainty as,

$$\epsilon_p \propto \epsilon_u \sqrt{\frac{h_r^2}{2\Delta t^2} + |\nabla u|^2 \, h_r^2 + \frac{|u|^2}{2}} \qquad (2.7)$$

While for Lagrangian flow, the error in the material derivative is related by,

$$\epsilon_p \propto \epsilon_u \sqrt{\frac{h_r^2}{2\Delta t^2} + \frac{|\nabla u|^2 h_r^2}{2}} \tag{2.8}$$

Where, Δt is the time separation between the velocity fields, h_r is the spatial resolution of the PIV images, $|\nabla u|$ is the magnitude of the velocity gradient and ϵ_u is the error in the PIV velocity measurements. de Kat and Ganapathisubramani (2012) improved the Eulerian estimation for convective flows to determine pressure by using Taylor's Hypothesis, which is particularly useful for turbulent flow cases where the pressure fluctuations of interest are very small.

2.4.4   Numerical solver

The pressure field is obtained from PIV data by either solving the Navier-Stokes equations directly or solving the pressure Poisson equation. The error associated with the spatial integration methods needed to solve the Navier-Stokes equations is known to monotonically increase with noise and error in the velocity measurements. One of the notable advantages of using the pressure Poisson equation is its insensitivity to the random noise in the velocity data (Murai *et al.*, 2007). To solve the pressure Poisson equation, many studies utilize simple central differencing 5-point solvers (Gurka *et al.*, 1999; Fujisawa *et al.*, 2005). They noted that two key drawbacks to using pressure Poisson equation are the necessity to define boundary conditions around the entire boundary of the flow field, as well as the large number of iterations required to solve the pressure field, which is disadvantageous when there are hundreds, if not thousands, of instantaneous pressure fields to solve. As a result of the extensive number of pressure calculations required and the limited knowledge of boundary

conditions for the instantaneous pressure fields calculations, a number of approaches have been developed to improve the efficiency of the solvers. Most often these solvers surround spatial marching of the Navier-Stokes equations as a result of the reduced number of iterations required to minimize error, as well as only needing to define boundary conditions at a point or small region (Van Oudheusden, 2013). Baur and Kongeter (1999) developed an improved marching scheme to solve the pressure gradient directly by using all known neighbouring values from the current iteration and used a weighted average approach to determine the pressure at a point in space. This was achieved by starting at one end of the domain where the boundary conditions are known and spatially marching across the domain. Liu and Katz (2006) noted bias in the results based on the integration path and subsequently proposed a modified omni-directional integration approach which integrates the pressure field along arbitrary paths based on a virtual boundary. Dabiri *et al.* (2014) developed an eight integration path solver to solve the pressure Poisson equation instead, however McClure and Yarusevych (2017) reviewed various solvers and showed the eight path method had a higher error sensitivity.

With increasing capabilities of volumetric PIV techniques, pressure field mapping has also been extended to solving pressure fields in three-dimensional flow cases. In order to solve the pressure Poisson equation in three-dimensional space, the PIV system must be able to capture all three velocity components u,v and w in a plane, as well as velocity gradients of u and v in the z direction (Van Oudheusden, 2013). Therefore, stereo-PIV is not enough, as a result of the missing velocity gradients in the z direction. Often dual-planes are resolved, or tomographic-PIV is used. Violato *et al.* (2011), showed that Lagrangian characterization reduces error for three-dimensional flow, however when using thin volume tomographic PIV, there must be a dominant flow direction and the PIV measurements should be oriented

parallel to it, as significant out of plane components exacerbate the particle tracking error. However, many investigations ignore the three-dimensional effects in these types of flow, as Charonko *et al.* (2010) showed that a small out-of-plane component does not significantly influence the pressure field determination if the pressure Poisson equation is used.

2.5   Summary

As discussed previously, the opposing planar jet oscillator exhibits a number of unique features which are not observed in many well-known classical jet oscillators. In particular, the oscillation frequency is observed to be over an order of magnitude lower, there are no frequency jumps to higher harmonics and the oscillations are not synchronized with the coherent structures shedding in the jets' shear layers. Furthermore, the inherent instabilities of free jets are also associated with much higher frequencies than those observed in the current flow oscillator and do not appear to be related to the resulting oscillations. Thus, the underlying mechanism which sustains the opposing planar jet oscillations is unique and has remained largely unexplored. As such, the primary focus of this thesis is the characterization of the self-sustaining mechanism of the opposing planar jet oscillator. However, to do so, the development of an original PIV-based pressure field mapping technique is needed which allows for the time-varying pressure field of the oscillator to be detailed. While the oscillations of the current phenomenon are shown to be similar in the few existing studies, the details of the response characteristics vary slightly for each study. In particular, the reported Strouhal number varies significantly over these studies. The cause of this variation is difficult to identify, as each study investigates a different subset of flow parameters. Therefore, this thesis will present a more comprehensive parametric analysis including the effect of jet aspect ratio to help draw links between these investigations. Finally, previous investigations have shown

that the opposing planar jet oscillations are difficult to disrupt and exist over a wide range of conditions which makes them ideal for many mass and heat transfer applications. However, in many other applications of the opposing jets, these oscillations are often an undesired phenomenon. Therefore, practical mitigation strategies which preserve the impinging jet flow, but suppress the oscillation mechanism will prove valuable.

Chapter 3

Experimental apparatus and methodology

The primary focus of the current investigation is the self-sustaining oscillations which arise from two opposing planar jets. Chapter 5 investigates the underlying mechanism which is responsible for sustaining the oscillations, while Chapter 6 outlines effective countermeasures for these oscillations. However, in order to detail the time-varying pressure field which is believed to be playing an essential role in the opposing planar jet oscillator, a new PIV pressure field mapping technique is proposed and developed in Chapter 4. Due to the novel nature of the proposed technique, it is necessary to benchmark this technique against a pressure field with well-known existing fluctuating pressure measurement methodologies. Unfortunately, the existing pressure measurement methodologies cannot effectively be used to measure the pressure field associated with the opposing planar jets. This is a result of the measurement techniques being intrusive in nature, unless used to measure the pressure along a solid surface, as discussed further in Section 2.4. Therefore, an additional jet oscillator, consisting of a planar jet impinging on a v-shaped plate, is used in Chapter 4 to benchmark the proposed
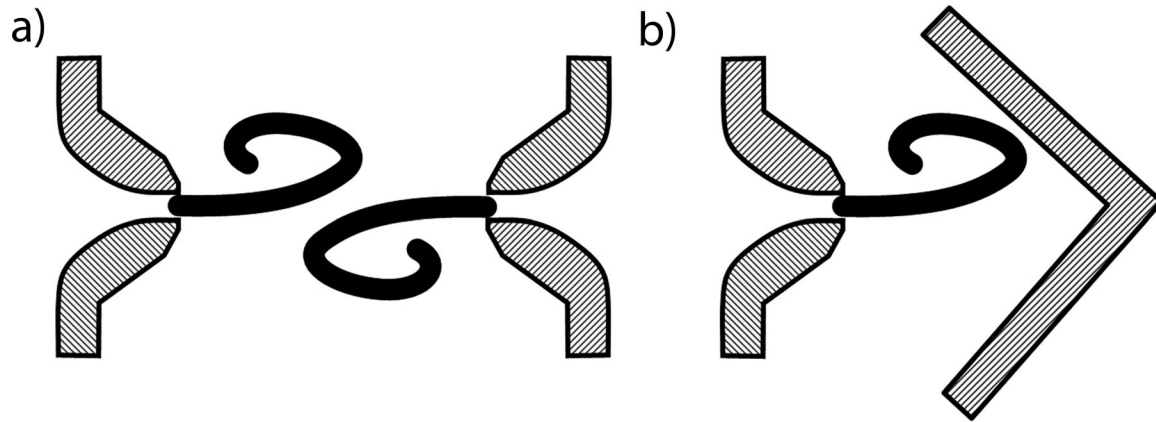
Figure 3.1: Schematic of jet deflection oscillations resulting from a) opposing planar jets and b) planar jet impinging on v-shaped plate

pressure field mapping technique. The primary reason for using this flow oscillator is the similarities in its flow field characteristics with those of the opposing planar jet oscillator, yet there exists a physical boundary in the flow field where reliable pressure measurements can be taken. These pressure measurements along the boundary can then be used to evaluate the pressure field determined using the proposed PIV-based technique. In addition to the similarity in the Strouhal number of the oscillations associated with each case, the flow characteristics are also similar, as both cases produce large lateral deflection oscillations of the jet columns, once in each direction per oscillation cycle. Figure 3.1 shows schematics of the jet deflection oscillations which arise for both the opposing planar jets and the planar jet impinging on a v-shaped plate. Both cases also produce strong circulation zones on either side of the jet columns, which synchronously grow and shed with the deflection oscillations. These circulation zones will later be shown to be an essential feature in sustaining the oscillations.

The experimental apparatus used to investigate both the opposing planar jets and the planar jet impinging on v-shaped plate will now be discussed, with particular focus on the
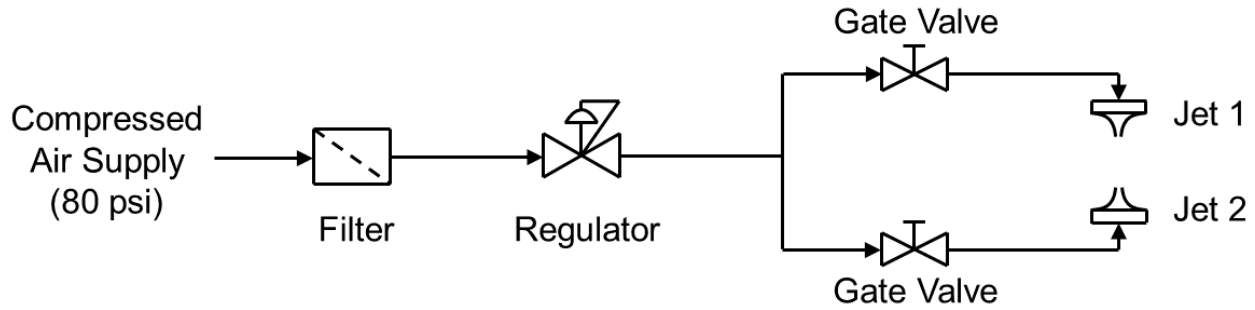
Figure 3.2: Schematic of air supply pipeline

design of the planar jets and capacity to vary relevant study parameters. Following will be a discussion of the equipment and methodologies used to measure pressure and flow-field characteristics. In addition, Chapter 4 will provide an in-depth discussion of the PIV-based pressure mapping technique used to investigate the time-varying pressure fields. While uncertainties are discussed in the current chapter, a detailed analysis of the uncertainties in each measurement is presented in Appendix A.

3.1   Experimental facility

3.1.1   Planar jet design

The planar jets are supplied with air through the physical plant at McMaster University via a 2" pipeline which supplies compressed air at 80 *psi*. As shown in Figure 3.2, the air is filtered, then passed through a regulator, which is used to control the exit velocity of the jets. The pipe is then split into two 1" lines to supply each jet. Care is taken to ensure the exit velocity of each jet is the same, as light flow resistance is applied to either line using gate valves.
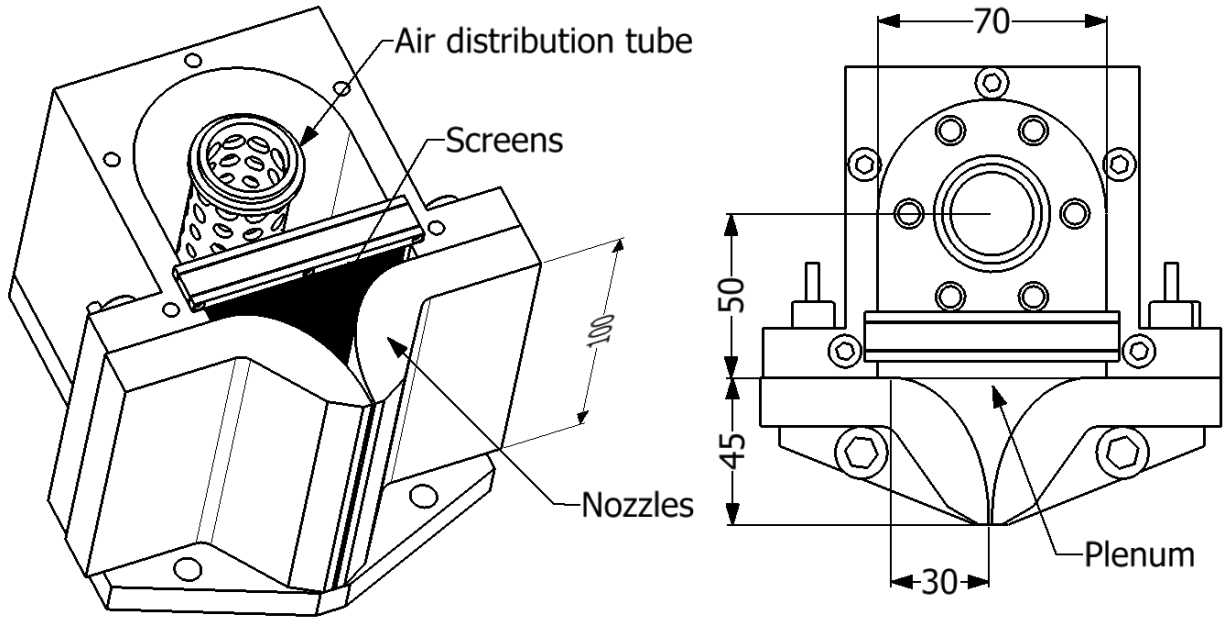
Figure 3.3: Planar jet assembly (all dimensions in mm)

Two identical planar jets, fabricated from aluminum, are used for the current investigation. The various components of the jet assembly are highlighted in Figure 3.3. As the air is injected into the top of each jet assembly, it passes through an air distribution tube, followed by a series of screens before entering the contraction formed by the nozzles. The result is a strongly two-dimensional "top-hat" velocity profile at the exit which has been characterized in detail by Arthurs and Ziada (2012). The screens used to condition the flow prior to the contraction section consists of wire mesh made from 0.0034" stainless steel wire with 70 $wires/inch$, resulting in an open area ratio of 58%. The width of the plenum prior to the contraction is 70 mm and the span of the jet (W) is 100 mm. As shown in Figure 3.3, the nozzles at the exit of the jet are shaped using a 3 : 2 elliptical profile over a 45 mm streamwise distance. The nozzles are adjustable such that the slot width of each jet (h) can be varied from 1 mm ($\frac{W}{h} = 100$) to 4 mm ($\frac{W}{h} = 25$). The slot width is measured and checked
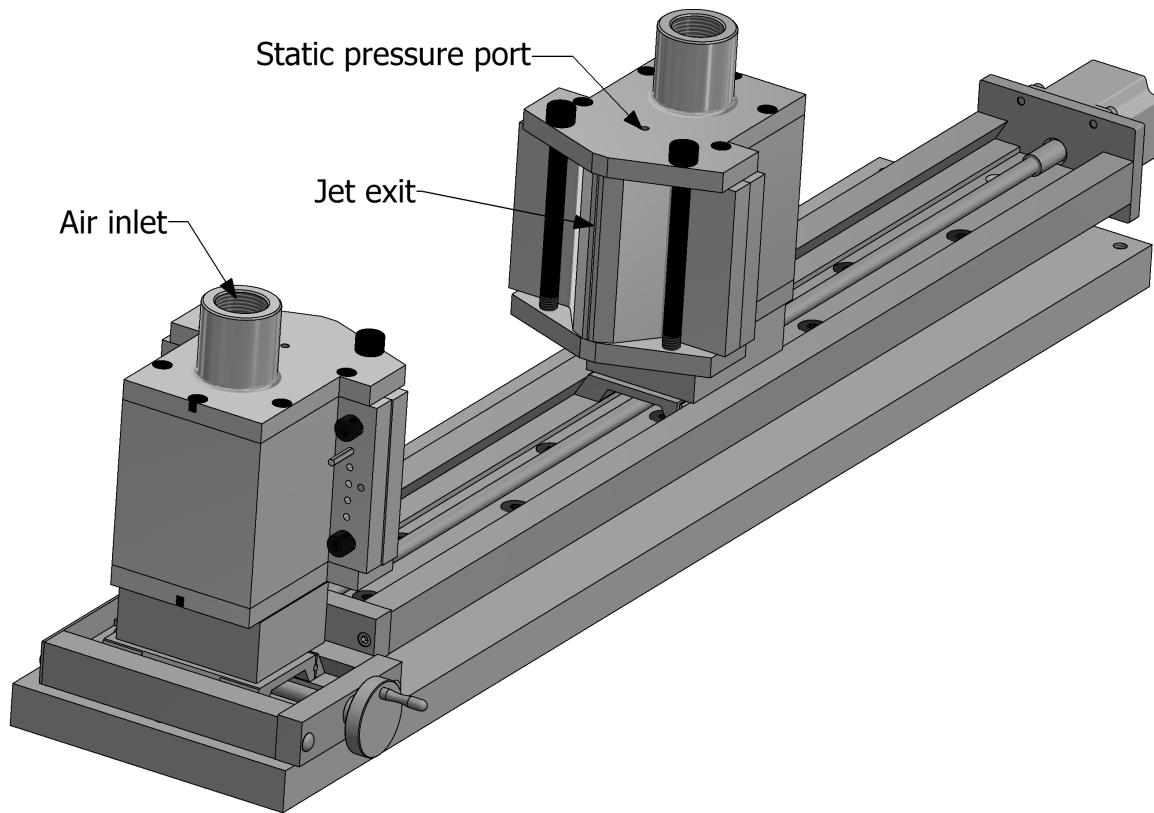
Figure 3.4: Opposing planar jet apparatus

regularly using feeler gauges and a vernier caliper. The velocity at the jet exit is controlled using the regulator upstream of the jets and is determined by measuring the pressure in the plenum through a small orifice in the top plate of the jet, as indicated in Figure 3.3. Further discussion of the methodology used to measure the pressure in the plenum and relate it to the velocity at the jet exit is provided in Section 3.2.1.

3.1.2 Opposing planar jet apparatus

Each jet is mounted on a traverse to allow for the location of each jet to be varied relative to the other, as shown in Figure 3.4. One jet is located on a small manual Velmex A4006

traverse which allows for the translation of the jet in the cross-stream direction, primarily for alignment of the jets along a common centerline. The other jet is situated on a Velmex MA4030 automated traverse capable of 630 $steps/mm$. This traverse allows for translation in the streamwise direction such that the impingement length (L) can be varied from 0 to 580 mm. The traverses are mounted on a 1" thick steel test table, which provides a strong base such that the opposing jets do not vibrate during operation. A schematic of the testing apparatus with the relevant parameters, including the slot width (h), impingement distance (L) and jet exit velocity (V), is shown in Figure 1.1. For the purposes of this investigation, the slot widths of each jet, as well as the exit velocities, are kept the same, such that symmetry of the flow conditions is maintained.

3.1.3   Planar jet impinging on v-shaped plate apparatus

The experimental apparatus used for the jet impinging on a v-shaped plate is the same as that used for the opposing planar jets, however one of the jets is removed and replaced with a v-shaped plate. Therefore, the method of adjusting the slot width, measuring the jet exit velocity, controlling the impingement distance and recording the measurement data is the same as that for the opposing planar jets. The apparatus which is used to investigate the flow phenomenon is shown in Figure 3.5, as the plate is mounted such that the jet impinges directly on the inside corner of the v-shaped plate. The v-shaped plate is made from 12 mm acrylic to allow the laser to pass through the plate and illuminate the flow field. The plate consists of a 90° angle between two 57 mm $\times$ 180 mm plates, as shown in Figure 3.6. As a result, the plates extend 40 mm above and below the span of the jet to ensure the flow field remains strongly two-dimensional. A custom-made aluminum holder is manufactured to support the plate and prevent bending of the plate under the high
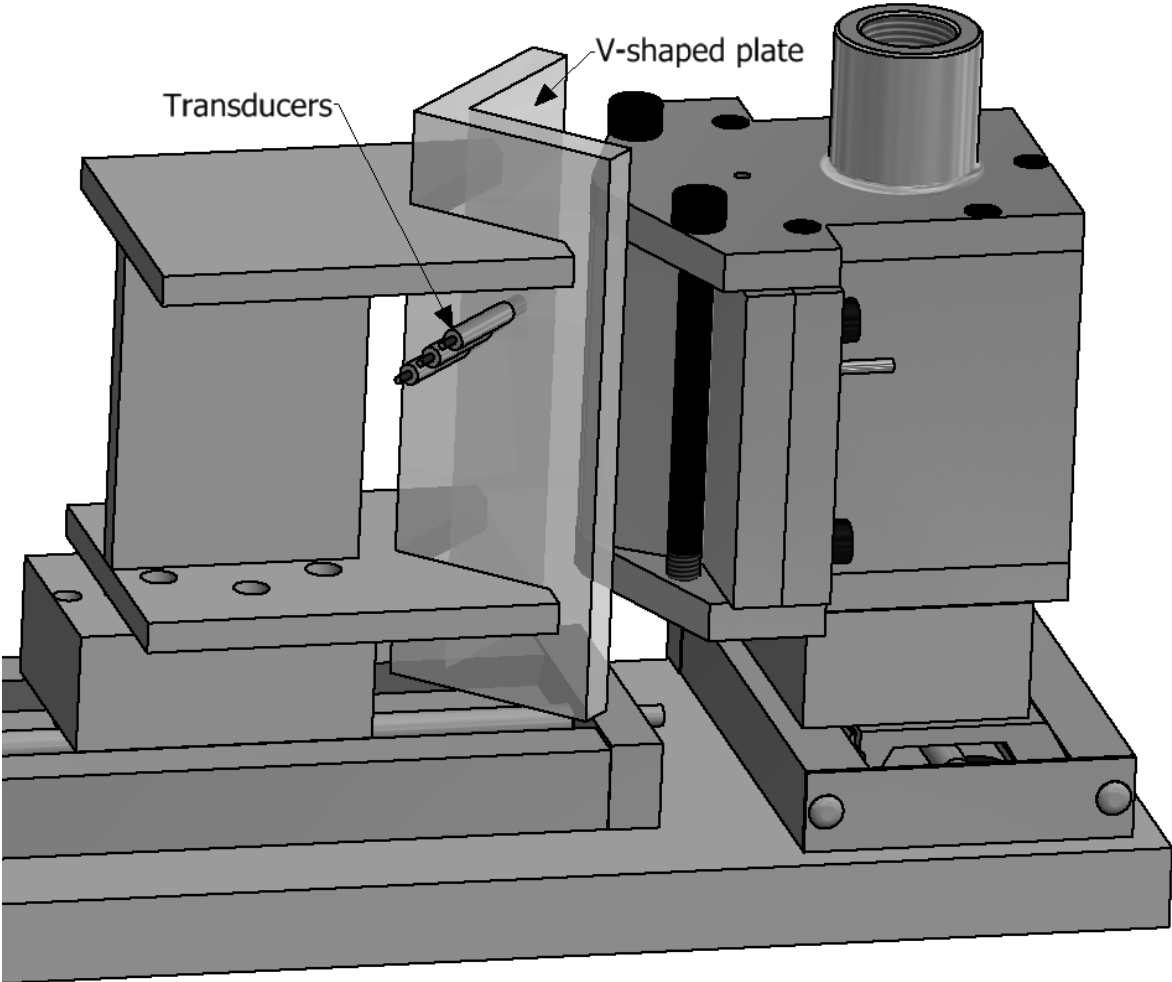
Figure 3.5: Jet impinging on v-shaped plate experimental apparatus
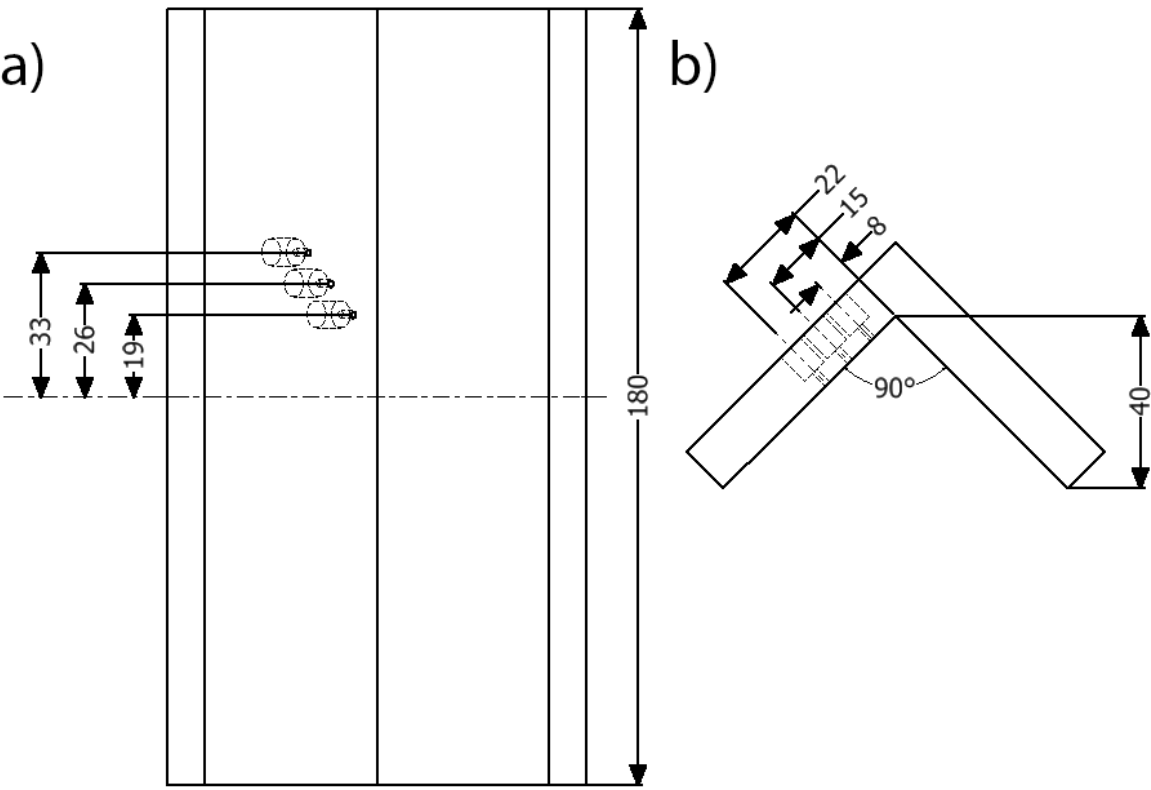
Figure 3.6: a) Front view and b) top view of v-shaped plate (all dimensions in mm)

pressures in the impingement region. The slot width of the jet (h) is 2 mm and the span (W) is 100 mm, resulting in an aspect ratio of 50. While pressure response characteristics for a variety of jet exit velocities (V) and impingement distances (L) will be presented, the flow velocity and impingement distance used to investigate the proposed PIV pressure field mapping technique are 90 m/s and 40 mm, respectively. This case results in a fundamental tone in the oscillations at 170 Hz, which corresponds to a Strouhal number of 0.07. This Strouhal number is slightly less than the 0.11 reported by Lin *et al.* (1993), however this is not surprising as the aspect ratio of the jet will be shown to influence the flow field dynamics.

To determine the phase-resolved pressure field from the proposed PIV technique, phase-locked PIV measurements are performed at 16 phases in the oscillation cycle, each consisting of 200 measurement samples. Each set of measurements are averaged to find the mean and fluctuating components of the flow field. The results of the velocity measurements will be discussed in Section 4.3. Similar to the opposing planar jets, the PIV measurements are taken in the horizontal plane (x-y plane), halfway along the span of the jet. Three transducers are located along one side of the plate, 7.6 mm, 15.0 mm and 22.4 mm from the corner of the v-shaped plate, as shown in Figure 3.6. This results in the fluctuating pressure measurements being recorded along the plate at y locations 0.13L, 0.27L and 0.40L. As indicated in Figure 3.6, care is taken to ensure the transducers are located at slightly different elevations to prevent the flow over one orifice from influencing the pressure reading of another downstream. The transducer locations are selected based on the lateral deflection amplitude of the jets, such that the PIV measurements can be evaluated against the transducer measurements in different regions of the flow field. Transducer 1 is located near the corner of the v-shaped plate, as indicated in Figure 3.6, such that the jet will pass it twice, once as the jet is moving away from the centerline, and once as it returns to the centerline. The second transducer

is located near the location where the jet impinges as it reaches its maximum deflection, therefore the jet will approach the transducer once per oscillation cycle. The third transducer is located further along the plate, such that the jet never reaches this transducer during the entire oscillation cycle, but it does observe the remnants of the flow passing along the plate as it convects away from the impingement region. This will also be shown to be a region where a strong negative pressure is observed which pulls the jet away from the centerline. The transduces are mounted in the manufacturer's recommended recessed orientation such that the fluctuating pressure can be measured through a 1.5 mm orifice. Further details of the transducers and the measurement technique can be found in Section 3.2.2.

3.1.4 Data collection and control systems

Both the jet exit velocities and the impingement lengths are autonomously controlled and monitored while measurements are being performed. The aforementioned traverse which allows the impingement distance to be varied is actuated using a Vexta PK266-03A stepper motor controlled by a Velmex RS232 controller. The exit velocities of the jets are set by actuating the regulator upstream via a DC motor. However, the actuator is only used to set the velocity, as care is taken to ensure the velocity of the jet reaches steady-state and the regulator is not actuated during any measurements. The steadiness of the air supply from the physical plant, in combination with the regulator, results in very little drift in the jet exit velocities during any measurements ($\pm 0.9\%$). Both static and fluctuating pressure data, as well as microphone data, are collected using a four channel National Instruments 9234 data acquisition device with selectable AC/DC coupling for each channel. MATLAB is used to set the impingement distance and velocity by communicating with the controllers via serial ports, as well as recording and processing measurements. The collection and processing of

each measurement type will now be individually discussed.

3.2 Pressure measurements

3.2.1 Static pressure

Static pressure measurements are used to evaluate the pressure in each jet plenum which ultimately allows the exit velocity to be determined. Validyne DP15 pressure transducers are used in conjunction with Validyne CD23 signal conditioners to measure the static pressure. The transducers are calibrated using a Crystal Engineering IS-33 pressure calibrator with a Ralston DPPV air pump. The pressure in the plenum is measured via the aforementioned small orifice on the top plate of each jet assembly prior to the contraction. The pressure in the plenum can be related to the exit velocity through the use of the isentropic flow relation shown in Equation 3.1, which relates pressure to velocity through a nozzle.

$$V = \eta c \sqrt{\frac{2}{\gamma - 1} \left[\left(\frac{P + P_\infty}{P_\infty} \right)^{\frac{\gamma - 1}{\gamma}} - 1 \right]} \tag{3.1}$$

where P is the static pressure, P_∞ is the ambient pressure, γ is the ratio of specific heats, c is the speed of sound and η is the isentropic efficiency of the nozzle. Arthurs and Ziada (2012) conducted a series of experiments for the jets used in the current investigation and found that the nozzle efficiency is consistently in excess of 97% for a complete range of subsonic Mach numbers. However, for the range of velocities studied here ($\leq 180 \ m/s$), the minimum efficiency is 98.5%. Care is taken to ensure the ambient pressure and speed of sound are determined for the conditions of the experiment.

3.2.2   Fluctuating pressure

For the planar jet impinging on a v-shaped plate experiments, which is the topic of discussion in Chapter 4, the fluctuating pressure along the plate is required to validate the results from the PIV-pressure measurements. Three PCB model 112A21 high resolution ICP dynamic pressure transducers are mounted with the recommended recessed installation, such that the pressure at the plate's surface can be measured through a 1.5 mm diameter orifice. The sensitivity of the transducers is 7.3 mV/kPa with a maximum uncertainty of ± 7 Pa. The transducers generate a linear response for frequencies between 0.5 Hz and 25 kHz, up to a maximum pressure amplitude of 690 kPa. The transducers are used in conjunction with a Kistler Type 5134 Coupler to condition and amplify the voltage signal before being digitized using a National Instruments 9234 data acquisition device. A more in-depth discussion of the mounting locations, as well as the purpose of the measurements, is discussed in Section 3.1.3.

3.2.3   Acoustic pressure

Acoustic measurements are taken to evaluate the noise which is radiated from the opposing planar jet oscillator, for which a G.R.A.S. $\frac{1}{4}$" microphone system is used, consisting of a Type 40BP condenser microphone, Type 26AB preamplifier and a Type 12AA power supply. The microphone has a linear response for frequencies between 4 Hz and 70 kHz with only a 3% maximum distortion at 170 dB and is calibrated prior to each experiment with a G.R.A.S. Type 42 pistonphone. The microphone is located above one of the jets along the jet exit plane, 100 mm from the jets' common centerline (i.e. $x = -\frac{L}{2}$ and $y = 100$ mm) and 150 mm above the top of the jet, as shown in Figure 3.7. The microphone measurements are recorded by a National Instruments 9234 data acquisition device at a sampling rate of 51.2 kHz. Each measurement corresponds 60 seconds of data, which is divided into one second samples with
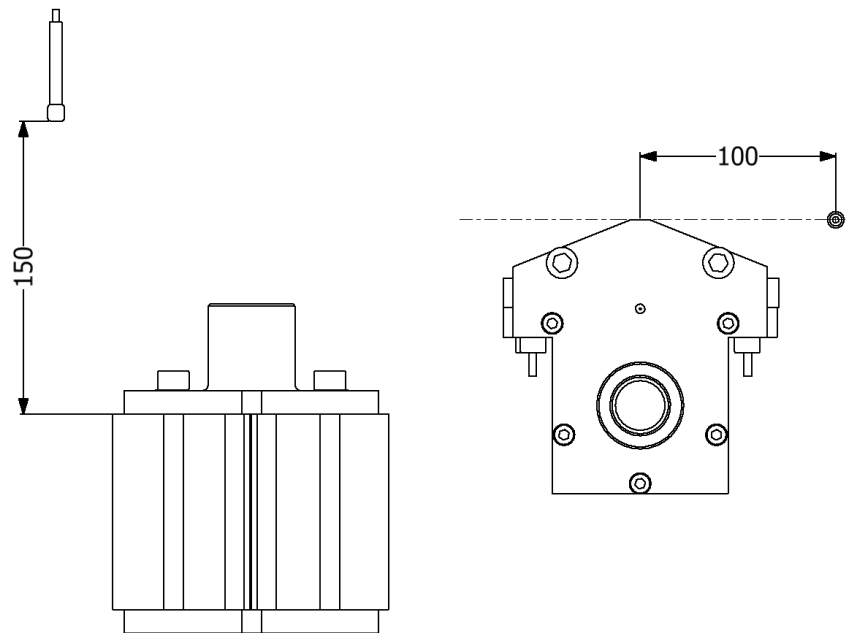
Figure 3.7: Microphone location for acoustic pressure measurements

50% overlap, converted to the frequency domain using Fast Fourier Transforms and then averaged. The data is often presented in non-dimensionless form using the reduced pressure and Strouhal number, defined as

$$P_r = \frac{P_{rms}}{\frac{1}{2}\rho V^2} \tag{3.2}$$

$$St_L = \frac{fL}{V} \tag{3.3}$$

where P_{rms} is the RMS pressure, ρ is the density of the fluid, V is the jet exit velocity, L is the impingement length and f is frequency.
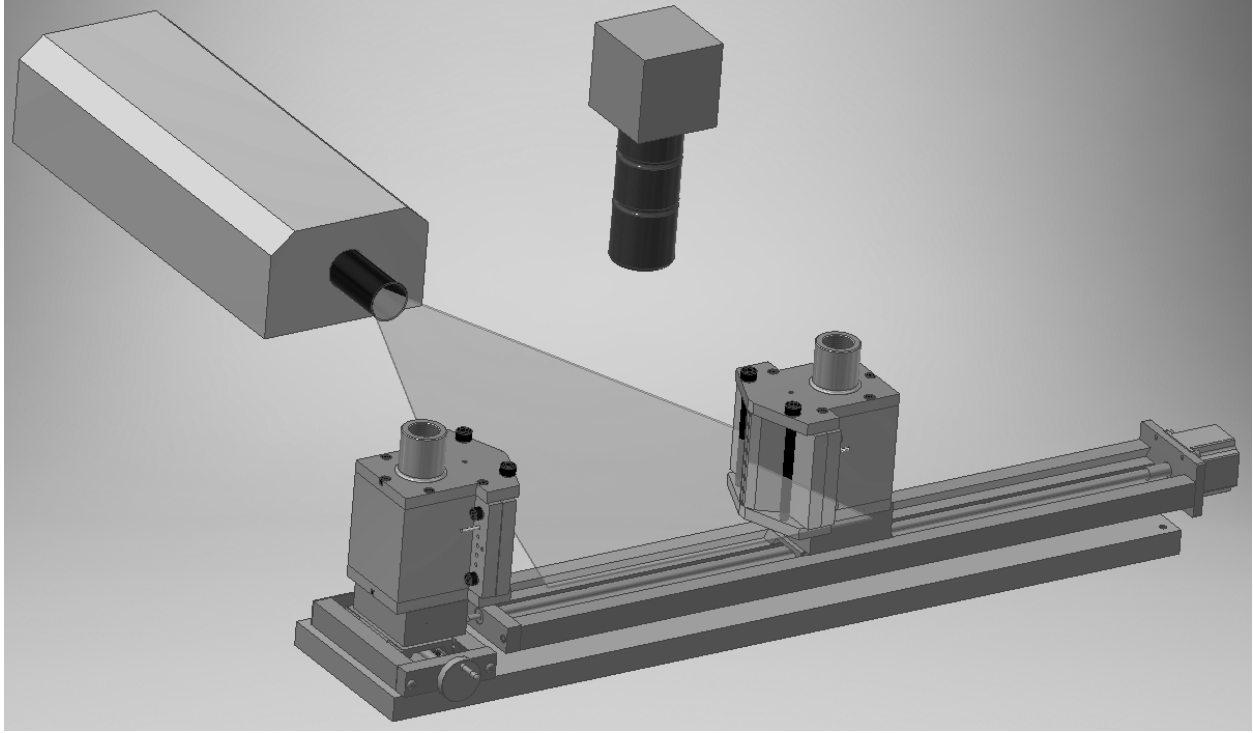
Figure 3.8: Opposing planar jet apparatus with PIV

3.3 Particle Image Velocimetry (PIV)

Flow visualization is conducted throughout the current investigation to detail the flow-field associated with the opposing planar jets. Due to the large aspect ratio of the planar jets, a two-dimensional PIV system is used to measure the flow-field. The PIV measurements are taken in the horizontal plane (x-y plane in Figure 1.1), half way along the span of the jet, as shown in Figure 3.8. The system consists of a 532 nm NewWave Solo 120XT pulsed Nd:YAG laser with a 12-bit Powerview 4MP CCD camera. A Nikon AF Nikkor 50 mm lens with maximum aperture of $f/1.8$ is used, as well as 1.4× to 2.0× magnifiers depending on the required field of view, to optimize the resolution of the images. A 10 nm bandwidth optical bandpass filter centred at 532 nm is situated at the end of the camera

lens assembly to filter light which does not originate from the laser. The laser pulses and camera frames are synchronized using a TSI LaserPulse Model 610035 synchronizer. Insight 4G is used to capture and process the images, while post-processing of the velocity fields is conducted in Tecplot and MATLAB. The flow is seeded using a Laskin aerosol generator with bis(2-ethylhexyl) sebacate as the seeding material. The mean particle diameter of the seeding is 1 μm, which resulted in a Stokes number less than 0.03 and particle tracking error of 1.4% (Melling, 1997). A 'base case' ($h = 2\ mm$, $L = 80\ mm$ and $V = 90\ m/s$) is adopted in the opposing planar jet investigation, as most of the analysis is performed for this case, then extended to determine the impact of each parameter. For this case, a maximum displacement gradient ($\frac{\partial u_i}{\partial x_j}$) of 0.17 $pixels/pixel$ is found, corresponding to an uncertainty of 0.06 $pixels$, resulting in a relative uncertainty of 2.9% (Scarano and Riethmuller, 2000). Further discussion of the uncertainty in the PIV measurements, as well as a list of the uncertainties for each case investigated, is presented in Appendix A. The Classical PIV algorithm is used to process the images with a deformation interpolation scheme, using three primary and two secondary refinements, leading to a final window size of either 16 or 32 $pixels\ square$ depending on the flow parameters, with a 50% overlap. Vector validation rates for all PIV measurements conducted consistently exceeds 99%.

3.3.1   Phase-locked velocity technique

Phase-locked velocity measurements are utilized to capture the time-varying nature of the flow-field which is related to the flow phenomenon. In general, the technique allows for a large sample of images to be taken at repeated points in the flow oscillation cycle. These images can then be averaged to determine the mean and fluctuating components of the velocity field at each phase of the oscillation cycle. Figure 3.9 shows a sample of three periods of
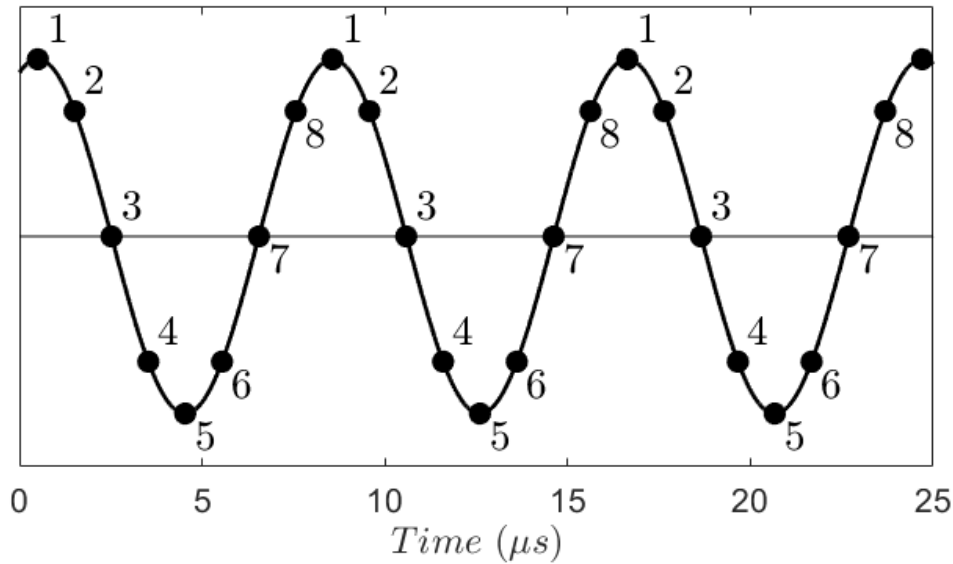
Figure 3.9: Phase-locking methodology

the oscillation cycle with the phase-locked points at each of eight phases in the oscillation cycle highlighted. By averaging each of the eight sets of images over hundreds of cycles, a true representation of the mean flow-field which follows the oscillation cycle can be realized while all other flow structures which do not follow the oscillation cycle will be 'averaged out'. For each flow case which is studied using this phase-locking technique, a series of images are also taken at random points in the oscillation cycle, such that a true representation of the mean flow-field can be realized. The fluctuating velocity field presented later, is calculated by subtracting this mean flow-field from each phase-locked velocity field.

For the case of the opposing planar jets, the microphone signal is used to trigger the PIV measurements. A custom made triggering system generates a falling signal at repeated points in the oscillation cycle. This falling signal is sent to the synchronizer, which then commences the laser firing sequence. After a series of 200 images are recorded at the same relative phase in the oscillation cycle, a small time delay is introduced and the process is

repeated at another point in the oscillation cycle. This process is repeated until a sample of 200 images are recorded at each of sixteen equally spaced points in the oscillation cycle. To increase the precision of the trigger, the raw microphone signal is filtered using an Alligator Technologies USBPBP-S1 Butterworth digital filter with the low and high pass stages set to approximately $\pm 30\%$ of the fundamental frequency, respectively. The result is a triggering signal which repeatedly fires the PIV system at the same phase in the oscillation cycle with an error less than $\pm 80\ \mu s$ for all cases. For the case with the highest frequency of oscillation studied with PIV, this uncertainty corresponds to a phase variation of $\pm 4°$.

Chapter 4

PIV-based pressure field mapping

In the current investigation, it is desired to resolve the detailed time-varying pressure field associated with the opposing planar jets in order to gain valuable insight into the self-sustaining mechanism. In principle, PIV pressure field mapping is straightforward, as the highly-resolved velocity data which is obtainable from PIV can be used to solve the Navier-Stokes equations to find the pressure field. However, in practice, determining the pressure field does not come without several challenges. The most notable of which is the inability of the PIV system to accurately resolve time gradients as a result of the low sampling rate associated with these systems. Current methodologies are either incapable of doing so or are not feasible for the present investigation. Therefore, an original PIV-based pressure field mapping technique will be developed which takes advantage of the strong periodic component of the time-varying flow field. Careful consideration of the methodology used to describe the flow field, as well as the formulation of the pressure Poisson equation and boundary conditions, is necessary. The result is a pressure field mapping technique which can very accurately resolve time-varying flow field characteristics with readily available PIV systems. For the current investigation, high speed jet oscillations will be resolved using a PIV system

with only a 7.5 Hz sampling rate.

However, as discussed previously, the novel nature of the developed technique merits its benchmarking against well-established pressure measurement techniques. Due to the absence of any physical boundary in the flow field of the opposing planar jet oscillator, traditional measurement techniques will prove to be intrusive and subsequently, will not provide reliable pressure measurements to effectively evaluate the calculated pressure field. Thus, the planar jet impinging on a v-shaped plate, which demonstrates similar flow oscillation characteristics to that of the opposing jets, will be used to benchmark the proposed technique as a result of the physical boundary which exists in the flow field. *While the phase-resolved velocity and pressure fields of the planar jet impinging on a v-shaped plate will be presented, their contribution to the self-sustaining mechanism of this flow case is not to focus of the current investigation. This flow case is used only to benchmark the proposed pressure field mapping technique, which will then be utilized in subsequent chapters to investigate details of the underlying mechanism associated with the opposing planar jet oscillator.* Existing methodologies surrounding PIV pressure field mapping are discussed in Section 2.4, while the planar jet impinging on a v-shaped plate apparatus is introduced in Section 3.1.3. After first reviewing the response characteristics of the apparatus, this chapter will outline the proposed pressure field mapping methodology and measurement procedure. Phase-resolved flow field measurements will then be presented, followed by an in-depth analysis of the pressure field calculations. Finally, the time-varying pressure field will be presented and evaluated against a series of transducer measurements taken along the physical boundary. In subsequent sections, this technique will be extended to determine the pressure field which helps sustain the opposing planar jet oscillations.

4.1   Planar jet impinging on a v-shaped plate

An original PIV-based pressure field mapping technique will now be presented and discussed. It is essential to evaluate the effectiveness of this new technique by comparing it to traditional pressure measurement techniques. However, as discussed previously, traditional methods of measuring pressure are either intrusive in nature or can only measure pressure along a physical boundary. As such, traditional measurement techniques are not effective at measuring the time-varying pressure field for the opposing planar jets as a result of the nonexistence of physical boundaries, as well as the presence of strong multi-directional flow characteristics making pressure probes ineffective. Therefore, while the focus of the current investigation surrounds the opposing planar jet oscillator, a similar flow oscillator will be utilized to evaluate the effectiveness of the proposed PIV pressure field mapping technique. The technique will then be extended in later chapters to investigate the pressure field associated with the opposing planar jet oscillator.

The flow oscillator which will be used consists of a planar jet impinging on the inside corner of a v-shaped plate, as shown in Figure 4.1. Similar to the opposing planar jets, the flow case is defined by a jet exit velocity (V), a slot width (h) and an impingement distance (L). The plate is situated downstream such that the jet impinges directly on the corner of the plate. As a result, the flow is forced to circulate back towards either side of the jet exit, which will be shown to form strong circulation zones in these regions. While very little is known about the jet impinging on a v-shaped plate, flow oscillations have been reported with large low frequency lateral deflection oscillations of the jet column, which is similar to the opposing planar jets. The similarity between these flow characteristics and those observed in the opposing planar jets, as well as the existence of well defined boundaries in the flow field where traditional methods of pressure measurements can be utilized, are the
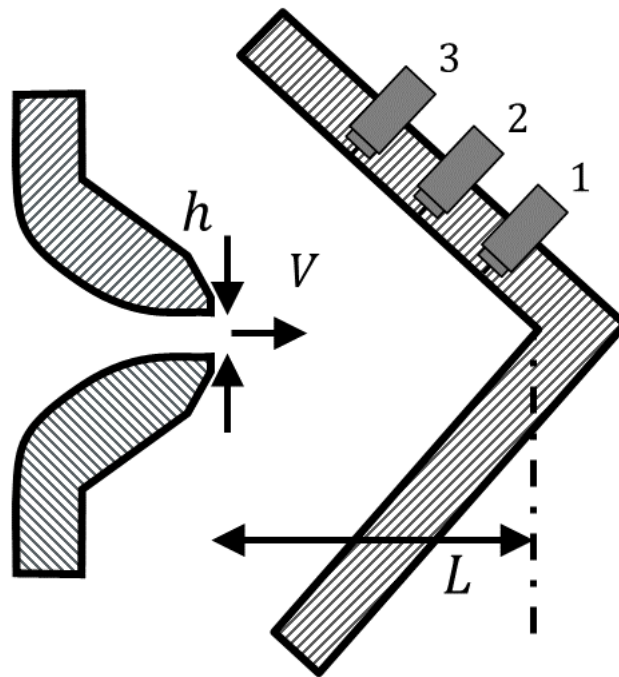
Figure 4.1: Schematic of jet impinging on a v-shaped plate

primary reasons for using this flow oscillator to evaluate the effectiveness of the proposed pressure field mapping technique. As shown in Figure 4.1, three transducers are situated along the v-shaped plate to effectively measure the fluctuating pressure at these locations. These pressure measurements will later be used to evaluate the effectiveness of the proposed PIV pressure field mapping technique. Further details of the known characteristics of the flow oscillations which arise from a planar jet impinging on a v-shaped plate will now be discussed, followed by a review of the experimental apparatus used to investigate the flow phenomenon.
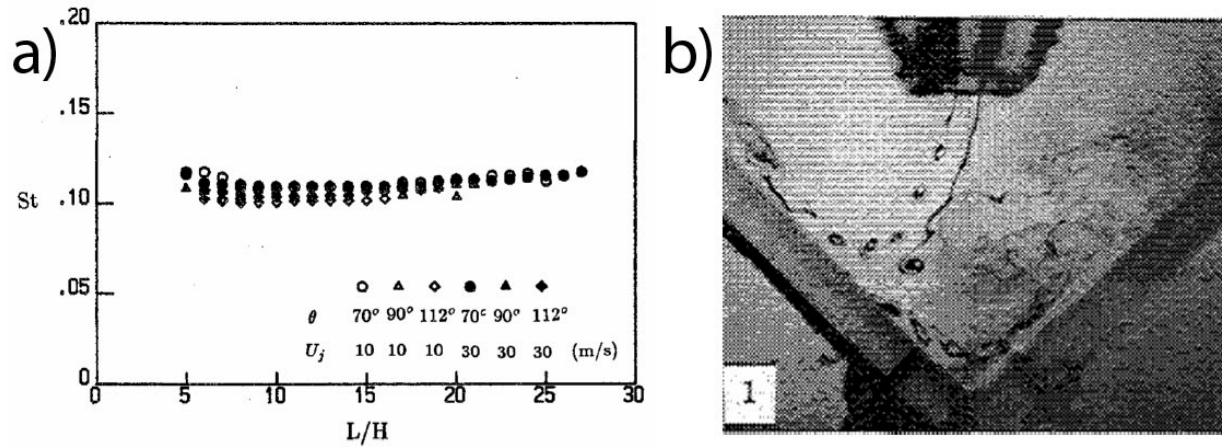
Figure 4.2: a) Strouhal number and b) flow visualization of deflection oscillations of jet impinging on a v-shaped plate (Lin *et al.*, 1993)

4.1.1   Oscillation characteristics

To date, there is only one study in the literature on the nature of the oscillations produced by a planar jet impinging on a v-shaped plate. (Lin *et al.*, 1993) experimentally studied the response characteristics of the oscillations using a gas jet at low Mach numbers ($M <$ 0.1) over various impingement ratios ($\frac{L}{h} < 30$), with a slot width (h) of 12.5 mm. The investigation also includes qualitative flow visualization of the flow phenomenon using a water jet with a 4 mm slot width and an exit velocity less than 1 m/s. The Strouhal number (St_L) of the oscillations is reported to be approximately 0.11 consistently for a wide range of plate angles, jet exit velocities and impingement ratios, as shown in Figure 4.2 a). This range of Strouhal numbers shows some similarity with those observed from the opposing planar jets, while all other jet oscillators in the literature produce oscillations at a Strouhal number over an order of magnitude higher. For the wide range of offset distances and jet exit velocities investigated by Lin *et al.* (1993), the oscillations demonstrate the largest pressure amplitudes for a plate angle of 90°, measured from one plate surface to the

other. As such, the 90° v-shaped plate case is adopted for the current investigation. Subset b) of Figure 4.2 demonstrates the deflection oscillations of the jet column which is observed by the investigators. This flow visualization shows large lateral deflection oscillations of the jet column, once in each direction per oscillation cycle. This figure also shows the existence of coherent structures in the shear layers of the jet; however, they are shown to exist at much higher frequencies and are not synchronized with the jet deflection oscillations.

The ability of this flow case to sustain strong high-quality oscillations makes it ideal to validate the proposed PIV pressure field mapping technique. In both the case of the planar jet impinging on v-shaped plate and the opposing planar jets, the low Strouhal number associated with these oscillations suggests that a particle leaving the jet exit will travel many impingement distances downstream during an oscillation cycle and will only remain in the immediate flow vicinity for a short portion of the oscillation cycle. Yet the ability of the jet(s) to repeatedly produce high-quality oscillations suggests that the pressure field is likely playing an essential role in sustaining the oscillations as it drives the jet column back and forth. Therefore, in both cases, it is expected that the pressure field measurements will yield strong pressure fluctuations which are synchronized with the jet oscillations.

4.1.2   Response characteristics of fluctuating pressure along plate

The response characteristics of the planar jet impinging on a v-shaped plate will now be discussed for the flow case with a slot width (h) of 2 mm, impingement distance (L) of 40 mm and a jet exit velocity (V) of 90 m/s. The oscillation frequency which is observed by the transducers as the impingement ratio and jet exit velocity are varied is presented in Figure 4.3 a). The frequency of oscillation is negatively correlated to the impingement distance and positively correlated to the jet exit velocity. The data is shown to collapse very
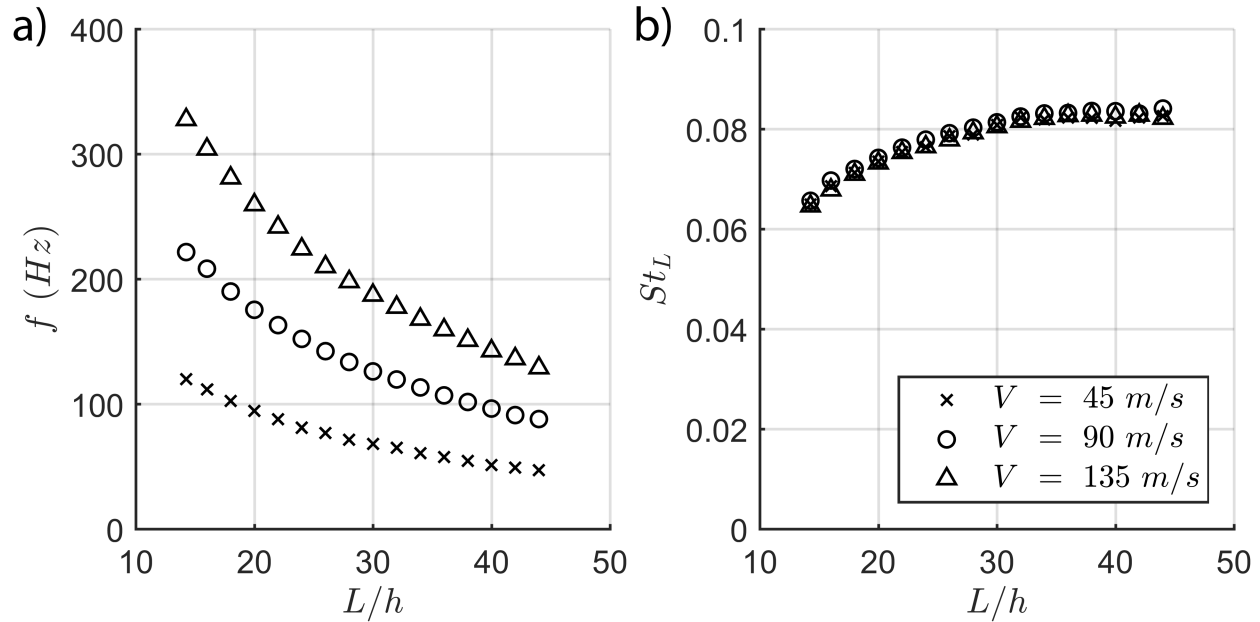
Figure 4.3: a) Frequency and b) Strouhal number of oscillations for varying impingement ratios and jet velocities

well for various jet exit velocities when the Strouhal number is used to non-dimensionalize the frequency of oscillation, as shown in Figure 4.3 b). However, there does appear to be a slight decrease in the Strouhal number as the impingement distance gets smaller, which is believed to be a result of the gap between the end of the v-shaped plate and the jet nozzle getting smaller. As the gap gets smaller, the ability of the flow to effectively convect away from the immediate vicinity of the jets is inhibited, which ultimately will delay the dissipation of the circulation zones, effectively increasing the time required for the jets to return to the centerline. However, the influence of this gap on the oscillation characteristics is outside the scope of the current investigation, as the jet impinging on a v-shaped plate experiment is utilized only as a means of evaluating the effectiveness of the proposed PIV pressure field mapping technique. Albeit, a similar discussion will be presented in Chapter 6, as the development and dissipation of the circulation zones created by the opposing planar jets will

be impeded using splitter plates, causing a similar decrease in the frequency of oscillation. Nonetheless, the oscillations observed in the current investigation are very similar to those observed by Lin *et al.* (1993) in both the reported Strouhal numbers and flow field dynamics.

The average frequency spectrum for each transducer is determined by performing spectral analyses on 60 seconds of data in one second samples with 50% overlap. The time signals of the transducers are recorded simultaneously and a phase shift is introduced to the samples, such that the spectral phase associated with the fundamental frequency for the first transducer is 0°. This allows for averaging of both the amplitude and phase components of the spectra, providing for a more comprehensive comparison with the fluctuating pressure determined from the proposed PIV pressure field mapping technique. The resulting average spectra are presented in Figure 4.4 with the amplitudes in subset a) and the phases in subset b). The fluctuating pressure signals are shown to be dominated by the fundamental frequency and first harmonic. This is expected since, as discussed previously, the transducers are strategically located such that the jet passes each transducer twice, once or not at all, respectively. The fundamental component is strongest in the second transducer, as this transducer is situated in a location where the jet impinges on it usually once, at the phase in the oscillation cycle when the jet reaches its maximum deflection. The first harmonic is strongest for the first transducer as a result of being located near the corner of the v-shaped plate and the jet passing it twice. The third transducer has smaller components of both the fundamental and first harmonic since the jet never directly impinges on it. While the signals contain very little noise, the second transducer does demonstrate some intermittent behaviour over time. A sample of the raw time signals is shown in Figure 4.5, which demonstrates the intermittency of the second transducer. Observing the positive peaks in this time signal, some have two well defined small peaks at the maximum (i.e. $t = 3\ ms$), while
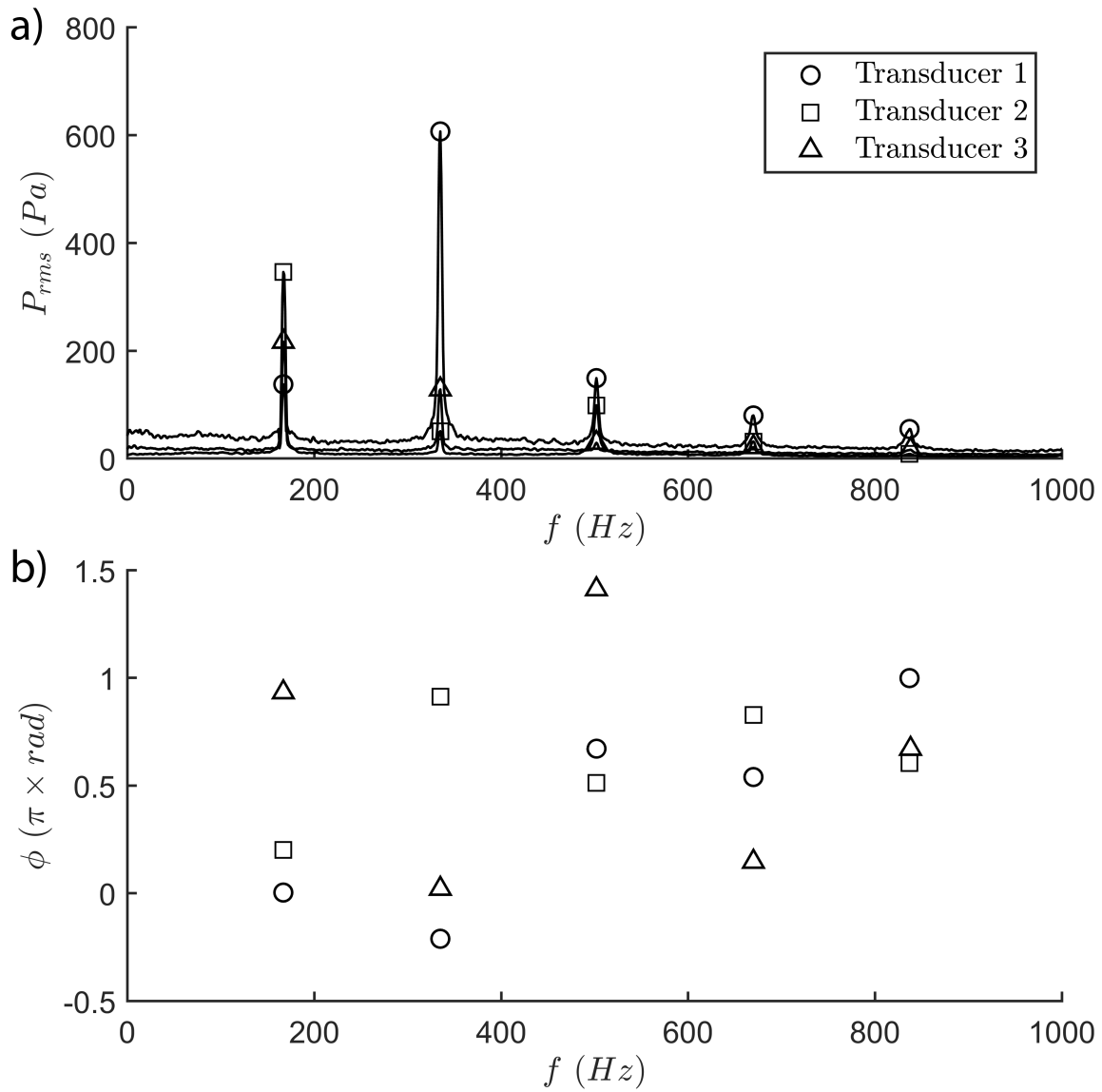
Figure 4.4: Frequency spectra of transducers signals including both a) RMS amplitude and b) phase
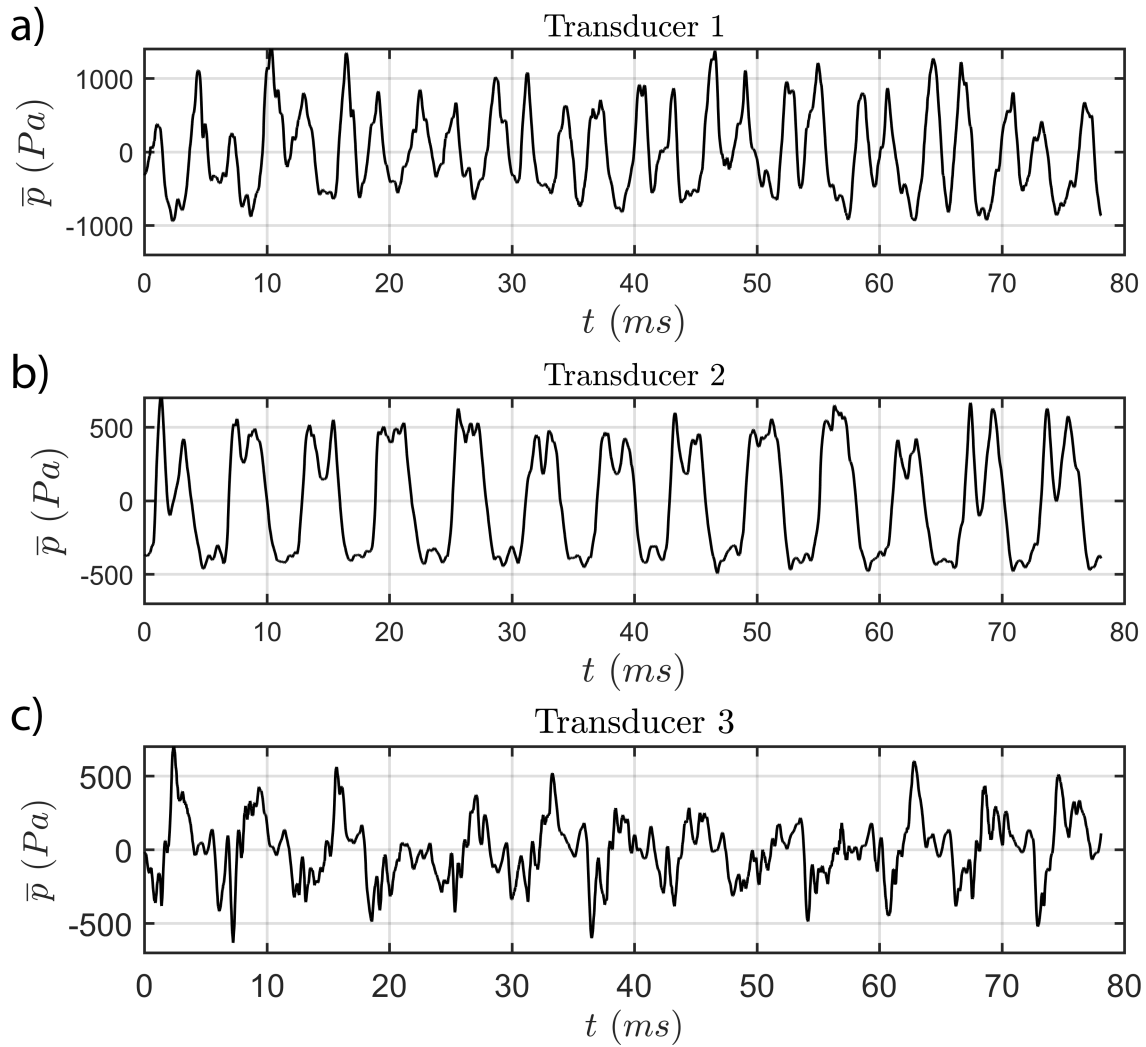
Figure 4.5: Sample raw time signals from fluctuating pressure at transducers a) 1 b) 2 and c) 3

others have only one large flat peak (i.e. $t = 20\ ms$). This is believed to be a result of the transducer being located precisely where the jet impinges at its maximum deflection. As a result of slight variation in the deflection angle from one cycle to the next, in some cycles the jet deflects just far enough to impinge on the transducer once, while in other cycles the jet deflects further and impinges on the transducer twice, resulting in two distinct peaks. Therefore, even though the second transducer demonstrates a strong fundamental frequency component, the third transducer is chosen as the signal to phase-lock the PIV measurements.

4.2   Proposed technique

The primary benefit of the proposed technique is the ability to detail and analyse high frequency features of the pressure field without the need for expensive and involved PIV systems which may have limited capability in other aspects. Until now, the ability to accurately detail the time-varying pressure field requires a high sampling rate PIV system or the ability to record four sequential images with a small time delay between them. However, with the proposed technique, the only requirement is the ability to trigger the PIV system at repeated phases in the oscillation cycle. While this does come with its own challenges, as will be discussed later, if the flow contains a strong periodic component, the detailed time-varying pressure field can be resolved using readily available PIV systems. For example, the PIV system used for the current investigation has a maximum sampling rate of 7.5 Hz, yet the system can map the time-varying pressure field for oscillation frequencies in the $10s$ of kHz range.

Similar to many turbulent flow analysis techniques, the proposed methodology takes advantage of the ability to characterize the velocity and pressure fields into mean and fluctuating components. However, in this case, both the velocity and pressure fields will be
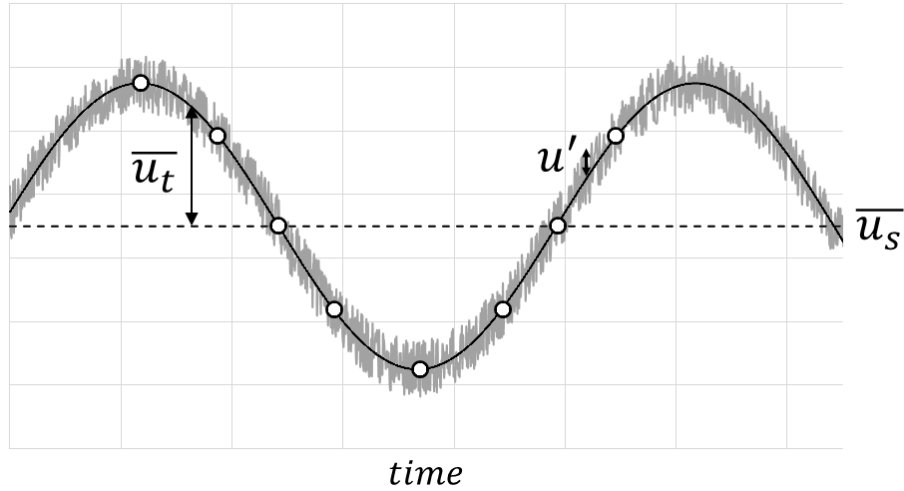
Figure 4.6: Sample time signal of velocity at a point in the flow field showing velocity components

assumed to have a periodic mean component which follows the mean motion of the flow oscillations and a fluctuating component away from this mean component. Figure 4.6 shows an example of a velocity time signal which represents the velocity at a point in space. The true velocity signal is shown by the noisy signal in grey, while the periodic mean velocity is indicated by the solid black line. The periodic mean component can further be decomposed into a steady ($\overline{u_s}$) and a transient component ($\overline{u_t}$), while the fluctuations are measured as the difference between the actual signal and the mean component.

$$u = \overline{u} + u' = \overline{u_s} + \overline{u_t} + u' \tag{4.1}$$

$$v = \overline{v} + v' = \overline{v_s} + \overline{v_t} + v' \tag{4.2}$$

$$p = \overline{p} + p' = \overline{p_s} + \overline{p_t} + p' \tag{4.3}$$

For each phase in the oscillation cycle which the PIV system is phase-locked to, a sample of velocity field measurements is recorded over hundreds of cycles. For each set of images

associated with a phase in the oscillation cycle, statistical analysis can be performed to determine the mean velocity field ($\overline{u}$) and the standard deviation of the fluctuations ($\overline{u'}$). The result is a mean and fluctuating component attributed to each phase-locked set of images which are both time dependent and more specifically, periodic. Furthermore, it is important to note that while the mean component in Figure 4.6 is illustrated to be represented by a single sine wave at the fundamental frequency, in reality the signal will be made up of the fundamental and its associated harmonics which follow the flow oscillations. Any other flow oscillations which do not follow an integer multiple of the frequency in which the PIV system is phase-locked to will be 'averaged out'. The fluctuating component away from the mean component will therefore be made up of the random turbulence in the flow, as well as other fluctuations which are not related to the oscillations being phase-locked to.

The necessary condition for the proposed pressure mapping technique to effectively measure the phase-resolved pressure field is the ability to repeatedly trigger the PIV system at relatively the same phase in the oscillation cycle, such that an accurate measurement of the time gradients, as well as the phase-resolved spatial gradients, of the velocity field can be obtained. As will be discussed in more depth in Section 4.3, for the current investigation, the PIV system is triggered using a filtered signal from the third transducer, which triggers the system with an accuracy of $\pm 4°$. The results will be shown to agree very well with the pressure measurements from the transducers. While the proposed technique works very well for the current investigation, the technique is ideal for cases where an external periodic excitation is introduced to the flow, such as the periodic load introduced for a fluid-structure interaction problem, or acoustic excitation where an acoustic wave is used to excite the flow field. In these cases, a strong, low noise, synthetic signal can be used to trigger the PIV system very accurately.

Once the phase-resolved velocity gradients are obtained for both the periodic mean and fluctuating components, they can be used to solve the pressure Poisson equation for each phase in the cycle. The pressure Poisson equation, introduced in Section 2.4.1, must first be reformulated to allow the phase-resolved velocity field measurements to be used. By introducing Equations 4.1, 4.2 and 4.3 to Equation 2.5, one can determine that the pressure Poisson equation can be reformulated as,

$$-\nabla^2 \overline{p} = \rho \left[\left(\frac{\partial \overline{u}}{\partial x} \right)^2 + 2 \frac{\partial \overline{u}}{\partial y} \frac{\partial \overline{v}}{\partial x} + \left(\frac{\partial \overline{v}}{\partial y} \right)^2 + \left(\frac{\partial u'}{\partial x} \right)^2 + 2 \frac{\partial u'}{\partial y} \frac{\partial v'}{\partial x} + \left(\frac{\partial v'}{\partial y} \right)^2 \right] \qquad (4.4)$$

Subsequently, Equation 4.4 can be averaged over each set of measurements taken at each phase in the oscillation cycle, and rearranged to find,

$$-\nabla^2 \overline{p} = \rho \left[\left(\frac{\partial \overline{u}}{\partial x} \right)^2 + 2 \frac{\partial \overline{u}}{\partial y} \frac{\partial \overline{v}}{\partial x} + \left(\frac{\partial \overline{v}}{\partial y} \right)^2 \right] + \rho \left[\frac{\partial^2 (\overline{u'^2})}{\partial x^2} + 2 \frac{\partial^2 (\overline{u'v'})}{\partial x \partial y} + \frac{\partial^2 (\overline{v'^2})}{\partial y^2} \right] \qquad (4.5)$$

At each spatial location in the flow field, the mean velocity components in the x and y directions ($\overline{u}$ and $\overline{v}$) are determined by averaging the velocity measurements over each set of phase-resolved PIV measurements. Similarly, the $\overline{u'^2}$ and $\overline{v'^2}$ are determined by finding the variance of the x and y velocity components, respectively, while $\overline{u'v'}$ is determined by calculating the covariance of the velocity components over each set of measurements. Each of these terms in Equation 4.5 are therefore obtainable from the PIV measurements, and the pressure Poisson equation can be solved with no simplifications. By solving the pressure Poisson equation, a true depiction of the time-varying pressure field which is associated with the oscillation cycle can be obtained.

In this form, no simplifications have been made to the pressure Poisson equation, except neglecting compressibility effects. As discussed in Section 2.4.1, while the transient and

viscous terms do not appear in Equation 4.5, the equation is valid for unsteady and viscid flows, as these terms are canceled out in its formulation. However, the result is a second-order differential equation which requires boundary conditions. Therefore, the transient and viscous influence on the pressure calculations is often incorporated through the boundary conditions, usually by using the Navier-Stokes equations to define Neumann boundary conditions normal to the boundaries where the flow is not constrained by a physical domain. These boundary conditions can be found similar to the above analysis, by introducing Equations 4.1, 4.2 and 4.3 to the Navier-Stokes equations and averaging over each set of phase-locked measurements,

$$-\nabla \overline{p} = \rho \frac{\partial \overline{u}}{\partial t} + \rho \left(\overline{u} \frac{\partial \overline{u}}{\partial x} + \overline{v} \frac{\partial \overline{u}}{\partial y} \right) - \mu \nabla^2 \overline{u} + \rho \left(\frac{\partial \overline{u'^2}}{\partial x} + \frac{\partial \overline{u'v'}}{\partial y} \right) \tag{4.6}$$

A detailed derivation of Equation 4.5 is available in Appendix B, and a further discussion of the source terms and boundary conditions used for the current investigation will be provided in Sections 4.4.1 and 4.4.2, respectively.

While the spatial gradients in both the pressure Poisson equation, as well as the boundary conditions, are obtainable directly from the PIV measurements, determination of the time dependence has proven difficult for past PIV-based pressure solvers. As discussed previously, to determine the time dependent terms, either expensive and often unobtainable PIV systems are required, or the flow is assumed to be steady. The former is not available for the current study, while the latter is not adequate, as a detailed depiction of the time-varying pressure field is required. One of the major benefits of the proposed pressure mapping technique is the ability to determine the time dependence of the flow field without the need for expensive equipment which is not readily available. By observing the phase-resolved flow field over

the oscillation cycle, the time dependence can be obtained. In fact, as a result of phase-resolving the measurements, the time dependence of the flow field can be completely defined by the mean steady component ($\overline{u_s}$) and the fluctuating components at discrete frequencies associated with the phase-locking time scale and its harmonics. For example, the time-varying velocity at each point in space can be described by,

$$\overline{u} = \overline{u_s} + \sum A_i \sin(2\pi i f_n t - \phi_i) \tag{4.7}$$

Where f_n is the fundamental frequency the PIV system is phase-locked to and A_i and ϕ_i are the amplitude and phase components associated with the ith frequency component. To determine the time dependence, a function of this from is used to model to the PIV data, and a unique set of values A_i and ϕ_i is determined for each point in space. All other random fluctuations and modes of oscillation which follow other time scales are not synchronized with the fundamental oscillations (i.e. column deflection oscillation) and will subsequently be eliminated through averaging the hundreds of measurements recorded at the same phase in the oscillation cycle. Even though the higher harmonic components are also different time scales than the phase-locked measurements, if the frequency components are harmonics of the fundamental oscillations, then they will still follow these oscillations, but will repeat more than once per oscillation cycle. For example, one will observe the second harmonic oscillations twice per oscillation cycle, the third harmonic three times, and so on. Nonetheless, as a result of being synchronized with the fundamental oscillations, they will be preserved in the phase-resolved measurements. To this end, the current oscillations are strongly dominated by the fundamental and first harmonic, which may not be the case for many other oscillating flow phenomena. To accurately capture features in the flow field which are associated with much larger harmonics, it is necessary to record measurements

67

using more resolved phases in the oscillation cycle. Further discussion of the calculation of the time dependence of the flow field for the current investigation is provided in Section 4.4.2.

4.3   Phase-resolved flow field

The phase-locked PIV measurements are obtained using the aforementioned process discussed in Section 3.3.1. The pressure signal from the third transducer along the v-shaped plate is used to trigger the PIV system at 16 phases in the oscillation cycle, as a result of its large, consistent, fundamental frequency component. As discussed in Section 4.1.2, while the second transducer demonstrates a higher amplitude fundamental component, the shape of the waveform varies from one cycle to the next as a result of being located near the region where the jet impinges as it reaches its maximum deflection. Even though, the pressure signal from the third transducer has a lower signal-to-noise ratio, the bandpass filter removes the high frequency noise from the signal, generating a more consistent and repeatable waveform over many oscillation cycles. The bandpass filter used is discussed in Section 3.3.1, and consists of high and low pass stages at 166.0 Hz and 174.1 Hz, respectively. Figure 4.7 shows the phase-resolved mean flow field at eight phases in the oscillation cycle, with the contours indicating the velocity magnitude and accompanying streamlines indicating the directionality of the flow. The same flow case as discussed in the response characteristics section is used ($h = 2\ mm$, $L = 40\ mm$ and $V = 90\ m/s$). The jet column clearly shows a full deflection both upwards and downwards through a single oscillation cycle. At 0°, the jet is impinging directly on the corner of the v-shaped plate as the jet column moves downward. The large circulation zone below the jet column appears closer to the jet exit, as compared to the circulation zone above the jet. As the cycle steps forward, the jet deflects downward until it reaches its maximum deflection at approximately 90°. At this phase in the oscillation
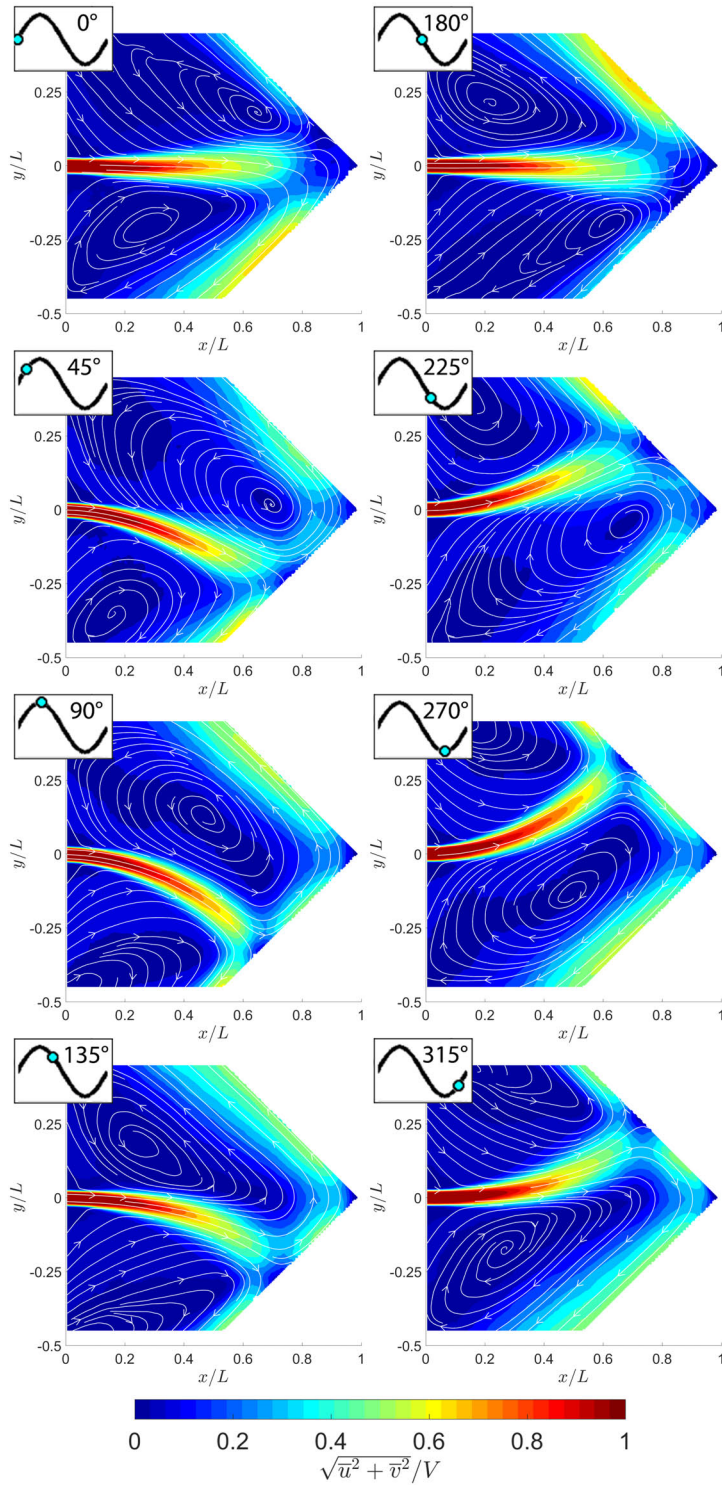
Figure 4.7: Phase-resolved velocity field with accompanying streamlines of jet impinging on v-shaped plate at eight phases in the oscillation cycle

cycle, the jet is impinging on the v-shaped plate at an approximate cross-stream location of $y = -0.3L$. Simultaneously, the circulation zone below the jet begins to move away from the jet column, while the upper circulation zone moves closer to the jet exit. As the jet continues back towards the centerline, the velocity along the top half of the v-shaped plate continues to increase as more momentum is transferred upward. The jet continues to move back towards, and ultimately past, the centerline as the cycle repeats. *While it is not the focus of the present investigation to reveal the self-sustaining mechanism associated with the jet impinging on a v-shaped plate*, there are a number of similar characteristics between this phase-resolved flow field and that of the opposing planar jets, which will be discussed in detail in later chapters. In particular, the following analysis will show pressurizing of the stagnation region near the corner of the v-shaped plate which pushes the jet away from the centerline, as well as strong low-pressure regions in the circulation zones which create pressure gradients across the jet column that are responsible for driving the jet columns back towards, and ultimately across, the centerline.

4.4   Time-varying pressure field

The determination of the phase-resolved pressure field of the planar jet impinging on a v-shaped plate will now be discussed, with specific focus on the composition of the source term in the pressure Poisson equation and the various boundary conditions used. The phase-resolved pressure field will then be presented, followed by a comparison to the transducer measurements along the plate.

4.4.1   Source term determination

The source term, created by the pressure Poisson equation (Equation 4.5), which is used to determine the phase-resolved pressure field can be separated into two sets of terms, one associated with the convective flow field (f_c) and the other with the fluctuating flow field (f_f).

$$-\left(\frac{\partial^2 \overline{p}}{\partial x^2} + \frac{\partial^2 \overline{p}}{\partial y^2}\right) = f_c + f_f \tag{4.8}$$

where,

$$f_c = \rho \left[\left(\frac{\partial \overline{u}}{\partial x}\right)^2 + 2\frac{\partial \overline{u}}{\partial y}\frac{\partial \overline{v}}{\partial x} + \left(\frac{\partial \overline{v}}{\partial y}\right)^2\right] \tag{4.9}$$

$$f_f = \rho \left[\frac{\partial^2 (\overline{u'^2})}{\partial x^2} + 2\frac{\partial^2 (\overline{u'v'})}{\partial x \partial y} + \frac{\partial^2 (\overline{v'^2})}{\partial y^2}\right] \tag{4.10}$$

Each of these components of the source equation are plotted for four phases in a half cycle in Figure 4.8, with the convective component on the left and the fluctuating component on the right. Noting the difference in the scale of each set of plots, the source term for the fluctuating component is much smaller than that associated with the convection. Specifically, the typical magnitude of the fluctuating component is only about 10% of the convective component, with the largest influence of the fluctuating component occurring near the phases where the jet impinges directly on the corner of the v-shaped plate ($\theta = 0°$ & $180°$). This clearly demonstrates the fundamental nature of the mechanism, which is not surprising as these oscillations persist over a wide range of flow parameters and have even been reported with similar characteristics for low Reynolds number jets (Lin *et al.*, 1993).
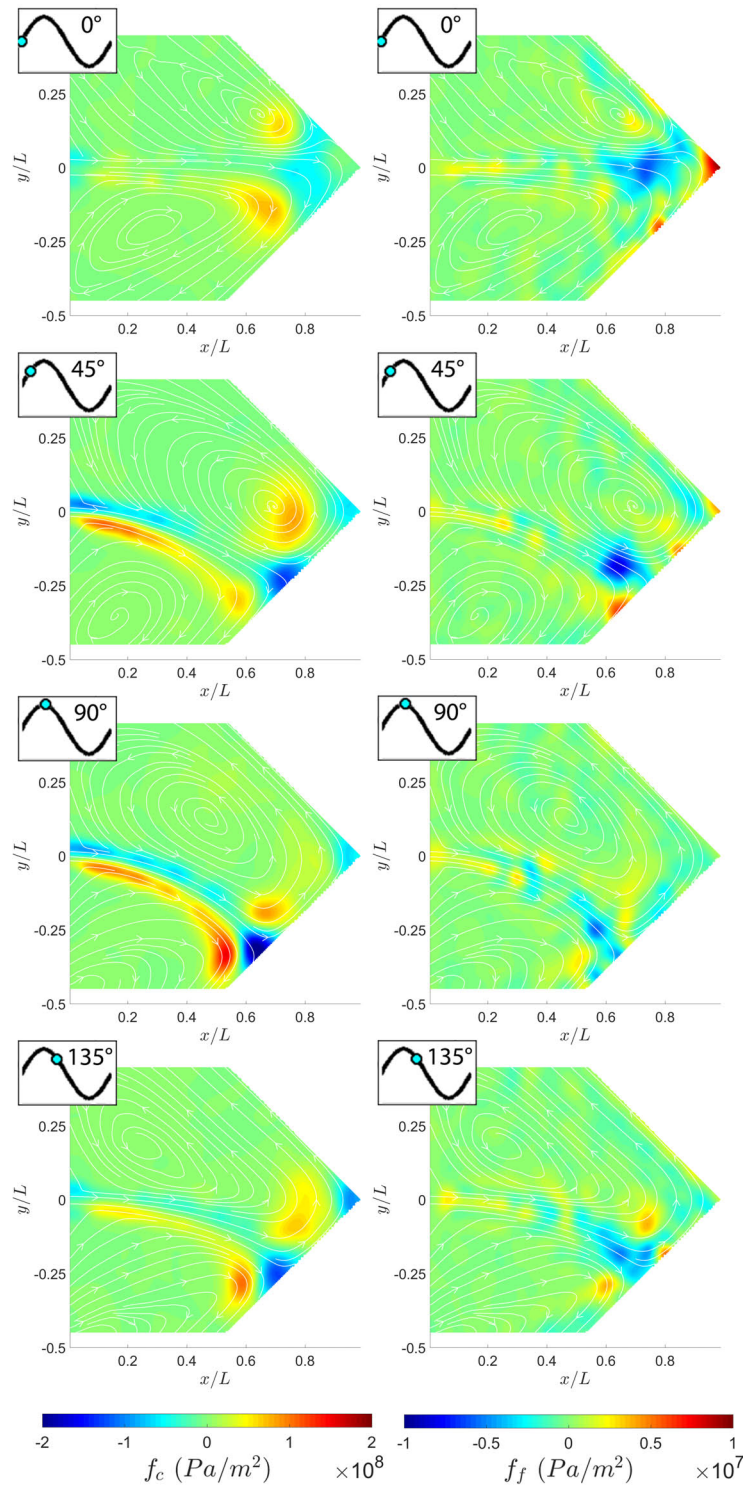
Figure 4.8: Comparison of the convective (f_c) (left) and the fluctuating (f_f) (right) source components of the pressure Poisson equation
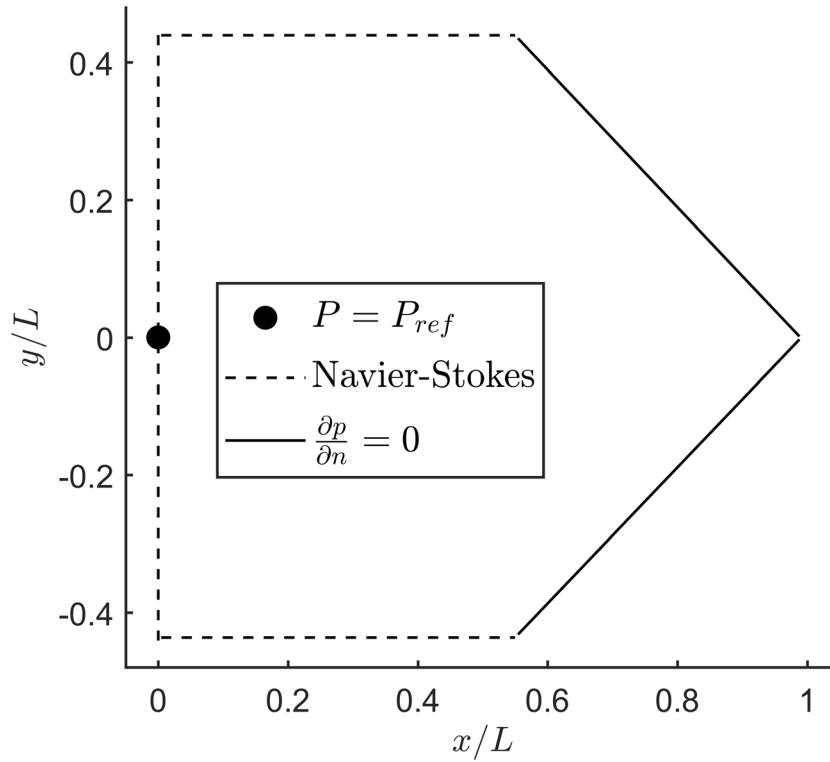
Figure 4.9: Boundary conditions imposed to solve pressure Poisson equation

4.4.2 Implementation of boundary conditions

To solve the pressure Poisson equation, a Gauss-Seidel solver is used with boundary conditions around the entire perimeter of the flow field which are calculated using the PIV measurements. As shown in Figure 4.9, while a Dirichlet boundary condition is applied at the jet exit, two types of Neumann boundary conditions are also applied, one at the region where the flow is open, and another along the v-shaped plate surface. The Dirichlet boundary condition is defined by setting the pressure near the jet exit equal to a reference pressure,

$$P = P_{ref} \tag{4.11}$$

One of the major error sources in the PIV-based pressure calculations originates from the error in velocity field measurements from the PIV used to solve the pressure Poisson equation, as discussed in Appendix A. In particular, the error is in the velocity gradient calculations, which for the current investigation is highest near the jet exit. Therefore, defining the reference pressure at the center of the jet exit will result in considerable error throughout the entire domain. Therefore, it is more appropriate to define the reference pressure over the immediate vicinity of the jet exit, which is achieved by defining the mean pressure over a radial distance of $1.5h$ from the center of the jet exit ($r = \sqrt{x^2 + y^2} \leq 1.5h$) equal to the reference pressure. Furthermore, PIV has difficulty obtaining measurements at the jet exit as a result of the high density of seeding particles and laser reflections at the nozzle lips. Therefore, the PIV vectors which do not yield high validation rates from the jet exit to $0.3h$ downstream are removed and not used in defining the reference pressure. Defining a Dirichlet boundary condition is necessary in the current analysis, as without one there is no reference pressure for the pressure field and therefore there is an infinite number of solutions to the pressure Poisson equation. It is especially important to define a reference pressure in the current investigation in order to compare the pressure field over the oscillation cycle. In particular, defining the references pressure allows for the time traces of the pressure field along the v-shaped plate to be compared with the fluctuating pressure measurements from the transducers. In order to compensate for the small variations in the time traces taken from the PIV-pressure data as a result of the pressure field referencing scheme, a function is used to model to the signal at each spatial location in the flow field which consists of the mean steady pressure ($\overline{p_s}$) and the fluctuating components associated with the fundamental

and its harmonics,

$$\overline{p} = \overline{p_s} + \sum A_i \sin(2\pi i f_n t - \phi_i) \qquad (4.12)$$

The ability of this equation to accurately describe the pressure data will be discussed further in Section 4.5. Nonetheless, the time traces from the PIV-pressure data will be shown to agree very well with the time signals from the transducers. In many other flow cases where the reference pressure is not defined near a location which high shear flow exists, such as when the far-field pressure characteristics are known, the influence of the reference pressure on the time traces from the PIV-pressure measurements will inevitably be less. In the current investigation, any of the time signals produced from the transducers could be used to reference the pressure field at each phase. However, one of the major benefits of the proposed pressure field mapping technique is that the detailed time-varying pressure field can be obtained without the requirement of any other direct pressure measurements, as often they are not easily obtainable. Therefore, it is necessary to reference the pressure field using only the jet exit region and avoid using any of the transducer signals, as they will only be used to evaluate the results. Nonetheless, even though referencing the pressure field in a high shear flow region impacted the jet impinging on a v-shaped plate and opposing planar jet investigations, most of the analysis of the pressure field used in the current investigation is concerned with pressure differentials across the jet columns. Therefore, this error does not impact this analysis as the pressure differential calculation is not influenced by the reference pressure.

The first type of Neumann boundary conditions is applied along the plate, which is

achieved by defining the pressure gradient normal to the boundary equal to zero,

$$\frac{\partial \overline{p}}{\partial n} = 0 \tag{4.13}$$

Where n defines the normal direction to the boundary. As a result of the plate being oriented $45°$ to the axes, the boundary condition can applied as $\frac{\partial \overline{p}}{\partial x} + \frac{\partial \overline{p}}{\partial y} = 0$ and $\frac{\partial \overline{p}}{\partial x} - \frac{\partial \overline{p}}{\partial y} = 0$ along the top and bottom half of the v-shaped plate, respectively.

The second type of Neumann boundary conditions which are applied along the perimeter of the flow field where the flow is open, is boundary conditions derived from the Navier-Stokes equations. Specifically, the Navier-Stokes equations are used to define the pressure gradient normal to the boundary. For example, along the vertical boundary on the left-hand side of the flow field, the pressure gradient is defined in the x-direction as,

$$\frac{\partial \overline{p}}{\partial x} = -\rho \frac{\partial \overline{u}}{\partial t} - \rho \left(\overline{u} \frac{\partial \overline{u}}{\partial x} + \overline{v} \frac{\partial \overline{u}}{\partial y} \right) + \mu \left(\frac{\partial^2 \overline{u}}{\partial x^2} + \frac{\partial^2 \overline{u}}{\partial y^2} \right) - \rho \left(\frac{\partial \overline{u'^2}}{\partial x} + \frac{\partial \overline{u'v'}}{\partial y} \right) \tag{4.14}$$

Similarly, along the horizontal boundary at the top and bottom of the flow field, the pressure gradient is defined in the y-direction as,

$$\frac{\partial \overline{p}}{\partial y} = -\rho \frac{\partial \overline{v}}{\partial t} - \rho \left(\overline{u} \frac{\partial \overline{v}}{\partial x} + \overline{v} \frac{\partial \overline{v}}{\partial y} \right) + \mu \left(\frac{\partial^2 \overline{v}}{\partial x^2} + \frac{\partial^2 \overline{v}}{\partial y^2} \right) - \rho \left(\frac{\partial \overline{v'^2}}{\partial y} + \frac{\partial \overline{u'v'}}{\partial x} \right) \tag{4.15}$$

With the exception of the transient term, each term from the Navier-Stokes equations shown above are directly obtainable from the phase-resolved velocity measurements, as PIV produces highly resolved spatial gradients. However, the transient term requires an understanding of how the phase-resolved mean flow field behaves over the oscillation cycle. To avoid the requirement of resolving many phases over the oscillation cycle to produce a high

enough resolution time signal to calculate the time gradients, the phase-resolved nature of the time signal is considered. In particular, the time signal at each point in space is defined by the steady mean velocity component ($\overline{u_s}$), and a series of fluctuating components associated with the higher harmonics,

$$\overline{u} = \overline{u_s} + \sum_1^N A_i \sin(2\pi i f_n t - \phi_i) \qquad (4.16)$$

Where f_n is the fundamental frequency component the PIV is phase-locked to, A_i and ϕ_i are the amplitude and phase components associated with the ith frequency component and N is the number of frequency components used to describe the oscillations. As discussed in Section 4.2, the mean flow field only consists of these fluctuating components as all other time scales and random fluctuations will be 'averaged out'. Figure 4.10 shows a sample of PIV velocity measurements over the oscillation cycle at a point in the flow field, starting with only the fundamental ($N = 1$) and subsequently adding harmonics ($N \geq 2$). The ability of Equation 4.16 to describe the time trace is shown to improve as the number of frequency components in the model (N) increases. The fundamental and first three harmonics ($N = 4$) are shown to be sufficient to accurately describe the velocity fluctuations. While $N = 4$ is used for all spatial locations, A_i and ϕ_i are uniquely determined for each spatial location in the flow field using a least-square fit. Subsequently, the time derivative can then be determined by differentiating Equation 4.16,

$$\frac{\partial \overline{u}}{\partial t} = \sum_1^N 2\pi i f_n A_i \cos(2\pi i f_n t - \phi_i) \qquad (4.17)$$

Each term in the Navier-Stokes boundary conditions will influence the pressure gradient defined along the boundary to varying extents. To better understand the influence of the
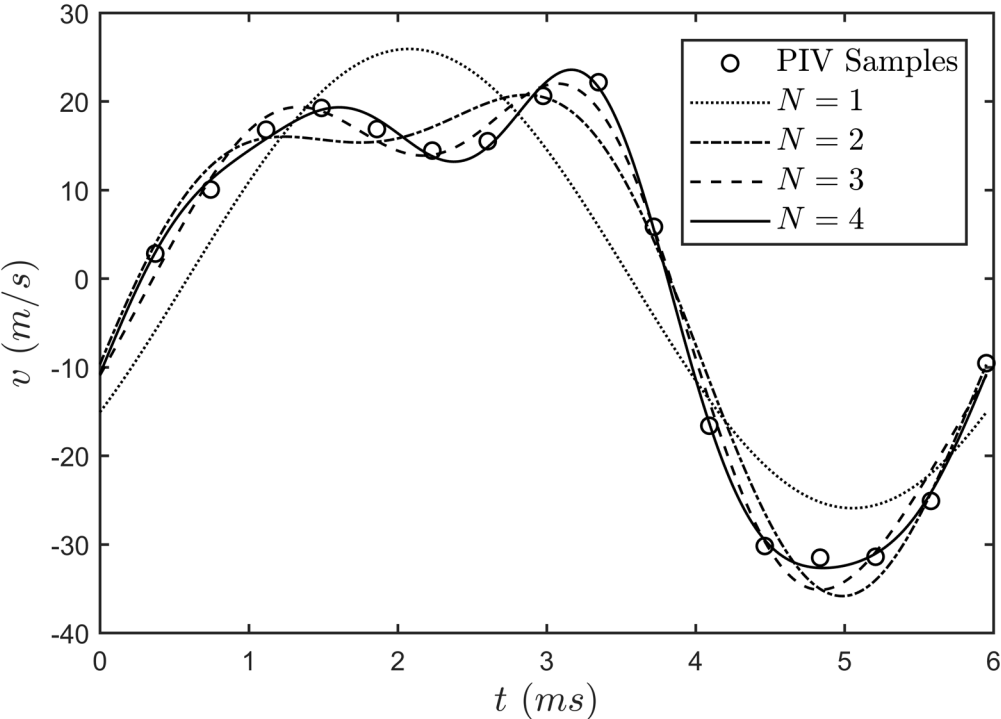
Figure 4.10: Goodness of fit with velocity time signal vs number of frequency components used

various sets of terms in these boundary equations, Equation 4.14 can be normalized as,

$$\frac{P_c}{\rho V^2}\frac{\partial \overline{p}^*}{\partial x^*} = -St_L\frac{\partial \overline{u}^*}{\partial t^*} - \left(\overline{u}^*\frac{\partial \overline{u}^*}{\partial x^*} + \overline{v}^*\frac{\partial \overline{u}^*}{\partial y^*}\right) + \frac{1}{Re_L}\left(\frac{\partial^2 \overline{u}^*}{\partial x^{*2}} + \frac{\partial^2 \overline{u}^*}{\partial y^{*2}}\right)$$
$$- \left(\frac{u'_c}{V}\right)^2\left(\frac{\partial \overline{u'^2}^*}{\partial x^*} + \frac{\partial \overline{u'v'}^*}{\partial y^*}\right) \quad (4.18)$$

where,

$$x^* = \frac{x}{L}, \quad y^* = \frac{y}{L}, \quad \overline{u}^* = \frac{\overline{u}}{V}, \quad \overline{v}^* = \frac{\overline{v}}{V},$$
$$\overline{u'^2}^* = \frac{\overline{u'^2}}{u'^2_c}, \quad \overline{v'^2}^* = \frac{\overline{v'^2}}{u'^2_c}, \quad \overline{u'v'}^* = \frac{\overline{u'v'}}{u'^2_c} \quad \text{and} \quad \overline{p}^* = \frac{\overline{p}}{P_c}$$

P_c is the characteristic pressure associated with the problem and the order of magnitude of the pressure field will be shown to be proportional to the dynamic head of the jet (i.e. $\frac{P_c}{\frac{1}{2}\rho V^2} \approx 1$). The transient term of the Navier-Stokes equations is shown to scale with the Strouhal number (St_L), which is earlier quoted as approximately 0.07. Therefore, this term should be small, however as will be shown below, it is the same order of magnitude as the convective terms near the boundaries. The viscous terms show to inversely scale with the Reynolds number ($Re_L = \frac{\rho V L}{\mu}$), which is approximately 2×10^5 for the current flow conditions, making the viscous terms very small. u'_c is the characteristic velocity scale associated with fluctuations from the phase-resolved mean flow. Typical values for the fluctuating velocities is approximately 30% of the jet exit velocity, however is much smaller in the boundary regions. Thus, $\left(\frac{u'_c}{V}\right)^2$ is approximately 10% and therefore it is not surprising that the below analysis shows the turbulent terms are not significant in the determination of the pressure gradient around the boundary.

To determine the true extent to which each term of the Navier-Stokes equations plays a

a)

b)

Figure 4.11: Components of Navier-Stokes used to define boundary conditions along left boundary below jet at a) 45° and b) 135°

role in the boundary conditions away from the plate, it is necessary to observe the influence of each term in these regions. In particular, Figure 4.11 shows the value of each term used to define the boundary condition along the left boundary below the jet exit ($y < 0$). Subset a) shows the variation in each term along the boundary for a phase of 45° in the oscillation cycle, which is the phase in the cycle when the jet has just passed the centerline and is moving downward. Subset b) shows the same variation, however for 135° in the cycle, when the jet has already reached its maximum deflection downward and is beginning its return to

the centerline. In both cases, the convective terms are dominated by the $\overline{v}\frac{\partial \overline{u}}{\partial y}$ term which is positive away from the jet exit and negative near the jet exit since the velocity gradient $\frac{\partial \overline{u}}{\partial y}$ varies as a result of the circulation zone. However, the transient term is positive over this region at 45° and negative at 135°, which is attributed to the difference in the orientation of the jet between these two phases. At 45° the jet is moving downward which is increasing the scale of the velocity field in the low half of the flow field, while at 135° the jet is moving back towards the centerline, resulting in the scale of the velocity in this region to decrease over time. Nonetheless, despite the previous scaling analysis, the transient term is shown to be of the same order of magnitude as the convective terms in this region. The viscous and turbulent terms on the other hand are very small, as expected.

The components of the Navier-stokes equation normal the bottom boundary is displayed in Figure 4.12. In this region, the convective terms are much larger and have an increased influence on the boundary condition, which is a result of the strong flow velocity along the plate as the jet is directed downward. The boundary layer flow which results from the flow passing along the plate creates a strongly negative $\overline{u}\frac{\partial \overline{v}}{\partial x}$ term, which dominates. The negative region extends further from the plate as the jet reaches is maximum deflection near 135°, as a result of the increased flow velocity directed along the plate. The sudden increase in the convective term near the plate is a result of the flow being forced to zero near the plate. While the transient terms are much smaller than the convective terms in this region, they are still significant. Despite the large time scale associated with the current problem, it is necessary to include the time-varying components of the boundary conditions in the pressure analysis.
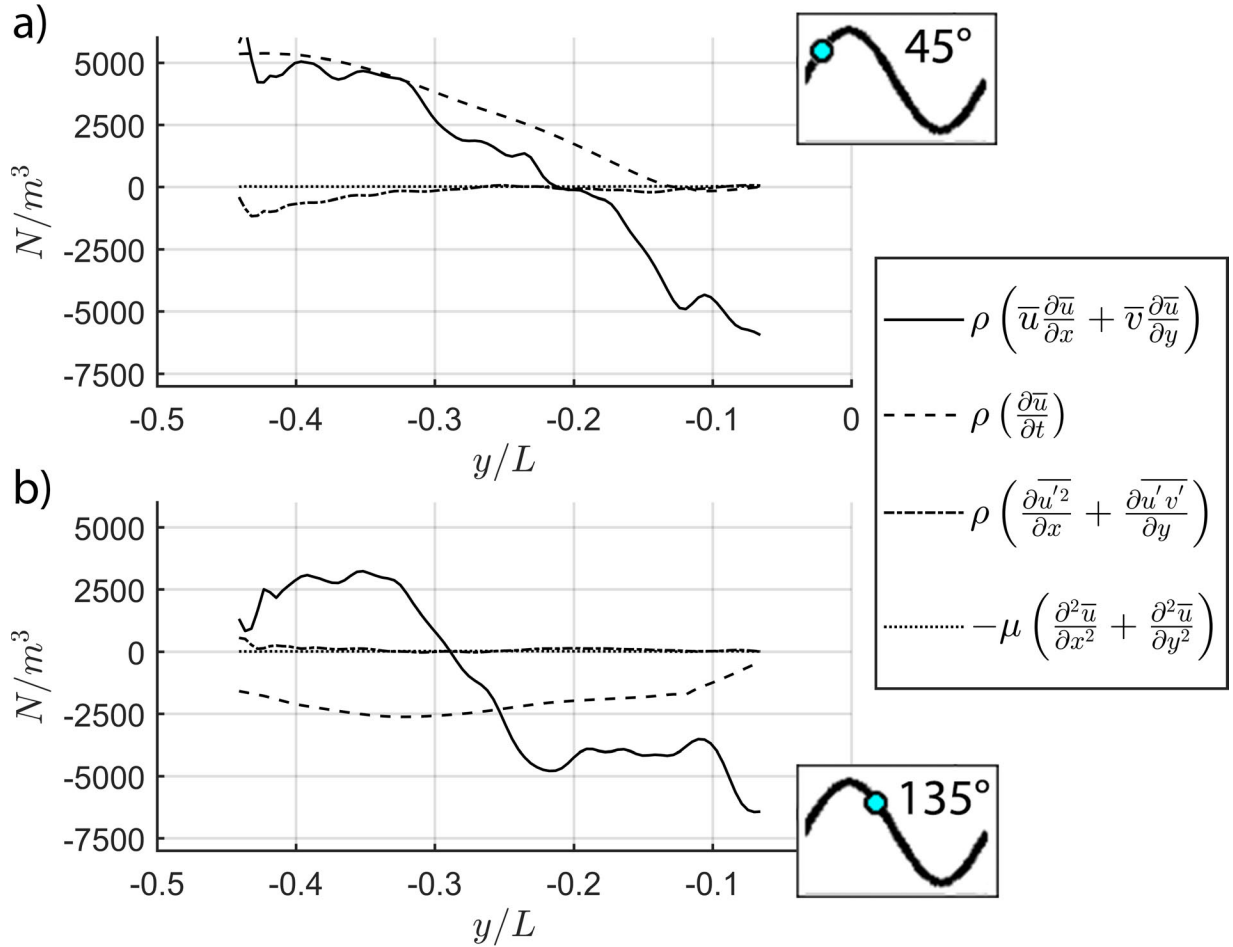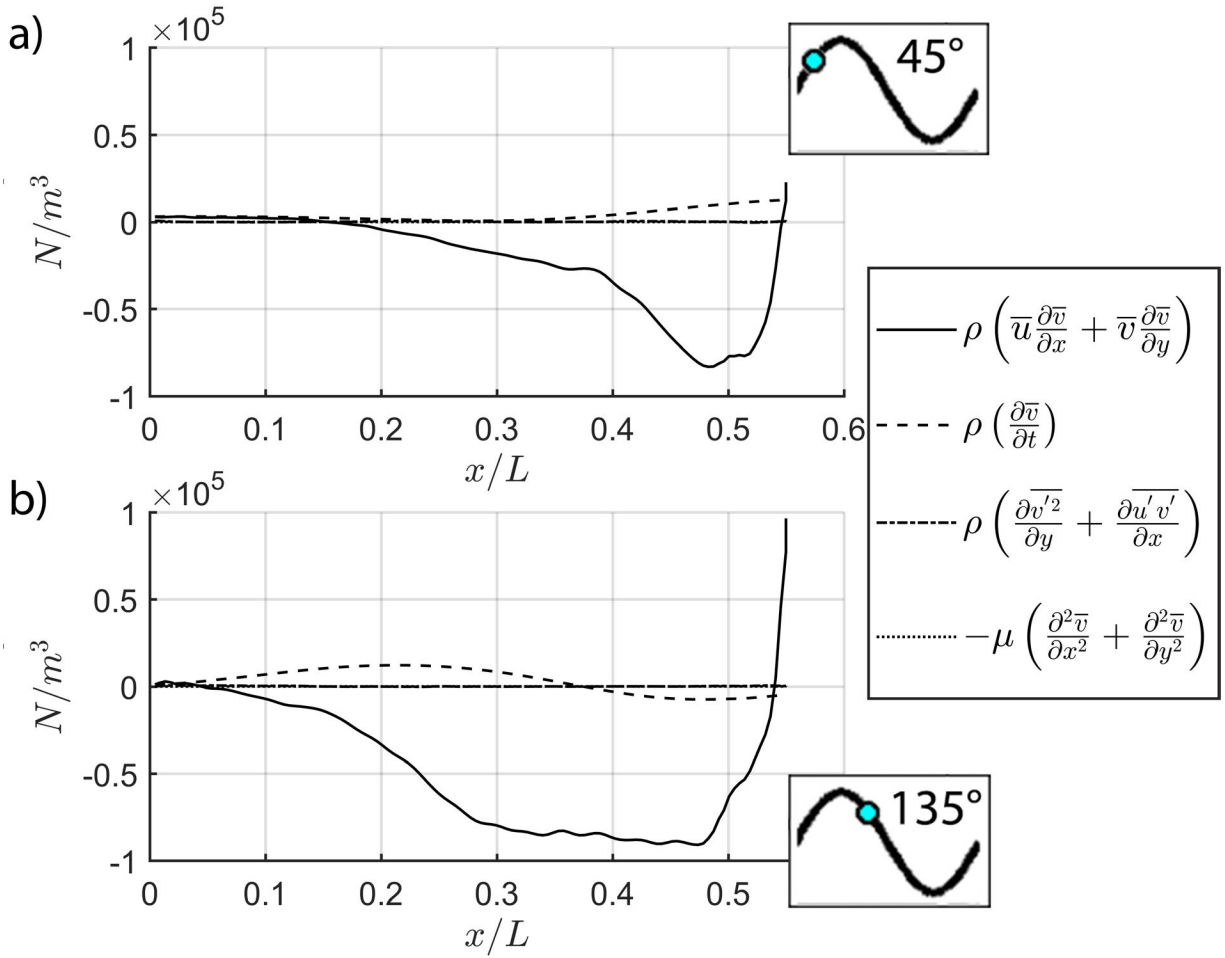
Figure 4.12: Components of Navier-Stokes used to define boundary conditions along bottom boundary at a) 45° and b) 135°
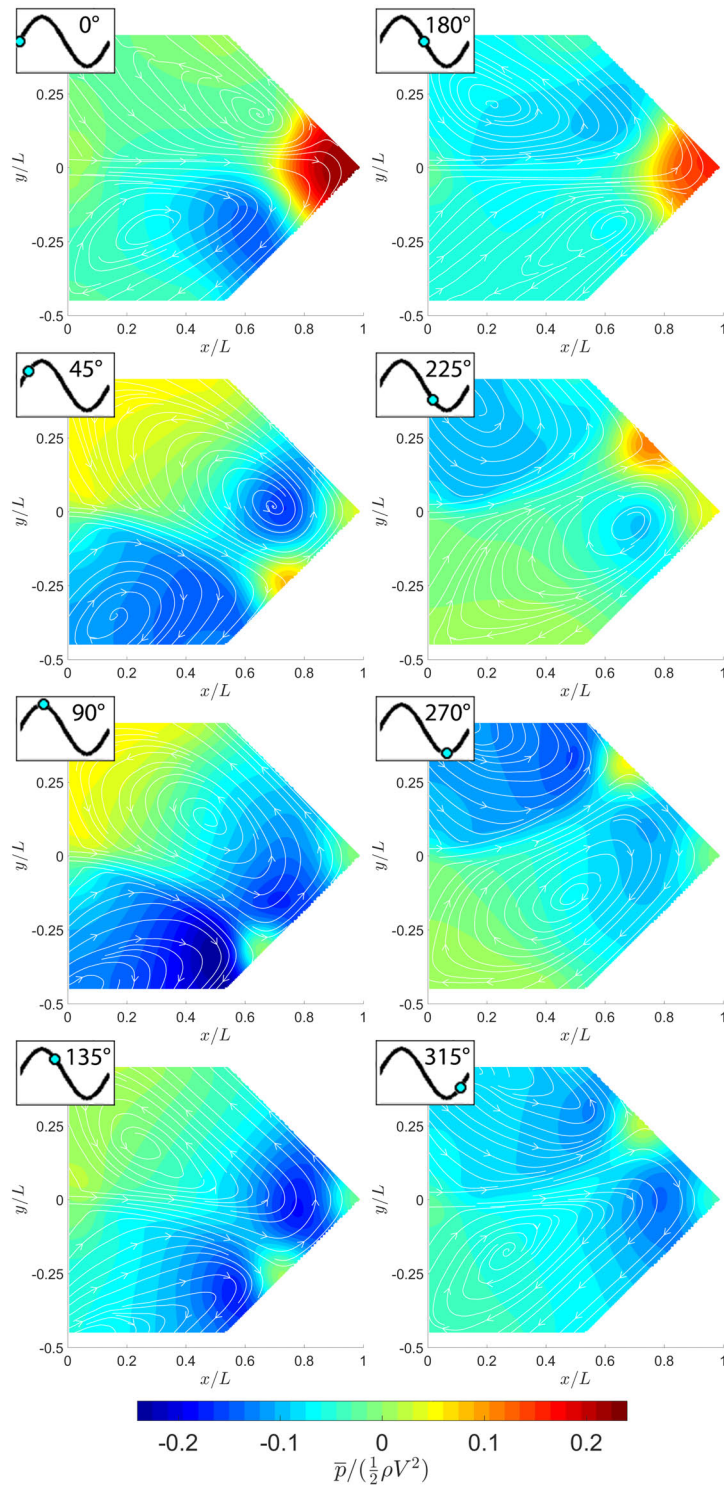
Figure 4.13: Phase-resolved pressure field with accompanying streamlines of jet impinging on v-shaped plate at eight phases in the oscillation cycle

4.4.3   Phase-resolved pressure field

Eight phases of the phase-resolved pressure field which is determined from the aforementioned PIV pressure field mapping technique is presented in Figure 4.13. Over the oscillation cycle, both a high-pressure region near impingement at the plate's surface, as well as low-pressure regions in the circulation zones are observed. The high-pressure region grows significantly as the jet impinges directly on the corner of the v-shaped plate, as a result of the large change in momentum of the fluid in this region. At this phase a saddle point exists, as the jet wants to deflect away from the centerline, but the direction is dependent on the flow conditions at the current phase in the oscillation cycle. The low-pressure regions in the circulation zones on either side of the jet are both observed throughout the oscillation cycle, however the top low-pressure region is strongest as the jet deflects upward, while the bottom is strongest as the jet deflects downward. The existence of the circulation zones generates pressure gradients across the initial region of the jet column which are similar in magnitude to the dynamic head of the jet ($\frac{1}{2}\rho V^2$). These pressure gradients are likely generating the driving force which is forcing the jet column back and forth. Later analysis of the opposing planar jets, in Chapter 5, will demonstrate very similar characteristics of the pressure field as shown here. While the high-pressure region is responsible for pushing the jet columns away from the centerline, it is the low-pressure regions which drive the jet column back toward, and ultimately across, the centerline. It is very likely that the same mechanism is playing a role in the case of the planar jet impinging on a v-shaped plate, however this is outside the scope of the present investigation and will not be discussed here. The PIV pressure field measurements will now be compared to the transducer measurements to confirm their viability.

4.5   Comparison with transducer measurements

The PIV pressure measurements along the plate will be compared to the transducer measurements, including both an evaluation of the raw time signals, as well as the spectral characteristics of the time traces. The averaged frequency spectra of all three transducer signals, including both the phase and amplitude, are presented previously in Figure 4.4. The signals of all three transducers are shown to be dominated by the fundamental frequency and first harmonic. While transducer 1 is shown to have a very strong first harmonic amplitude and transducer 2 is shown to have a strong fundamental amplitude, transducer 3 has smaller components of both. This is a result of the transducers being located along the plate in locations where the jet impinges on them twice, once and not at all, respectively.

The PIV pressure field over the oscillation cycle is sampled at the three locations along the plate where the transducers are located. A comparison of the time traces from the PIV data and the transducers is shown in Figure 4.14. To properly compare the time signals, it is more appropriate to find the phase-resolved mean pressure fluctuations for each of the transducer signals. To find this average representation of the fluctuating pressure signal, the averaged spectra in Figure 4.4 are reconstructed into time signals using an Inverse Fast-Fourier Transform. Approximately eight cycles of the jet deflection oscillations are shown as the period of the oscillations is approximately 5.9 ms. Observing the first transducer, two distinct fluctuations in the pressure signal can be seen per oscillation period. The peaks in the signal are relatively well defined, as they indicate the points in the oscillation cycle when the jet passes the transducer location, once on the way away from the centerline and once during its return. The second transducer only has one large fluctuation in the pressure signal per oscillation cycle, however the maximum in the pressure fluctuation has two smaller peaks. This is likely a result of the jet deflecting such that it impinges slightly past the transducer
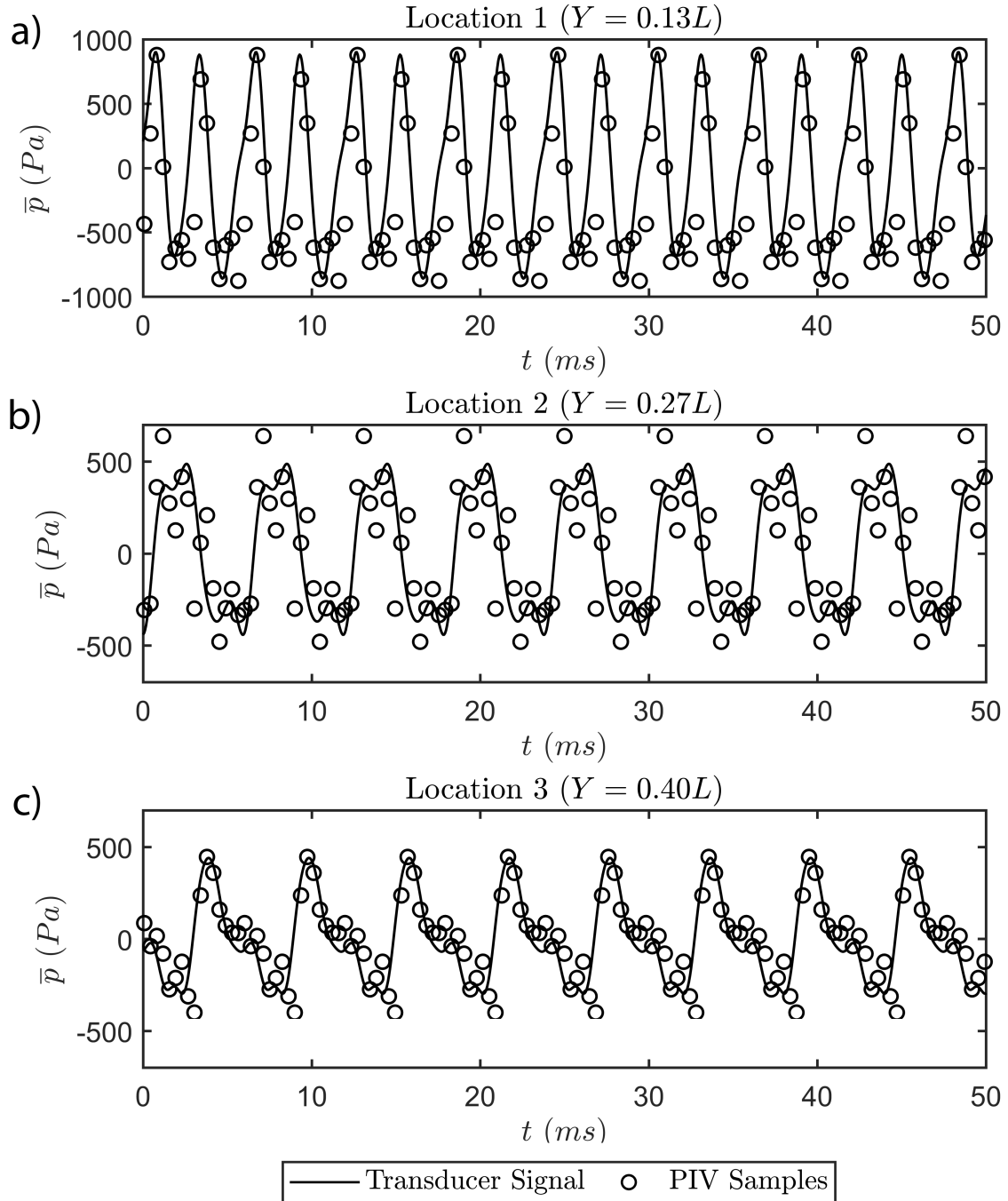
Figure 4.14: Time signals of transducer and PIV pressure measurements at location a) 1 b) 2 and c) 3

at its maximum deflection. Finally, the third transducer shows a minimum pressure as the jet reaches its maximum deflection upward. While this seems counterintuitive, review of the phase-resolved pressure field in Figure 4.13 shows the strong low-pressure region in the circulation zone near this transducer, which generates the pressure minimum in the time signal. The PIV samples appear to show very good agreement with the averaged transducer time signals, with the exception of the second transducer. While the overall trend appears to be consistent, with one large fluctuation in the pressure signal with two smaller peaks near the maximum, the size of the two peaks varies between the PIV and transducer measurements. Specifically, the two peaks in the PIV case, especially the first peak, is much larger than those observed in the transducer signals. This variation signifies a discrepancy between the magnitude of the first harmonic of the signals. It is difficult to assess the extent to which the measurements agree or disagree, simply by observing the time signals. Therefore, the spectra characteristics of the signals, including both amplitude and phase, will now be investigated.

Similar to the time traces of the velocity measurements, a function is used to model to the PIV pressure field measurements for each of these locations. The function consists again of the steady mean component $(\overline{p_s})$ and fluctuating components including the fundamental frequency and associated harmonics.

$$\overline{p} = \overline{p_s} + \sum_{1}^{N} A_i \sin(2\pi i f_n t - \phi_i) \tag{4.19}$$

Where f_n is the fundamental frequency of the oscillations which the PIV system is phase-locked to and A_i and ϕ_i are the amplitude and phase of the ith frequency component. Similar to the time-varying velocity calculations, the fundamental and first three harmonics ($N = 4$) are shown to sufficiently describe the pressure time traces for all three transducers, as indicated in Figure 4.15. The values of A_i and ϕ_i again are uniquely determined for each
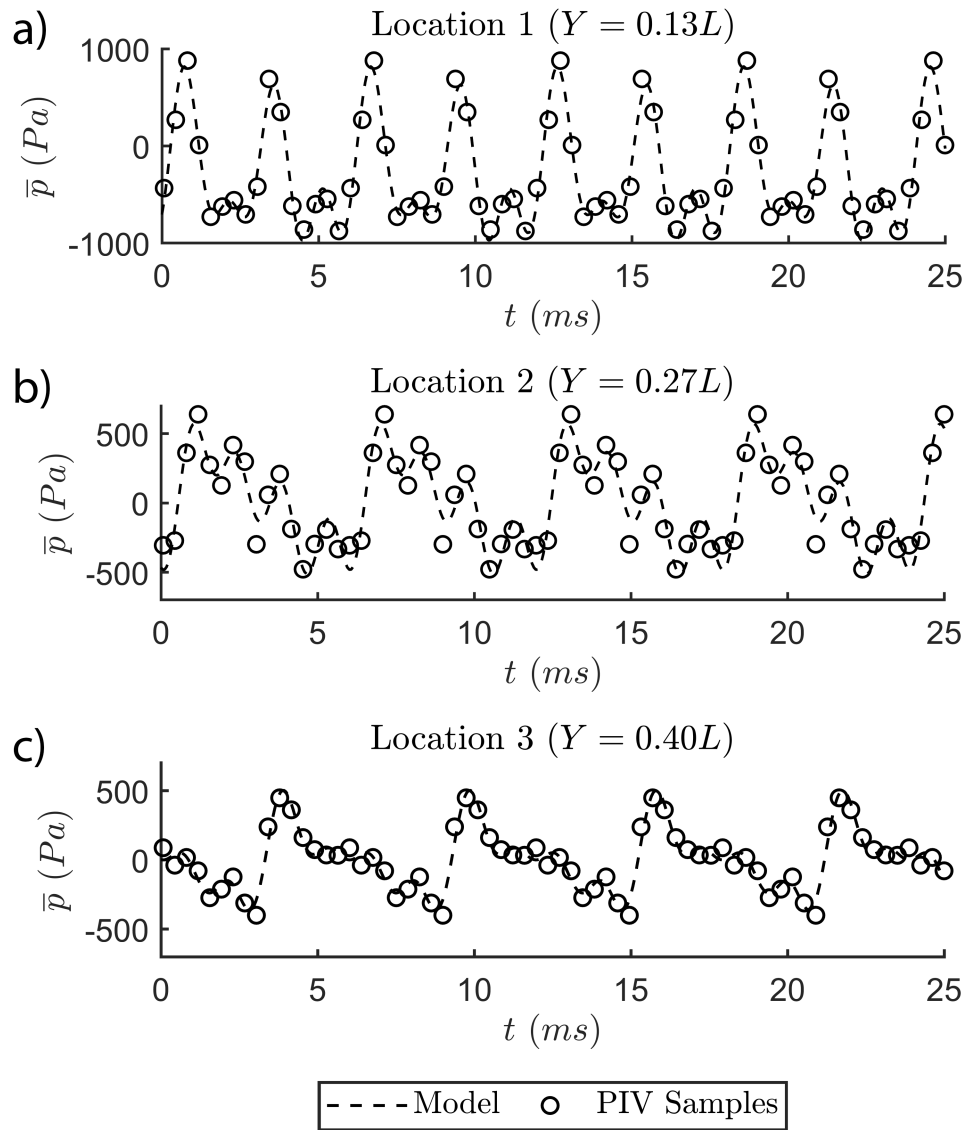
Figure 4.15: Fit of model to PIV samples for transducer locations a) 1 b) 2 and c) 3

spatial location in the pressure field using a least-square fit. Fitting the model equation is more appropriate than other methods of determining the spectra characteristics of the PIV samples, such as a Fast-Fourier Transform, as it helps reduce the artificial high frequency noise which is a result of the aforementioned small error in the referencing of the pressure field (discussed in Section 4.4.2).

The amplitude and phase of each component of the model equation for the PIV measurements can now be compared to the transducer spectra characteristics discussed earlier to better evaluate the effectiveness of the proposed PIV pressure field mapping technique to accurately predict the phase-resolved pressure field. A comparison of the amplitude and phase of the fundamental component is shown in Figure 4.16. Each transducer shows excellent agreement in both amplitude and phase, with only minimal variation in the phase of the third transducer. Therefore, this technique is shown to very accurately describe the fundamental oscillation characteristics which the system is phase-locked to. While still very good agreement is observed for the first harmonic component, Figure 4.17 shows significant variation in the amplitude and phase for the second transducer. This is indicative of the previous discussion of the variation in the time signals near the positive peak in the PIV and transducer measurements. The probable reason for the discrepancy at this location relates back to the previous discussion in Section 4.1.2, as the time signal of the second transducer shows intermittency. The intermittency is a result of the transducer being located precisely where the jet impinges along the plate as it reaches its maximum deflection. Figure 4.5 shows the variation in the number of defined peaks observed per oscillation cycle, which is indicative of the jet reaching slightly different amplitudes from one cycle to the next. Therefore, sometimes the jet passes the transducer twice, creating two well defined peaks at the maximum, while other times it only passes it once, resulting in one larger peak. This is likely the
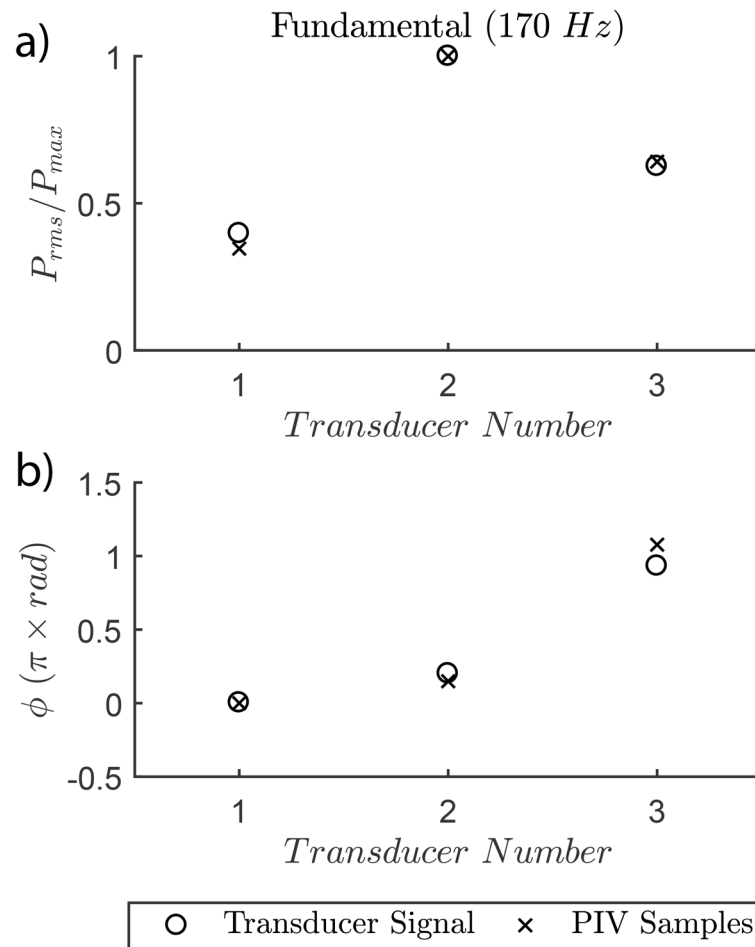
Figure 4.16: Comparison of amplitude and phase components of transducer and PIV signals for the fundamental frequency
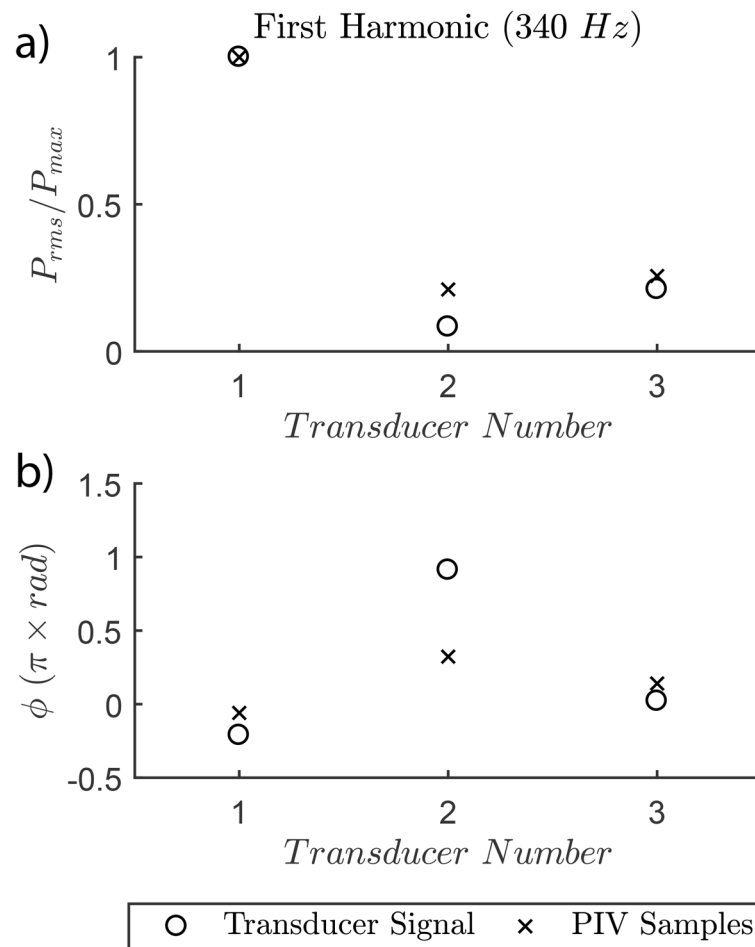
Figure 4.17: Comparison of amplitude and phase components of transducer and PIV signals for the first harmonic

reason for the discrepancy in the first harmonic component between these measurements for the second transducer location. Nonetheless, the amplitude of this component for the second transducer is relatively low and not an essential feature of the oscillations. The important aspects of the trend are captured very well by this technique, including the fundamental for all three transducers and the first harmonic for the first transducer.

4.6   Conclusion

An original PIV pressure field mapping technique is developed which allows for detailed characterization of the time-varying pressure field for flows which exhibit periodic characteristics, such as often the case in the area of fluid-structure-interaction and aeroacoustics. The technique utilizes the periodic characteristics of the flow field to decompose the velocity vectors into a periodic mean component which follows the oscillations, as well as a fluctuating component away from this mean motion. Careful formulation of the pressure Poisson equation and boundary conditions allows typical PIV systems with relatively low sampling rates to accurately describe high-speed flow oscillations. This is a unique benefit over existing methodologies as either very expensive and often unattainable PIV systems are required to quantify the time-varying characteristics, or the pressure field is assumed to be steady and the time-varying characteristics are ignored altogether. To better demonstrate the capabilities of the developed technique, the pressure field is calculated for the case of the planar jet impinging on a v-shaped plate and subsequently, the resulting time-varying pressure field characteristics are compared to transducer measurements along the boundary. Excellent agreement in the key features of the pressure field is observed between the PIV and transducer measurements, as both the raw time signals and spectral characteristics are

compared. The proposed technique will now be extended to the opposing planar jet oscillator to gain valuable insight into the self-sustaining mechanism, which until now, has not been well understood.

Chapter 5

Excitation mechanism

The fluid oscillations which arise as a result of the impingement of two counterflowing planar jets will now be investigated, with particular focus on the excitation mechanism responsible for sustaining the oscillations. Until now, little is known about the underlying mechanism which produces the asymmetric lateral jet deflection oscillations. While it is widely agreed upon in the literature that a high-pressure region forms in the impingement plane and is responsible for driving the jet columns away from the centerline, it is not clear what causes the jet columns to return to, and ultimately cross, the centerline. There has been a wide range of Strouhal numbers (St_L) reported by different investigators, however the values generally remain in a range of 0.1 to 0.2. These Strouhal numbers are much lower than many of the well-known jet oscillators in the literature, such as the jet-plate (Ho and Nosseir, 1981; Arthurs and Ziada, 2012, 2014), jet-edge (Powell, 1961; Staubli and Rockwell, 1987; Lin and Rockwell, 2001) or jet-slot (Ziada, 1995) oscillators. The low frequency nature of the oscillations suggests that a particle leaving the jet at an instance in the oscillation cycle will only remain in the immediate flow field for a short portion of the oscillation cycle. Therefore, it is likely that the pressure field is synchronizing the motion of the jets over the oscillation

cycle and ultimately playing an essential role in sustaining the oscillations. Thus, the time-varying pressure field is the primary focus in investigating the underlying mechanism. After first reviewing the impact of the jet exit velocity, impingement distance and slot width on the response characteristics of the opposing planar jets, phase-resolved flow measurements will be presented. Details of the fluid behaviour are then discussed and a unique mechanism which drives the jet oscillations is presented. The phase-resolved pressure field is then determined using the technique outlined in Chapter 4. Finally, the impact of the slot width, or the aspect ratio, on the oscillations, as well as on the sound-source characteristics, are discussed.

5.1   Acoustics response characteristics

Opposing planar jets are known to exhibit strong, robust and repeatable oscillations over a wide range of flow parameters. In general, these oscillations are difficult to disrupt and do not demonstrate many of the characteristics observed by well-known classical jet oscillators. Most notably, the opposing planar jets oscillate at a frequency over an order of magnitude lower than other jet oscillators and do not exhibit any frequency jumps to higher modes of oscillation. Furthermore, there has been some discrepancy in the literature regarding the reported Strouhal number of the opposing planar jet oscillations. While all the Strouhal numbers are much lower than the aforementioned classical oscillators, the values range from approximately 0.1 to 0.2. However, each reported measurement of the Strouhal number (outlined in Table 2.1) has been for a relatively narrow range of parameters. Therefore, prior to investigating the underlying mechanism, a more comprehensive parametric analysis of the acoustic response characteristics has been performed to help shed light on possible explanations for the variation in the reported Strouhal numbers. After reviewing the impact of the impingement ratio $(\frac{L}{h})$ and jet exit velocity (V) on the acoustic response, a unique

trend will be presented as the impact of the aspect ratio of the jets ($\frac{W}{h}$) is investigated. For the purposes of this investigation, the slot width of each jet, as well as the jet exit velocities, will remain the same as they are varied together.

5.1.1   Typical acoustic response

The opposing planar jets radiate a periodic tone associated with the global flow oscillations, which is audible in the far-field. Figure 5.1 a) shows sample averaged frequency spectra of the far-field noise produced by the opposing planar jets for a select few cases with varying impingement distances (L) and jet exit velocities (V). The measurement equipment and procedure used to determine the averaged spectra are discussed in Section 3.2.3. All the cases shown are for planar jets with a slot width (h) of 2 mm, resulting in an aspect ratio ($\frac{W}{h}$) of 50. Hereafter, the case with a slot width of 2 mm, an impingement distance of 80 mm and a jet exit velocity of 90 m/s is adopted as the 'base case', as much of the analysis will first be discussed in terms of this case and then extended to determine the impact of varying each parameter. The base case results in an oscillation frequency of 131 Hz and the amplitude is relatively low as compared to some of the other cases shown in this figure. The impact of doubling the impingement distance is observed in the figure as well, as the amplitude of oscillation is similar to the base case, but the frequency of oscillation is approximately half (60 Hz). The third spectra presented here indicates the impact of doubling the jet exit velocity, as the amplitude is approximately four times that of the base case and the frequency of oscillations is double (247 Hz). Finally, the impact of doubling both the impingement distance and jet exit velocity is shown to generate a tone with approximately four times the amplitude once again, however a similar but slightly lower oscillation frequency of 113 Hz is produced. There does appear to be small harmonics for

96
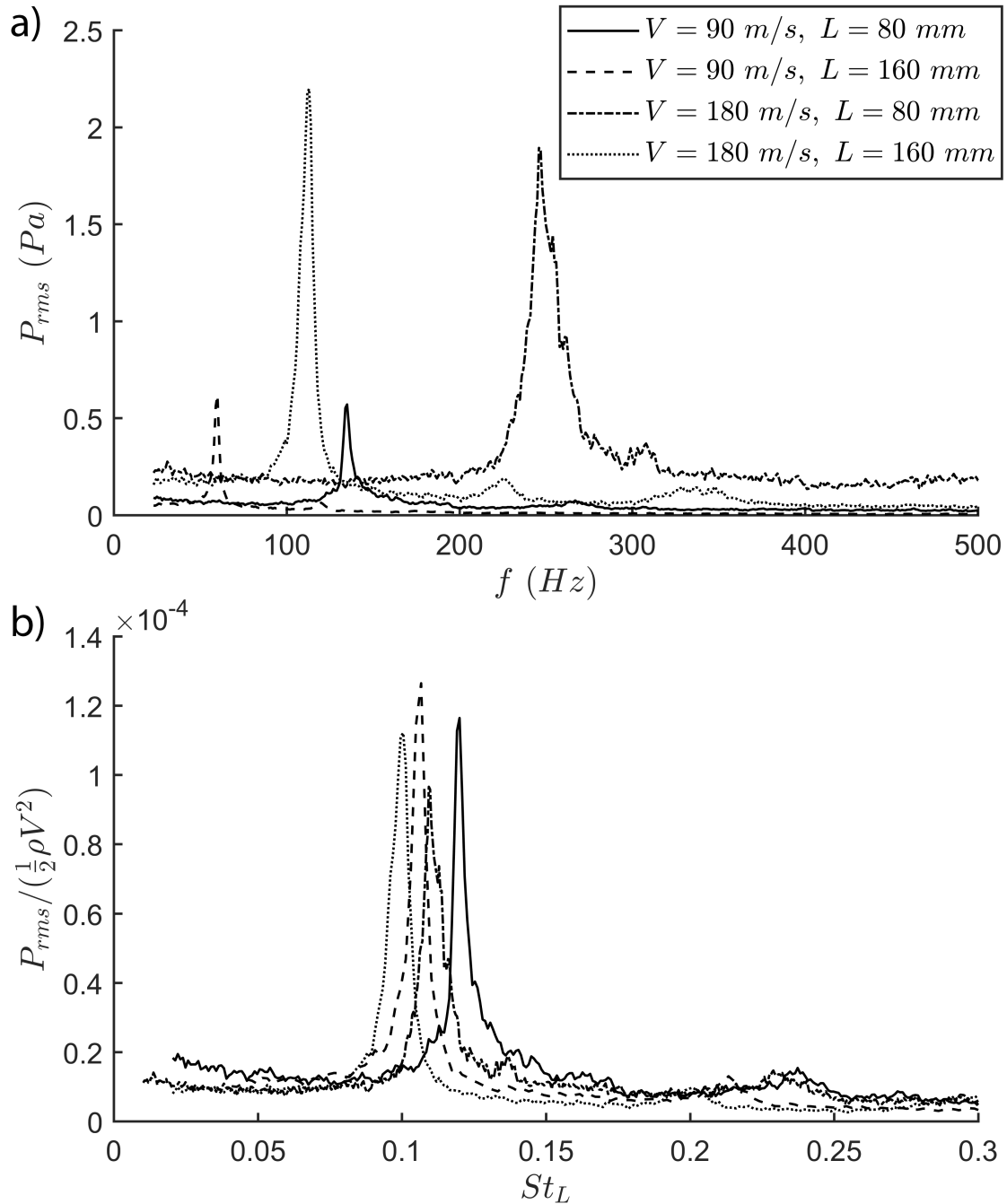
Figure 5.1: a) Dimensionalized and b) non-dimensionalized frequency spectrum of acoustic pressure for a select few parametric cases ($h = 2\ mm$)

some of the cases, however they are very weak relative to the fundamental. While all the spectra are defined by a distinct peak at the fundamental frequency, the amplitude and frequency of oscillation varies significantly. To help explain this variation, Figure 5.1 b) shows the impact of non-dimensionalizing the frequency using Strouhal number, as well as the reduced pressure determined by dividing the pressure amplitude by the dynamic head of the jet exit flow (defined by Equations 3.2 and 3.3). While the slight variation observed in the reduced pressure amplitude is not surprising, there does appear to be considerable variation in the Strouhal number of the fundamental tone for each case. To better understand this variation, the impact of varying the impingement distance and jet exit velocity will now be more comprehensively investigated.

To gain a detailed depiction of the variation in the oscillation frequency and corresponding Strouhal number over a more comprehensive range of flow parameters, the impingement distance (L) is varied from 12 to 400 mm and the jet exit velocity (V) is varied between 90, 135 and 180 m/s, while a jet aspect ratio of 50 is maintained. The resulting variation in the oscillation frequency is presented in Figure 5.2 a), as the frequency appears to inversely scale with the impingement distance and is positively correlated to the jet exit velocity. This is indicative of a typical Strouhal relationship, as Figure 5.2 b) shows excellent agreement in the variation of the Strouhal number with the impingement ratio for various jet exit velocities. However, the Strouhal number does appear to vary over the range of impingement distances investigated. In particular, the Strouhal number gets larger for smaller values of impingement distance as it reaches a maximum of approximately 0.15 at an impingement ratio of 12. For larger values of impingement ratio (> 75) the Strouhal number appears to converge to approximately 0.10. The increased Strouhal number for smaller impingement ratios will be shown in the following analysis to be a result of the impact of the jet core on
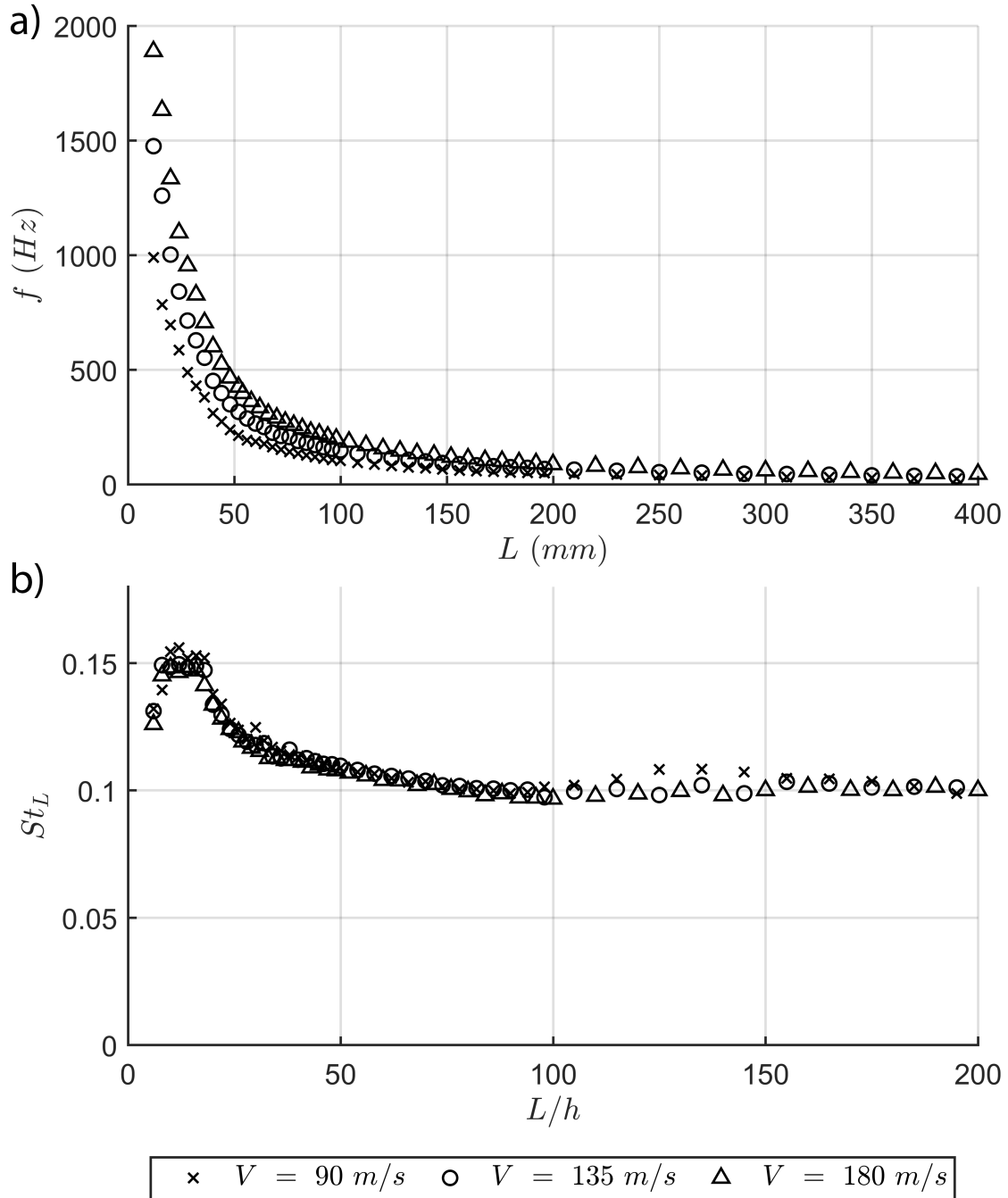
Figure 5.2: Impact of varying jet exit velocity on a) the impingement distance vs oscillation frequency and b) impingement ratio vs Strouhal number ($h = 2\ mm$)
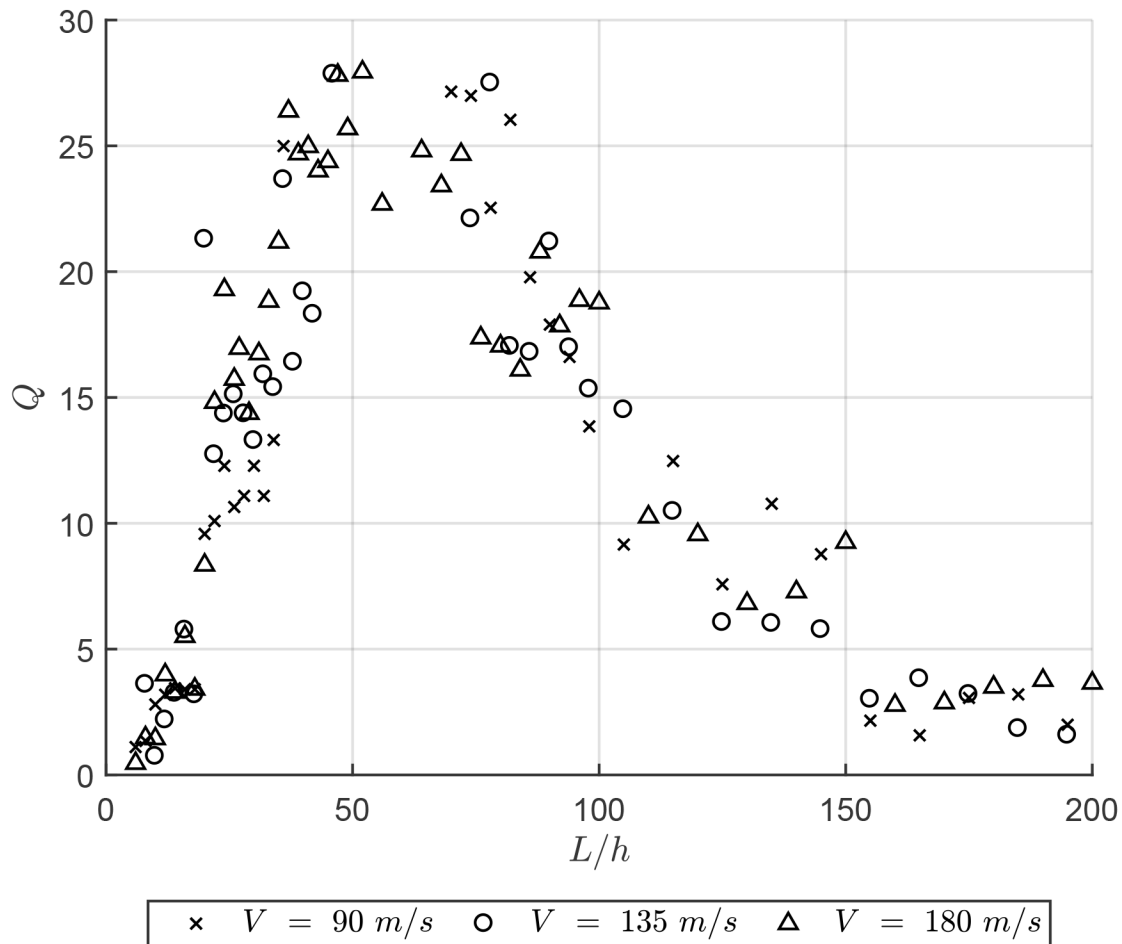
Figure 5.3: Quality factor of acoustic pressure for varying impingement ratio and jet exit velocity ($h = 2\ mm$)

the effective impingement distance. However, the sudden decrease in the Strouhal number as the impingement ratio gets very small (< 11) can be attributed to the decay in the ability of the oscillations to persist at smaller impingement distances as the jet columns are too stiff to deflect far enough to sustain the mechanism. This is illustrated by observing the quality factor of the acoustic pressure measurements in Figure 5.3, where the quality factor

is defined as,

$$Q = \frac{f_0}{f_u - f_l} \tag{5.1}$$

Where f_0 is the resonant frequency measured at the peak in the spectrum and f_u and f_l are the frequencies above and below the resonant frequency, respectively, where the power amplitude drops to one-half of the resonant value. The quality factor appears to be largest for impingement ratios of approximately 50. As the impingement ratio gets larger, the quality factor slowly decreases as a result of the three-dimensional effects of the jets beginning to cause it to lose some coherence prior to reaching the impingement plane. Furthermore, for smaller values of impingement ratio, there is a sudden reduction in the quality of the noise radiated as a result of the jets not being able to deflect as far and inhibiting the jets from consistently deflecting upon one another. As the impingement ratio gets very small (< 11), the quality factor approaches zero and the frequency of oscillation diminishes, which continues until the oscillations are no longer observed for impingement ratios less than 6. This is a result of the distance between the jets being so small that the cores do not allow the jets to deflect far enough to sustain the oscillations.

To investigate the impact of the existence of the jet cores on the oscillation frequency, the length of the jet cores must first be determined. Figure 5.4 shows the centerline velocity downstream of each jet for a select few cases with varying impingement distance and jet exit velocity. The velocity profiles are the steady mean velocity profiles as they are measured using the average velocity profile taken from 300 PIV measurements at random instances throughout the oscillation cycle. The length of the core is observed by the initial flat region of the velocity profiles and is measured by finding the downstream distance where the centerline velocity decays to 99% of the jet exit velocity. For the various cases studied with PIV, the core
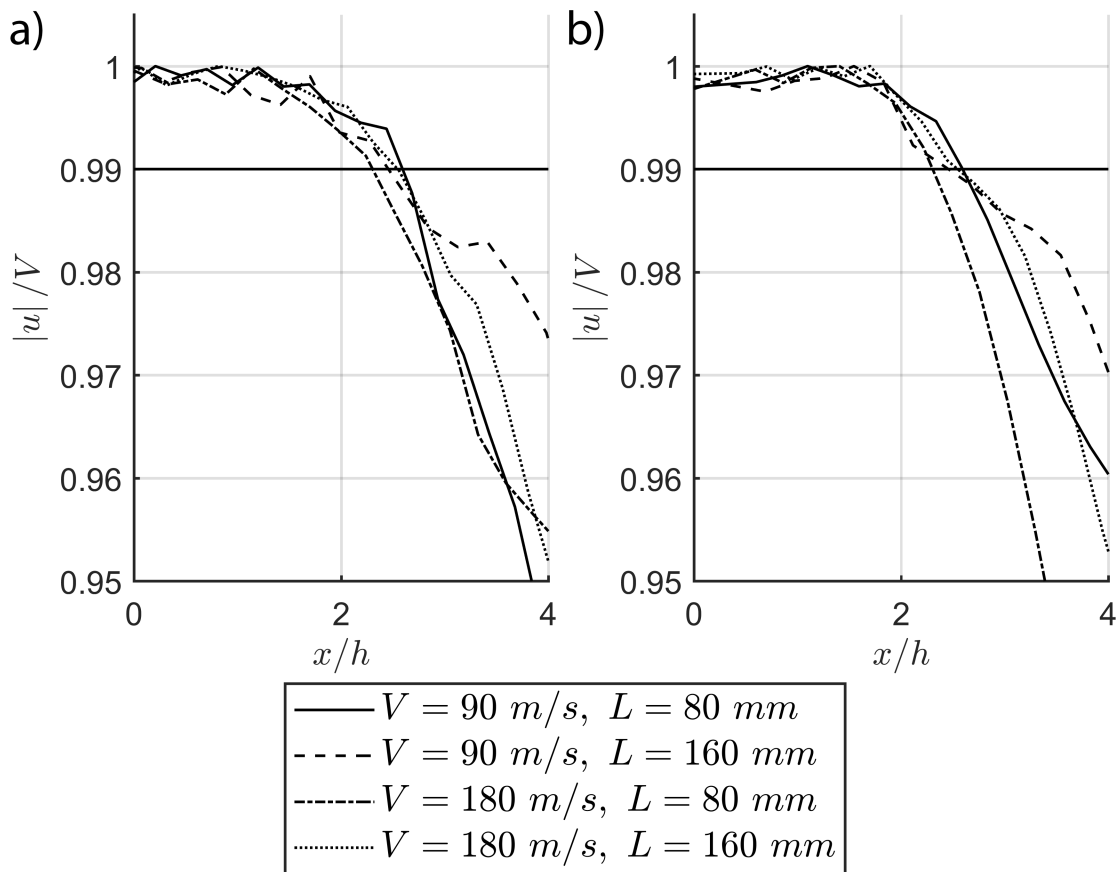
Figure 5.4: Centerline velocity of the time-averaged flow field of the a) left jet and b) right jet for a select few cases ($h = 2\ mm$)

length only varied by approximately $\pm 0.3h$ from the mean value of $2.6h$. The core lengths are then considered in calculating an effective impingement distance (L_e), by subtracting them from the total impingement length to determine the distance between the end of the two jet cores.

$$L_e = L - 2 \times 2.6h \tag{5.2}$$

A revised Strouhal number can then be determined.

$$St_{L_e} = \frac{f L_e}{V} \tag{5.3}$$

Figure 5.5 shows the variation in the Strouhal number based on the effective impingement length for various impingement ratios and jet exit velocities. A more consistent Strouhal number is observed over the range of impingement ratios investigated as it remains a constant value of approximately 0.10. The Strouhal number at lower values of impingement ratio (< 16) are shown to deviate from the trend as a result of the aforementioned inability of the jets to sustain repeatable and coherent oscillations at shorter impingement distances.

5.1.2   Effect of jet aspect ratio

While previous investigations have reported Strouhal numbers over ranges of impingement distance and jet exit velocity, very little is known about the impact of varying the aspect ratio of the jets. The only investigation to date considering the impact of the aspect ratio on the opposing planar jet oscillations is Tu *et al.* (2014a), who presented a small subset of results at low Reynolds numbers which suggested that increasing the aspect ratio extended the oscillation period. This is conducted for small aspect ratios (6-20), where three-dimensional
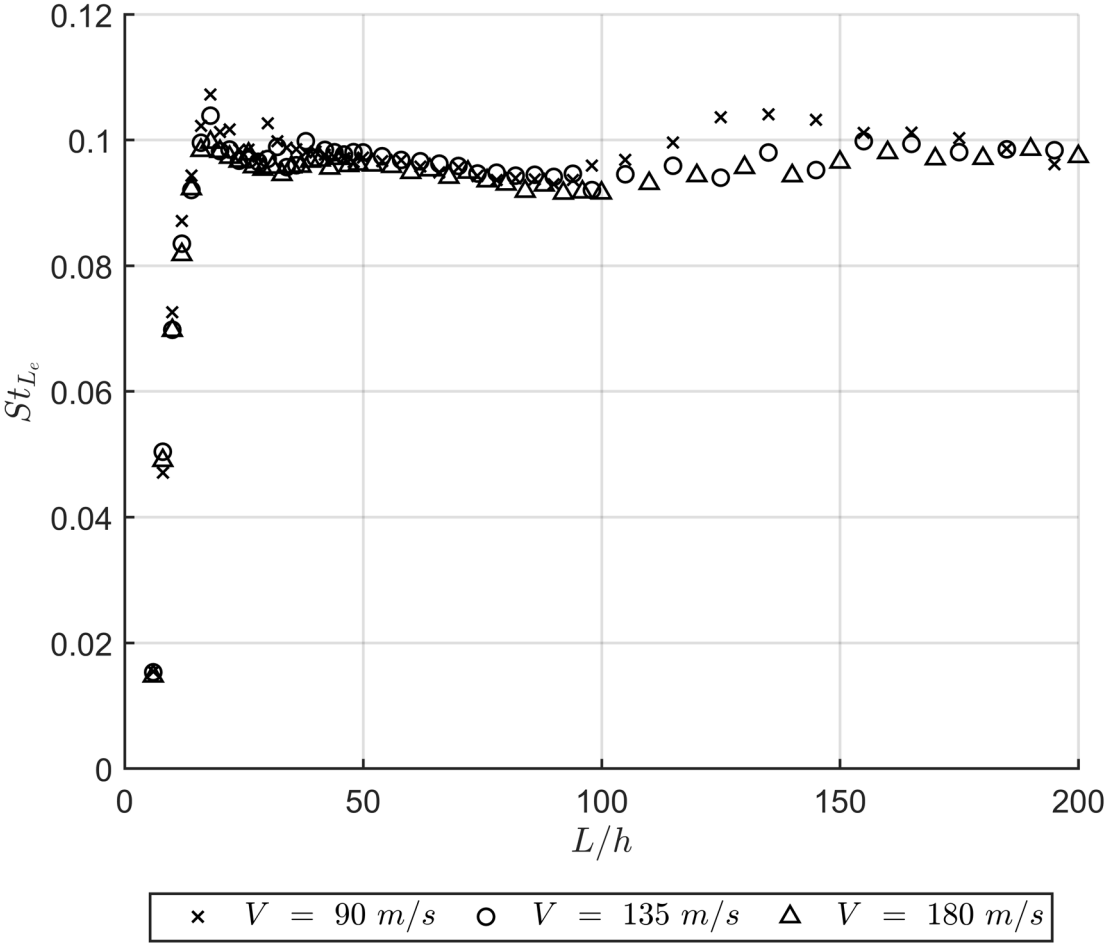
Figure 5.5: Strouhal number based on effective impingement length (St_{L_e}) for varying impingement ratio and jet exit velocity ($h = 2\ mm$)
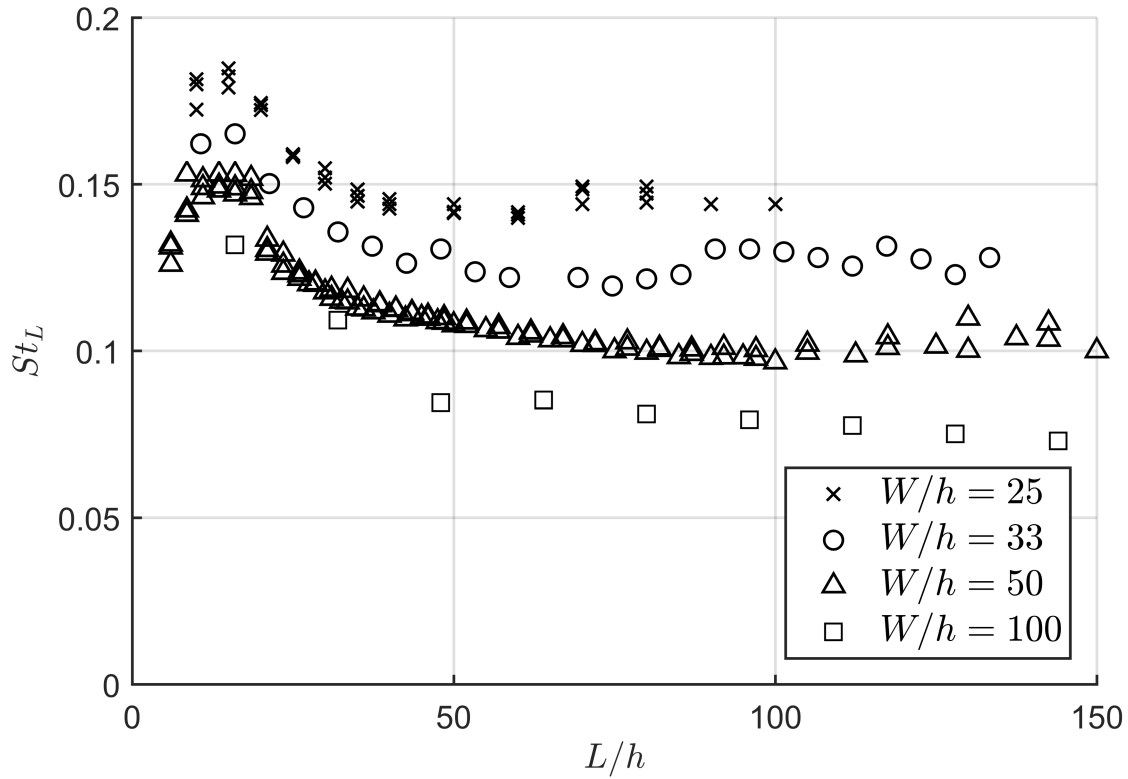
Figure 5.6: Strouhal number of oscillations for varying impingement ratio and jet aspect ratio

effects would be expected to play a prominent role. All other investigations reported in the literature have assumed that the aspect ratio will have negligible impact on the oscillation frequency, as long as it is sufficiently large. However, as will now be discussed, this may not necessarily be the case. For the current investigation, the span of the jet (W) remained a constant value of 100 mm, while the slot width (h) is varied from 1 to 4 mm, resulting in aspect ratios ($\frac{W}{h}$) as high as 100 and as low as 25. While the smallest aspect ratio investigated here is slightly less than the recommended aspect ratio of 30 to maintain two-dimensionality for planar jets (Deo *et al.*, 2007), the investigation will extend into a range of jets which are strongly two-dimensional. The influence of the aspect ratio on the Strouhal number of the oscillations is revealed in Figure 5.6. While a similar variation in the Strouhal number
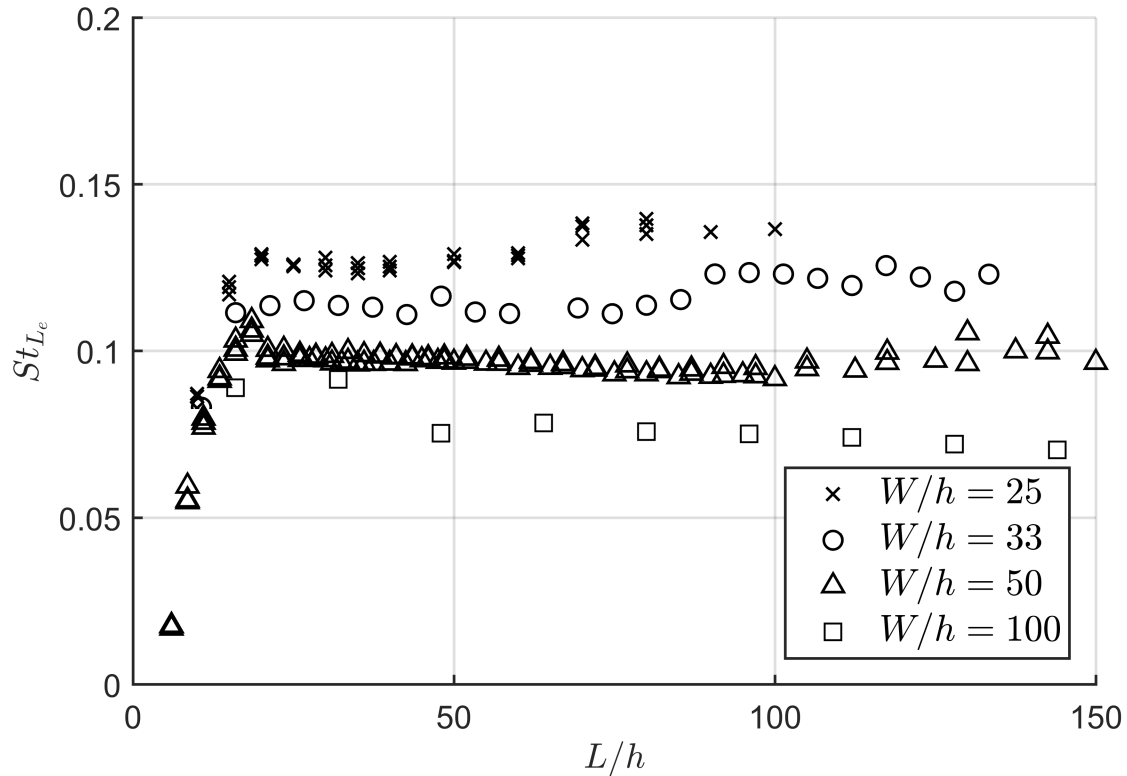
Figure 5.7: Strouhal number of oscillations based on effective impingement distance (L_e) for varying impingement ratio and aspect ratio

relative to the impingement ratio is observed for each jet aspect ratio, the observed Strouhal number consistently decreases as the aspect ratio increases.

To better understand the influence of the jet aspect ratio on the Strouhal number, similar analysis to that conducted in Section 5.1.1 can be conducted here by determining the effective impingement distance by compensating for the jet core lengths. Figure 5.7 shows the variation in the Strouhal number, calculated using the effective impingement length, for different jet aspect ratios. Similar to the previous discussion, the Strouhal number remains relatively constant for a given aspect ratio over the range of impingement ratios above 16. While using the effective impingement length slightly reduces the variation in the Strouhal number, the impact of the aspect ratio is still apparent. For the smallest aspect ratio case of

25, the Strouhal number is approximately 0.13, while for the largest aspect ratio of 100, the Strouhal number is approximately 0.075. Interestingly, even as the aspect ratio gets larger, the variation in the aspect ratio continues to impact the observed Strouhal number. One would expect that as the aspect ratio of the jets gets sufficiently large, the Strouhal number will begin to converge to a specific value. However, a significant variation is observed even as the jet aspect ratio is varied from 50 to 100. Section 5.4 will reveal some interesting trends in the oscillation mechanism and associated fluid dynamics as the aspect ratio of the jets is varied, which will provide valuable insight as to why the jet aspect ratio impacts the oscillation frequency.

5.1.3   Comparison to current literature

The differences existing in the reported Strouhal numbers in the literature is likely, or at least partly, a result of the range of jet aspect ratios used throughout the investigations. Table 2.1 outlines the range of parameters investigated in each study in the literature reporting upon the opposing planar jet oscillator, as well as the reported Strouhal numbers. Interestingly, a similar trend in the reported Strouhal numbers with the aspect ratios of the jets used is observed. In particular, the studies by Li *et al.* (2013) and Tu *et al.* (2014a) use jets with very small aspect ratios and observed the largest Strouhal numbers of approximately 0.20. As the aspect ratios of the jets get slightly larger, such as for the case in Denshchikov *et al.* (1978, 1983) and Li *et al.* (2011), the Strouhal number decreases to a slightly lower value of 0.17. Hassaballa and Ziada (2015) use very large aspect ratio jets and observed a much smaller Strouhal number of approximately 0.12. While it is very difficult to definitively show that this is the only influencing factor in the range of reported Strouhal numbers, as a result of the wide range of impingement distances and jet exit velocities used, it is very likely playing

a large part in this variation.

5.2   Proposed mechanism

The mechanism which sustains the opposing planar jet oscillations will now be addressed. A number of unique features of the flow field will be discussed with regards to their role in the underlying mechanism, with specific focus on the circulation zones in each quadrant of the flow field, which form, grow and dissipate once per oscillation cycle. These circulation zones will be shown to be an essential feature which allows the oscillations to exist in a repeatable and robust manner. Furthermore, Chapter 6 will attempt to disrupt the development and convection of these regions as a proposed mitigation strategy. The opposing planar jet oscillations are largely divided into two processes which occur twice per oscillation cycle. The first of which is the initial deflection of the jet columns away from the centerline in an asymmetric pattern. The high-pressure region which forms in the impingement plane is shown to play an important role in the deflection process, as the high-pressure region pushes the jet columns away from the centerline. However, the low-pressure regions which form in the circulation zones will also be shown to drive the jet columns away from the centerline and furthermore, allow them to remain at their maximum deflection for a short time before returning back towards the centerline. The second process occurs as the circulation zones convect away and the jet columns return to the centerline. During this time, two new circulation zones form near the centerline and will be shown to be responsible for driving the jet columns back toward, and ultimately across, the centerline, where the process then repeats. The phase-resolved velocity and pressure fields will now be presented, with specific focus on the various features which are synchronized with the oscillations. Following is an investigation into the role of each of these features with regards to sustaining the underlying

mechanism.

5.2.1   Phase-resolved flow field

The phase-resolved velocity measurements presented in the current section will be for the aforementioned 'base case', consisting of an impingement distance (L) of 80 mm, jet exit velocity (V) of 90 m/s and slot width (h) of 2 mm, resulting in an aspect ratio of 50. The frequency of oscillation which results, and subsequently is used to phase-lock the PIV system, is 131 Hz, which corresponds to a Strouhal number of 0.12. Details of the PIV system used and the phase-locking technique are provided in Section 3.3. The PIV system is triggered using the microphone signal with a bandpass filter applied containing high and low pass cut-off frequencies of 89.0 Hz and 192.8 Hz, respectively. A set of 200 PIV measurements are taken at each of 16 evenly spaced phases in the oscillation cycle, which are presented in Figure 5.8 with the velocity magnitude contours and accompanying streamlines indicating the flow pattern at each phase. The anticipated antisymmetric jet column oscillations once in each direction per oscillation cycle are clearly observed. A variety of circulation zones are observed throughout the oscillation cycle, including a circulation zone which forms in the impingement region each half cycle as the jets reach their maximum deflection (i.e. at 90° in Figure 5.8). Shortly after this central circulation zone forms, it splits into two smaller circulation zones on opposing quadrants of the flow field (i.e. at 135° in Figure 5.8). The result is a circulation zone which forms, grows in strength, and dissipates in each quadrant of the flow per oscillation cycle.

The process begins as the jets directly oppose one another, as at 0° in the oscillation cycle the jets are oriented along the common centerline and impinge upon one another. At this phase, the left jet is moving downwards, while the right jet is moving upwards. The
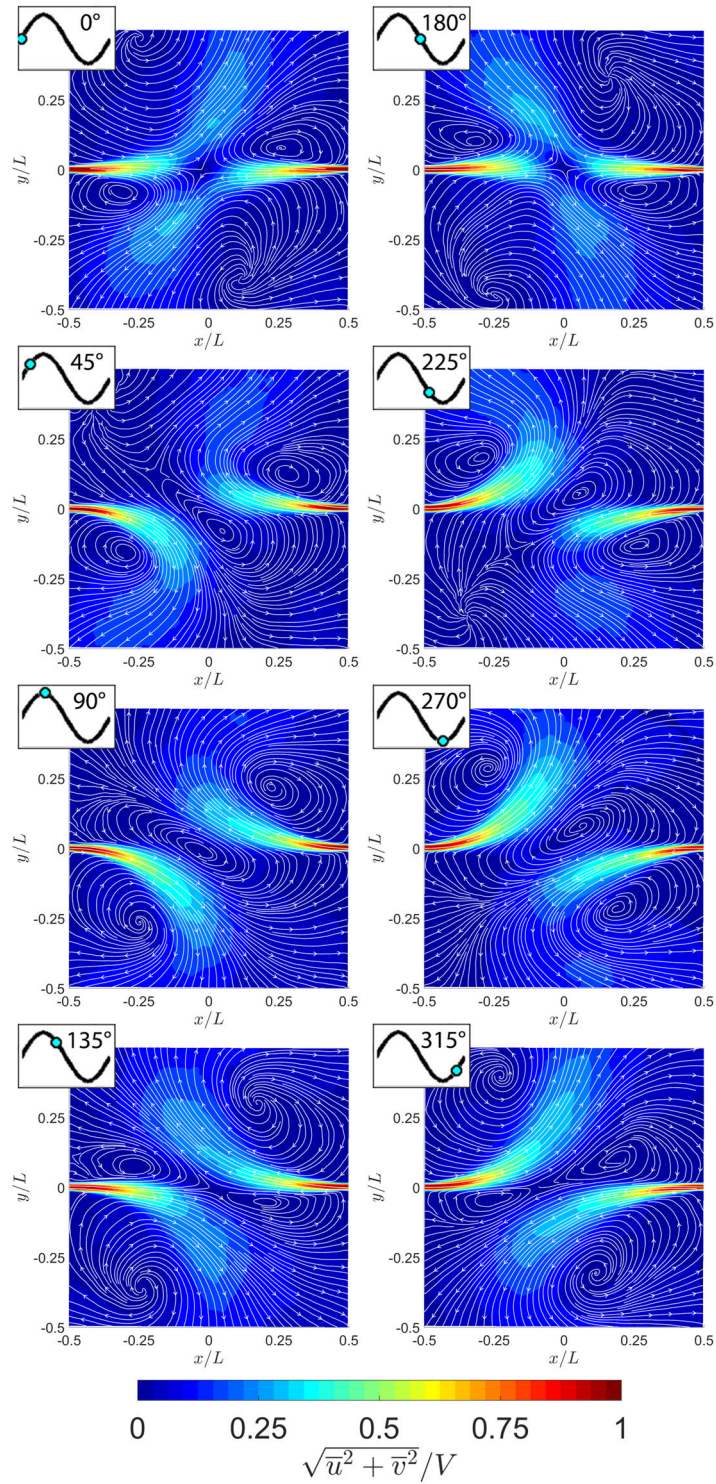
Figure 5.8: Phase-resolved velocity field with accompanying streamlines of opposing jets at eight phases in the oscillation cycle

key asymmetries in the flow field which indicate the direction each jet is travelling are the strong circulation zones which lead each of the jet columns. In particular, there is a strong circulation zone below the left jet and another one above the right jet. In the following section, these circulation zones will be shown to generate low-pressure regions which are responsible for pulling the jet columns back toward, and ultimately across, the centerline. As the oscillation cycle continues, the existence of these circulation zones, in conjunction with high-pressure at impingement, drives the jet columns away from the centerline. At approximately 90° in the oscillation cycle, the jets reach their maximum deflection and one large circulation zone appears between the two jets in the center of the flow field. Shortly after, at approximately 135° in the oscillation cycle, the circulation zones in the top right and bottom left begin to dissipate as they convect away from the jet columns. This results in the low-pressure regions in these circulation zones to dissipate as well and the jets begin to return back towards the centerline. As the jets approach one another, the large circulation zone in the center of the flow field splits into two smaller circulation zones, one above the left jet and one below the right jet. These circulation zones will eventually generate the new low-pressure regions which lead the motion of the jet columns. The circulation zones grow in strength as the jets approach the centerline, which continues until the jet passes the centerline at approximately 180° in the oscillation cycle. The jets begin to deflect away in the opposite directions and the process repeats itself. Astonishingly, despite the high-speed flow of the jets relative to the oscillation frequency, the jets return to the centerline in an organized and repeatable manner and do not chaotically flip orientation. One would expect the high-pressure region forming in the impingement plane as the jets approach one another to prevent the jets from returning to the centerline in this organized fashion. Despite the growth of this high-pressure region, the jets do return to the centerline, as the circulation

zones in each quadrant of the flow field will be shown to play an essential role in this process. The same analysis is performed for a variety of impingement distances, jet exit velocities and jet aspect ratios, and the same oscillation characteristics are observed. The impact of these characteristics and possible explanation for the variation in the Strouhal number will be discussed in Section 5.4.

5.2.2   Phase-resolved pressure field

The phase-resolved pressure field is determined using the same process discussed in Chapter 4 for the jet impinging on a v-shaped plate, as the phase-resolved velocity data is used to solve the pressure Poisson equation. However, the boundary conditions imposed are slightly different as a result of no physical boundaries existing in the flow field. As shown in Figure 5.9, the Navier-Stokes equations are once again used to define Neumann boundary conditions around the perimeter of the flow field, as the pressure gradient is defined normal to the boundary. Dirichlet boundary conditions are also once again defined at the jet exits by setting the mean pressure over a $1.5h$ radial distance from the jet exit to a specified reference pressure. For more information on the calculation of the various terms of the Navier-Stokes Equations, including the time gradients, as well as details of the PIV pressure field mapping technique, the reader is referred to Chapter 4.

Eight phases of the phase-resolved pressure field are presented in Figure 5.10, with the contours indicating the mean time-varying pressure field and the accompanying velocity streamlines illustrating the flow field which exist at each phase. Both the high-pressure region which forms as the jets impinge on one another, as well as the low-pressure regions in the circulation zones in each quadrant of the flow, are clearly observed at various phases in the oscillation cycle. These low-pressure regions appear to grow in strength and dissipate with
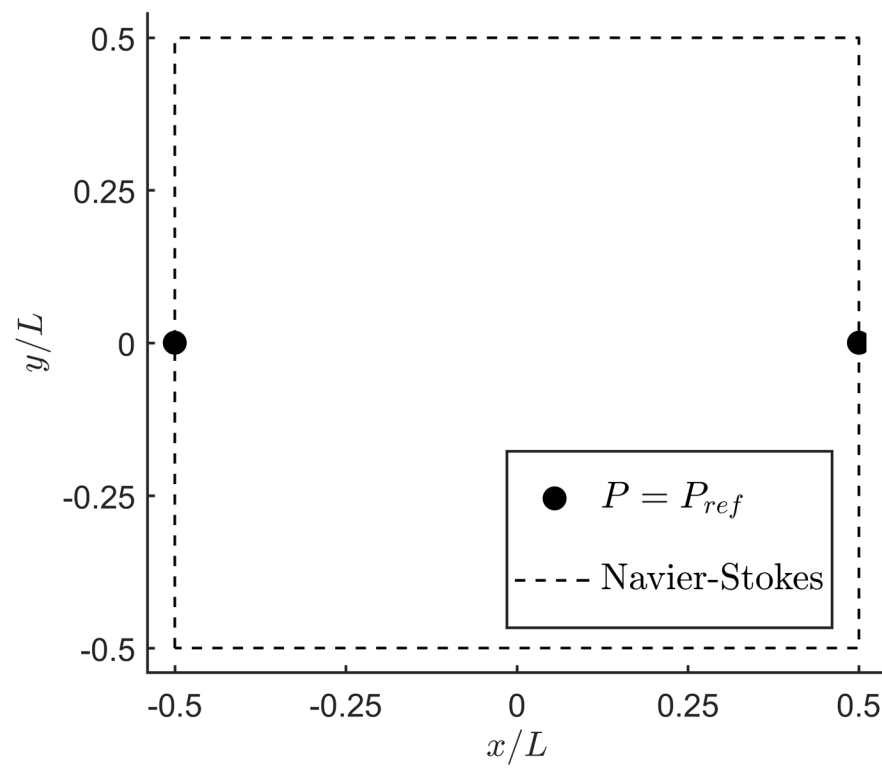
Figure 5.9: Boundary conditions imposed to solve pressure Poisson equation for opposing jets
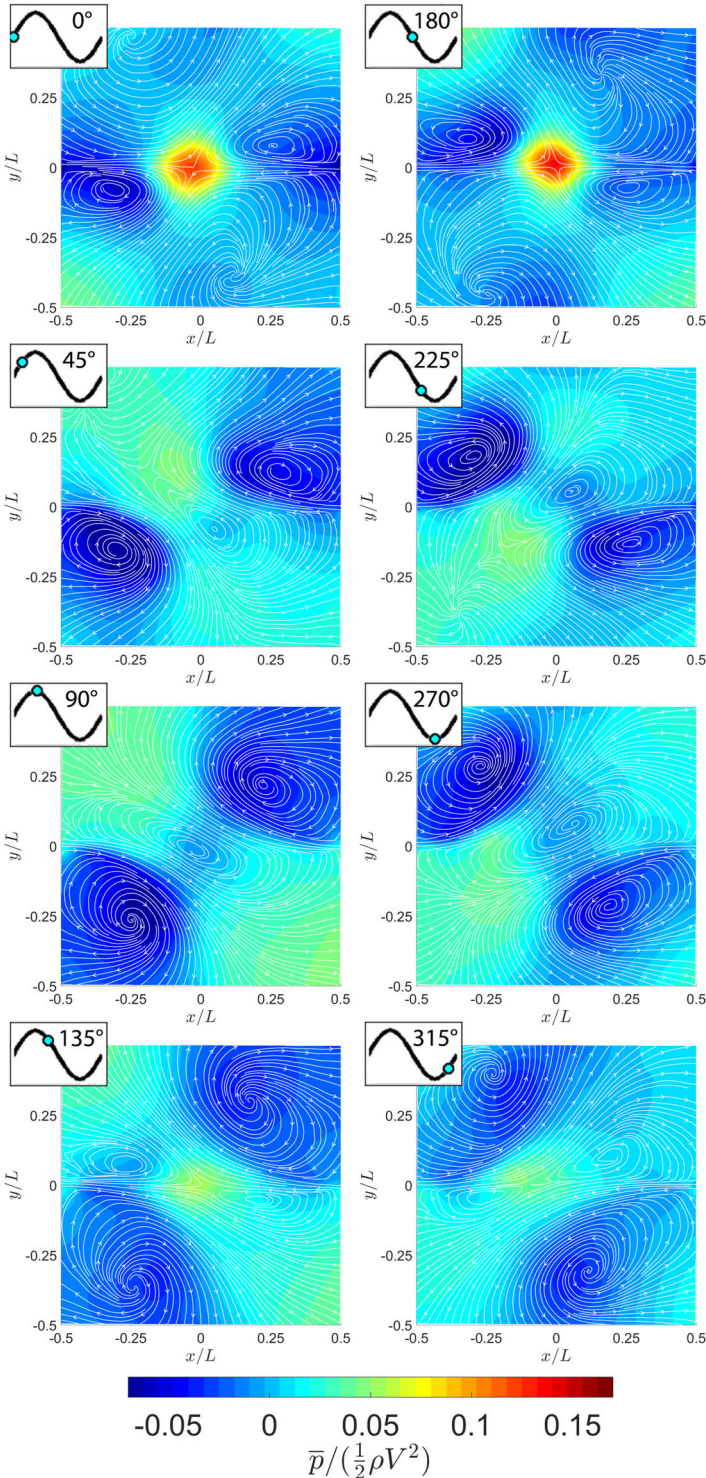
Figure 5.10: Phase-resolved pressure field with accompanying velocity streamlines of opposing jets at eight phases in the oscillation cycle

the circulation zones. At 0° in the oscillation cycle, as the jets impinge on one another, the high-pressure region is observed in the impingement plane. The aforementioned circulation zones below the left jet and above the right jet also appear to be giving way to strong low-pressure regions. However, the low Strouhal number associated with the oscillation cycle suggests that a particle leaving the jet will only remain in the immediate flow vicinity for a very short portion of the oscillation cycle. At this phase in the oscillation cycle, a particle leaving the jet exit will be forced to either travel upward or downward as a result of the high-pressure region downstream. However, the existence of the circulation zones will create a pressure gradient which drives a particle leaving the left jet downward and a particle leaving the right jet upward. The role of the high-pressure region at the impingement location and the pressure gradient across the jet created by the circulation zones will be discussed in more detail in Section 5.3. As the oscillation cycle continues, the low-pressure regions grow in strength and the jets continue to deflect away from the centerline. As the jets reach their maximum deflection at approximately 90°, the circulation zones below the left jet and above the right jet begin to dissipate. As these circulation zones dissipate, the associated low-pressure regions begin to weaken as well, and the jets begin to return to the centerline and the new circulation zones leading the jet columns form. Interestingly, at approximately 135° in the oscillation cycle, the high-pressure region in the center of the flow field begins to grow once again, yet the jets continue to approach the centerline. As will now be discussed in detail, the force created by the high-pressure region, which should prevent the jets from returning to the centerline, is overcome by the low-pressure regions which are growing in strength faster. These low-pressure regions are ultimately responsible for pulling the jets back towards, and across, the centerline.

5.3   Influence of pressure on mechanism

As a result of the pressure fluctuations in the flow field being of the same order of magnitude as the stagnation pressure of the jets, the pressure field will undoubtedly play a role in the underlying phenomenon. Particular focus will now be given to the high-pressure region in the center of the flow field, as well as the low-pressure regions in the circulation zones which form on either side of each jet column. The high-pressure region has been a topic of discussion in previous investigations, including those by Li *et al.* (2011, 2013), Tu *et al.* (2014a) and Hassaballa and Ziada (2015). It is widely agreed upon that this high-pressure region which forms as the jets impinge on one another will play a role in driving the jet columns away from the centerline. However, there is still considerable debate surrounding the process which brings the jets back towards the centerline. Li *et al.* (2013) proposed a 'pressurizing and depressurizing' process of the impingement region, while Hassaballa and Ziada (2015) showed leading indicators of the cross-stream fluctuating velocity on either side of the jet columns. Although both propositions have their merits, the details of the mechanism which drives the jet columns back and forth remains unknown.

Figure 5.11 a) shows the deflection angle of the jet columns, as well as the pressure in the impingement region, over the oscillation cycle. A positive value of the deflection angle represents an upward deflection of the left jet and a downward deflection of the right jet. The pressure in the impingement region reaches a maximum as the jets approaches the centerline, near a time (t) of 0.1τ and 0.6τ. The pressure in this region also shows a minimum near the time in the oscillation cycle as the jets reach their maximum deflection, at approximately 0.25τ and 0.75τ. Figure 5.11 b) shows the same data, but with the deflection angle plotted along the independent axis and the pressure in the impingement region along the dependent axis. The maximum is more clearly observed near the point when the jets pass the centerline,
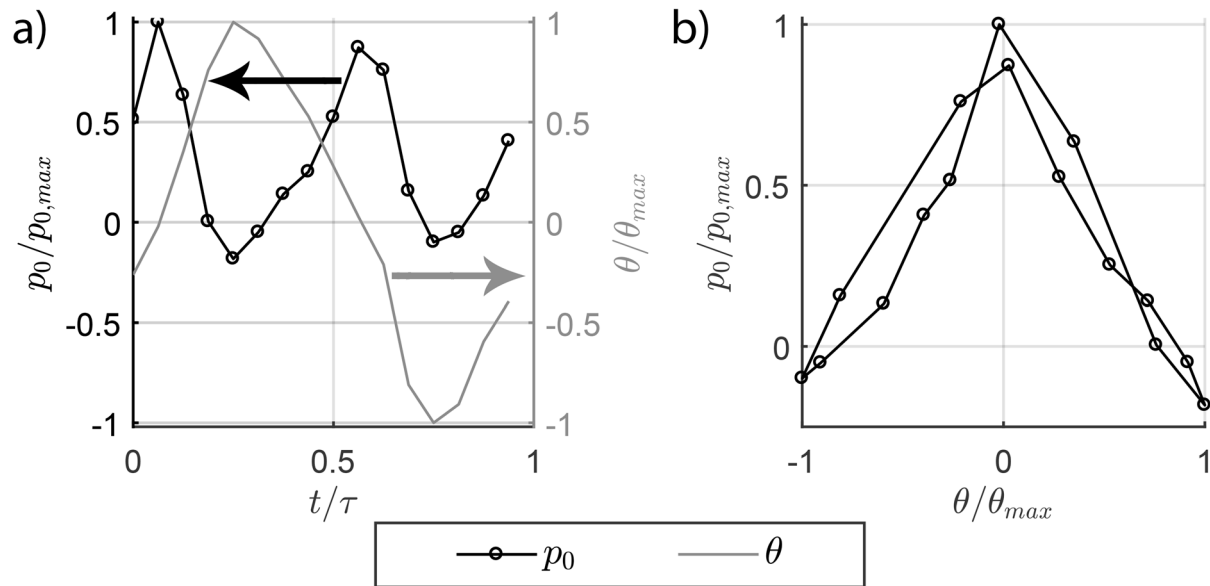
Figure 5.11: Pressure in impingement region over oscillation cycle

while the minimums are located at the maximum deflection angles. Furthermore, the rate at which the pressure increases as the jets approach the centerline is similar to the rate at which it decreases as the jets deflect away from the centerline. Even though the pressure in the impingement region grows rapidly as the jets approach the centerline, the jets continue to return to the centerline in an organized manner. The similarity in the pressure profile in the impingement region as the jets deflect and return to the centerline suggests that this region is neither extracting nor injecting much energy into the oscillations over the oscillation cycle. If this high-pressure region played a significant role in driving the oscillations back and forth, one would expect the pressure in the impingement region to be larger during the deflection process. Therefore, while this high-pressure region will unequivocally play a role in driving the jet columns away from the centerline, it does not appear that these regions are entirely responsible for sustaining the oscillations.

Since the high-pressure region in the center of the flow field does not appear to be

responsible for driving the jet columns back and forth on its own, similar analysis will now be extended to the low-pressure regions which form periodically in the circulation zones on either side of each jet column. In particular, the pressure differential across each jet which results from the existence of these zones will be investigated. To gain a more complete understanding of the influence of the pressure differential across each jet over the oscillation cycle, the pressure difference is calculated at each phase in the oscillation cycle, at three downstream distances ($l = 0.1L$, $0.2L$ and $0.3L$) of each jet. At each of these downstream distances, the pressure differential is calculated by taking the difference in the pressure above and below the jet, measured at the cross-stream locations where the flow velocity is half the maximum local value. These cross-stream locations are determined by measuring the maximum velocity at each cross-section of the jet and finding the cross-stream location where the velocity falls to half the maximum value. This calculation is repeated for each phase-resolved pressure field, such that a true representation of the pressure difference acting on the jets over the oscillation cycle is determined. Figure 5.12 illustrates the points where the measurements are taken for four phases in the oscillation cycle, with accompanying velocity vectors to indicate the flow field at each phase. The solid black lines indicate the maximum velocity line of each jet, while the grey lines indicate the half velocity lines. The pressure differential is calculated for each pair of points at the three downstream locations of each jet. For both jets, p_1 is the pressure at the half velocity point above the jet, while p_2 is the pressure at the half velocity point below the jet. Therefore, a positive pressure differential ($p_2 - p_1$) indicates a pressure gradient that would apply an upward force on each jet. The pressure difference observed by the left jet at each of the three downstream distances, as well as the deflection angle (θ), are shown in Figure 5.13. Again, a positive deflection angle indicates an upward deflection of the jet. Subset a) shows the leading indicators of the
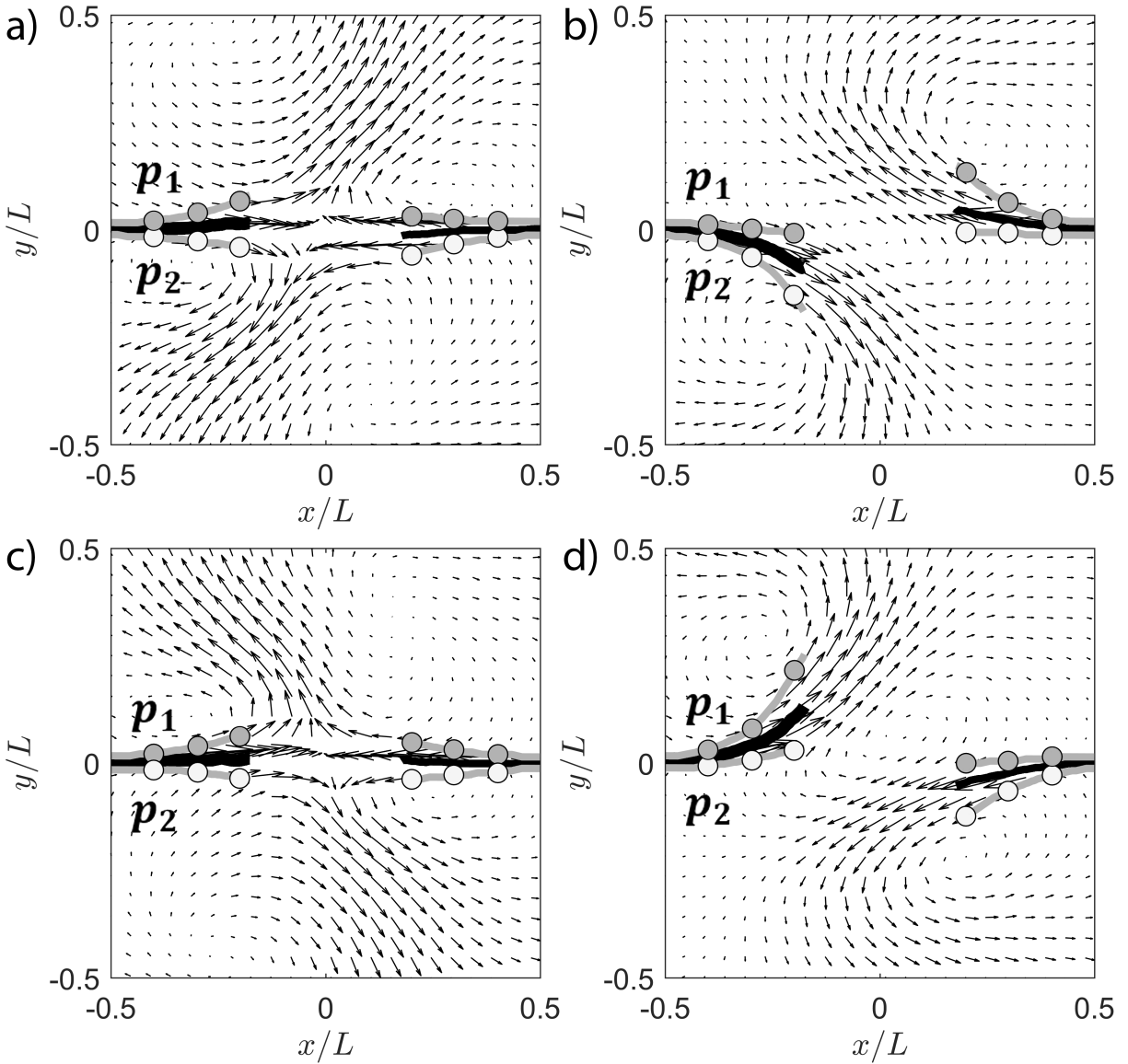
Figure 5.12: Phase-resolved velocity field at a) 0°, b) 90°, c) 180° and d) 270°, indicating where pressure measurements are taken along half velocity lines
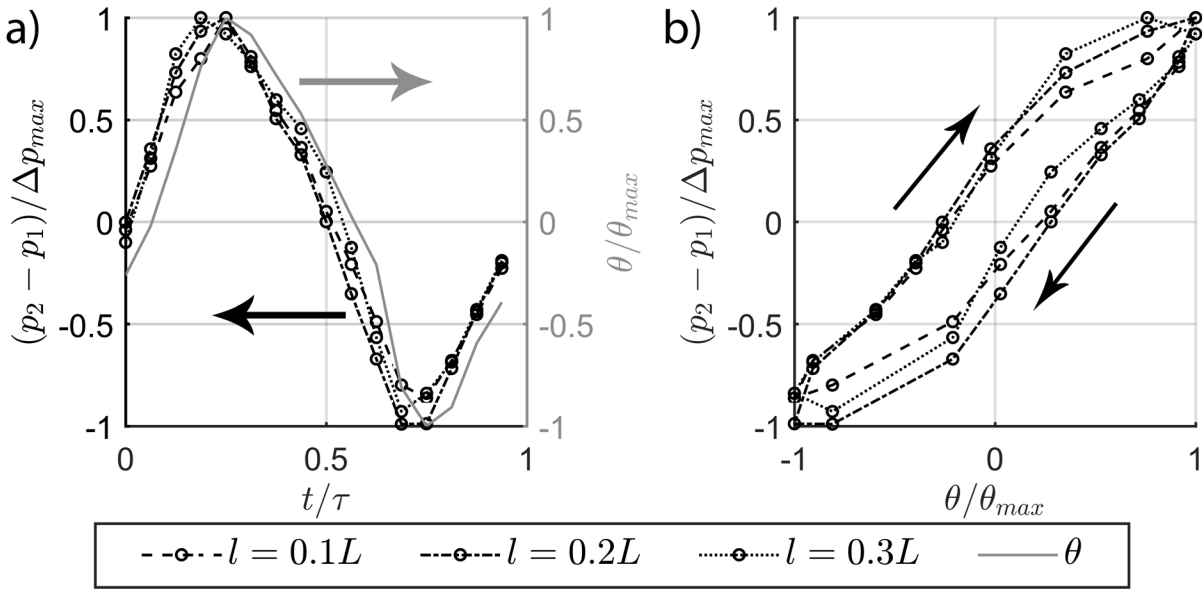
Figure 5.13: Pressure differential across left jet column at varying downstream distances over the oscillation cycle

pressure difference as the pressure signal leads the jet deflection angle at all three downstream locations. While this is true for all downstream locations measured, the pressure leads the jet deflection more for further downstream distances. As the same data is plotted in subset b), with the deflection angle along the independent axis and the pressure difference along the dependent axis, the variation in the pressure differential during the jet's deflection away and back towards the centerline is more clearly observed. For example, as the jet is moving upwards and approaches the centerline ($\theta = 0°$), the pressure is already positive, effectively pushing the jet past the centerline. Similarly, as the jet moves downwards, the pressure is already negative prior to the jet reaching the centerline. The same analysis is conducted on the right jet in Figure 5.14, with a positive deflection angle again representing an upward deflection, and the same trends are observed. The area between the pressure profiles during the deflection and return processes is indicative of the energy which is injected into the oscillations by the circulation zones as they pull the jets back and forth. Interestingly, both
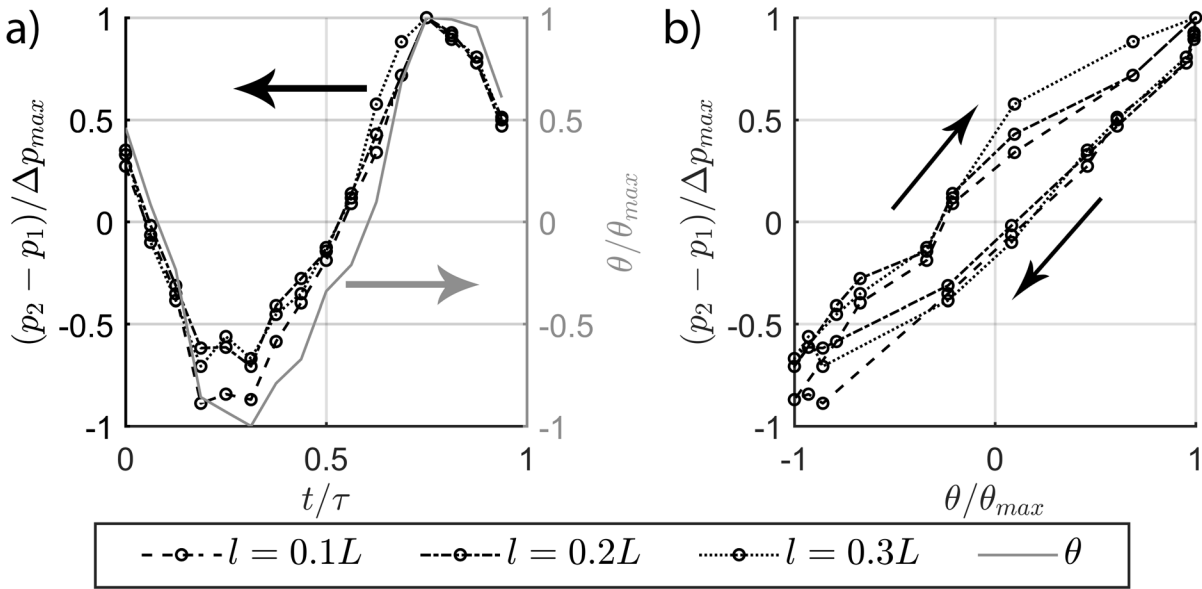
Figure 5.14: Pressure differential across right jet column at varying downstream distances over the oscillation cycle

the deflection angle and amplitude of the pressure fluctuations in the low-pressure regions of the right jet are approximately 15% lower than those observed in the left jet. This is a result of the microphone used to phase-lock the measurements being situated in the upper left corner of the flow field. Therefore, the microphone is phase-locked with the deflections of the left jet as this signal is dominated by the sound radiated by the pressure fluctuations in the upper left low-pressure region. While both jets appear to deflect exactly 180° out of phase with one another, there is small amounts of jitter in the relative phase of the jet deflections. This is apparent when observing a set of 200 instantaneous PIV measurements taken at the same phase in the oscillation cycle. The left jet is observed to be located at almost precisely the same deflection angle in each instantaneous image, while the deflection angle of the right jet varies slightly ($\pm 7\%$). Thus, the velocity gradients of the phase-resolved velocity field are slightly stronger around the left jet than the right jet and therefore the pressure amplitudes are as well. Therefore, the pressure amplitudes in the left half of the

flow field are likely more indicative of those radiated, however the right side of the pressure field provides more insight into the range of amplitudes which will be produced over various oscillation cycles. Nonetheless, while the variation in the amplitude between the two halves of the flow field is important to note, the difference is relatively small as a result of the strongly coherent global oscillations of the opposing planar jets.

Both the high-pressure region in the center of the flow field and the low-pressure regions in the circulation zones are synchronized with the oscillations and play key roles in sustaining the oscillations. During the deflection process of the jets, the high-pressure region clearly contributes to driving the jet columns away from the centerline. However, the low-pressure regions in the circulation zones also appear to pull the jets away from the centerline during the deflection process. This is most apparent in the pressure field measurements shown in Figure 5.10, as the strength of the low-pressure regions is largest as the jets reach their maximum deflection at approximately 90°, as well as the magnitude of the pressure differential is largest at the maximum deflection in Figure 5.13. Furthermore, these low-pressure regions prevent the jets from suddenly and chaotically returning to the centerline as the high-pressure region dissipates at the maximum deflection as a result of the time required for the circulation zones to dissipate and convect away. However, during the return of the jet columns to the centerline, the high-pressure region in the center of the flow field appears to be growing quickly and creating a force which will prevent the jets from returning to the centerline. During this process, the circulation zones formed ahead of the jets' motion are also growing in strength. Interestingly, the pressure gradients across the jets indicate that these regions are growing faster than the high-pressure region. The result is low-pressure regions which overcome the high-pressure region and pull the jets back towards, and ultimately across, the centerline.

5.4   Impact of jet aspect ratio on fluid dynamics

Table 5.1: List of PIV investigations conducted on opposing planar jets

Investigation	h (mm)	L (mm)	V (m/s)	St_L
	2	80	45	.12
Effect of Velocity	2	80	90	.11
	2	80	135	.11
	2	40	90	.14
Effect of Impingement Distance	2	80	90	.11
	2	120	90	.10
	2	160	90	.09
	1	80	90	.08
Effect of slot width	2	80	90	.11
	3	80	90	.13
	4	80	90	.16
	2	40	45	.13
Scaled with constant slot width	2	80	90	.11
	2	120	135	.10
	2	160	180	.09
	1	40	45	.09
Scaled	2	80	90	.11
	3	120	135	.13
	4	160	180	.13

The flow field of the opposing planar jets is investigated using PIV for a variety of flow parameters, as outlined in Table 5.1. Each set of the test cases is conducted to investigate the impact of varying each parameter relative to the base case of $L = 80$ mm, $V = 90$ m/s and $h = 2$ mm. In particular, the impingement distance is varied, then the exit velocity of the jets, then the slot widths, followed by a variation in the impingement distance and jet exit velocity together and finally, all three parameters varied together. The experiments are conducted in this manner to help resolve possible explanations for the variation in the Strouhal number of the oscillations observed in Section 5.1. Interestingly, the flow dynamics observed in the phase-resolved measurements show remarkable similarity between the cases,

as the same asymmetric flapping of the jet columns, driven by the development, growth and dissipation of the circulation zones, is observed. However, careful analysis shows two key variations in the velocity and pressure fields. These are the amount of momentum transferred to the cross-stream directions as a result of variation in the deflection amplitude and spread of the jet columns, as well as the location of the circulation zones relative to the jet columns (Y_r). The variation of the jet's momentum transfer to the cross-stream direction is indicated by the spread of the jets (b) in the *time averaged mean velocity profile*. The width of the jet spread is determined by averaging 300 images recorded at random phases throughout the oscillation cycle and measuring the cross-stream locations of the half velocity points at a downstream distance of $0.25L$ of each jet. Figure 5.15 shows an example of how the spread is calculated from the steady mean velocity field. This figure also shows how the location of the circulation zones is measured by determining the distance of the center of the circulation zones relative to the centerline of the mean velocity field, which reveals an averaged representation of the circulation flow. Both the width of the jet spread and the location of the circulation zones are measured in each quadrant of the flow and an averaged value of each test case is presented.

The variation in the cross-stream location of the circulation zones is shown in Figure 5.16. While significant variation in the location of the circulation zones relative to the centerline is observed for both changes in the impingement ratio and jet aspect ratio, the jet exit velocity is shown to have little impact. Increasing the impingement ratio for a given aspect ratio is shown to cause the circulation zones to be located closer to the jets' common centerline. This is a result of the impingement ratio effecting the jet deflection angle required to depressurize the high-pressure region formed at impingement. For example, for smaller impingement ratios, the jets do not travel as far downstream before impinging on one another, causing
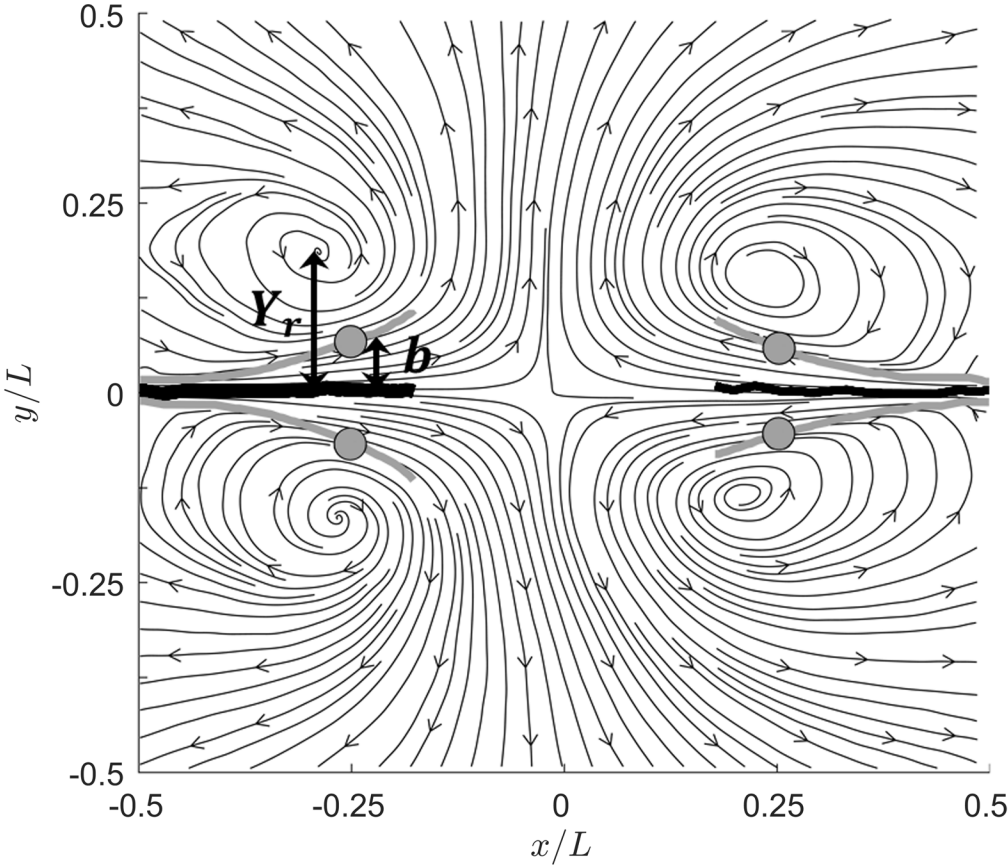
Figure 5.15: Steady mean flow field indicating how the spread (b) and cross-stream location of the circulation zones (Y_r) are measured
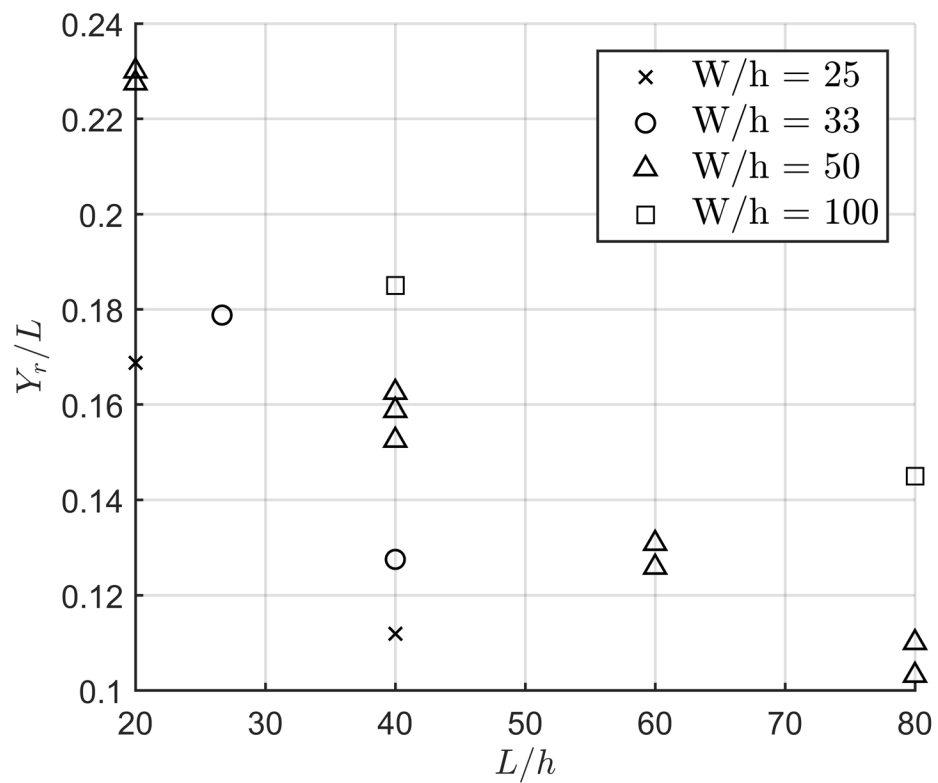
Figure 5.16: Location of circulation zones (Y_r) relative to the jets' centerline for varying impingement ratio $(\frac{L}{h})$ and jet aspect ratio $(\frac{W}{h})$

them to exhibit larger deflection angles in order to eliminate the high-pressure region in the center of the flow field. However, a more obscure trend is observed as the circulation zones appear to move further away from the centerline as the aspect ratio of the jets increases. Even as the impingement length, jet exit velocity and slot width are varied together, a consistent increase in the circulation zones' cross-stream location is observed with increasing aspect ratio. For example, for the perfectly scaled cases between $h = 1 \ mm$, $L = 40 \ mm$ and $V = 45 \ m/s$ to the case of $h = 4 \ mm$, $L = 160 \ mm$ and $V = 180 \ m/s$, one would expect the location of the circulation zones relative to the impingement length to remain constant. However, it is observed that for the $h = 1 \ mm$ case, the cross-stream distance of the circulation zones relative to the centerline is $0.19L$, while for the $h = 4 \ mm$ case, the distance decreases to approximately $0.11L$. The variation in the circulation zones will have a large impact on the jet oscillations as the circulation zones are aligned with the location of the low-pressure regions which have been shown to play an essential role in sustaining the oscillations. Specifically, the closer the low-pressure regions are to the jet columns, the stronger the force driving the jet columns back and forth will be. This influence of the location of the circulation zones on the jet oscillations is indicated by the variation in the spread of the jets shown in Figure 5.17. As expected, for a given jet aspect ratio, the spread of the jet appears to increase with the impingement ratio as a result of the spread being measured further downstream of the jet exit. However, as the aspect ratio increases, so does the spread of the jets relative to the slot width. Therefore, even as the slot width, impingement distance and jet exit velocity are all varied together, a larger percentage of the jets' momentum is transferred to the cross-stream direction as the aspect ratio is increased.

While it does appear the variation in the jet aspect ratio does have a subtle impact on the observed flow dynamics associated with the opposing planar jet oscillations, it is not
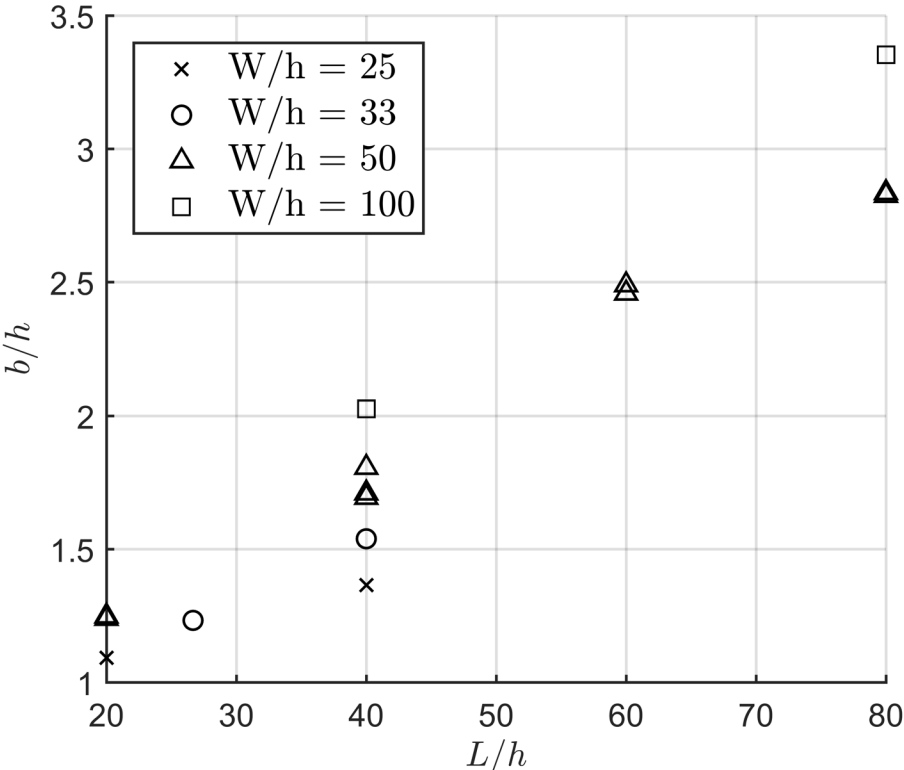
Figure 5.17: Spread of jet relative to jet slot width for varying impingement ratio and jet aspect ratio
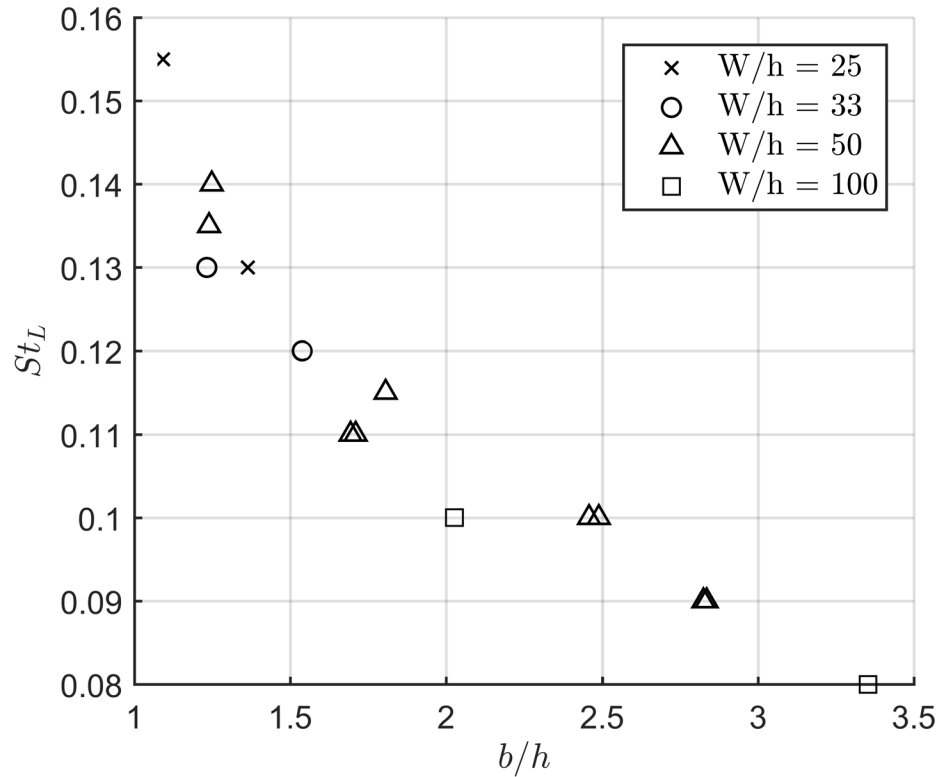
Figure 5.18: Strouhal number of oscillations for varying jet spread and jet aspect ratio

clear how these variations relate the observed trends in the Strouhal number. Figure 5.18 reveals the variation of the Strouhal number of the oscillations with the observed spread relative to the slot width of the jets. Despite the variation in the location of the circulation zones, the Strouhal number is observed to fairly consistently decrease with increasing spread. Therefore, as the impingement ratio increases, the circulation zones move closer to the jet columns and have more of an influence in driving the jet oscillations and consequently, more momentum is transferred to the cross-stream direction. The result is the jets deflect further, causing the period of the oscillations to increase, and the resulting Strouhal number to decrease. However, this still does not explain why increasing the aspect ratio for a perfectly scaled experiment results in an increase in the spread, and more importantly a

decrease in the Strouhal number. Increasing the aspect ratio of the jets causes an increase in the cross-stream location of the circulation zones, as a result of the increased size of the circulation zones relative to the flow field. The increased size of the circulation zones results in more time being required for them to grow and dissipate each oscillation cycle, and thus an extended oscillation period. While there does appear to be a strong link between the flow field characteristics and the resulting Strouhal number, further research is necessary to determine the root cause of these variations in the flow field characteristics. Appendix C provides a number of possible explanations for these observed trends and suggests that it may be a phenomenon which exists in the two-dimensional flow field and is a result of the variation in the relative energy transferred to the circulation zones as the aspect ratio varies.

5.5   Sound-source characterization

One additional unique feature of the current pressure field mapping technique is the ability to determine the fluctuating pressure field associated with the self-sustained oscillation by subtracting the time-averaged pressure field from phase-resolved pressure field presented in Section 5.2.2. These pressure fluctuations are ultimately the source of the sound radiated from the flow field which is recorded by the microphone. A detailed depiction of the fluctuating pressure field ultimately allows for a better understanding of the radiated sound field and can even be used to develop effective sound suppression strategies. Figure 5.19 reveals the phase-resolved fluctuating pressure field for eight phases in the oscillation cycle. As expected, the high-pressure region in the center of the flow field appears to fluctuate twice over the oscillation cycle, with the maximum aligned with the phases in the oscillation cycle as the jets impinge upon one another. The circulation zones on either side of both jets are also synchronized with pressure fluctuations in these regions and occur once per oscillation
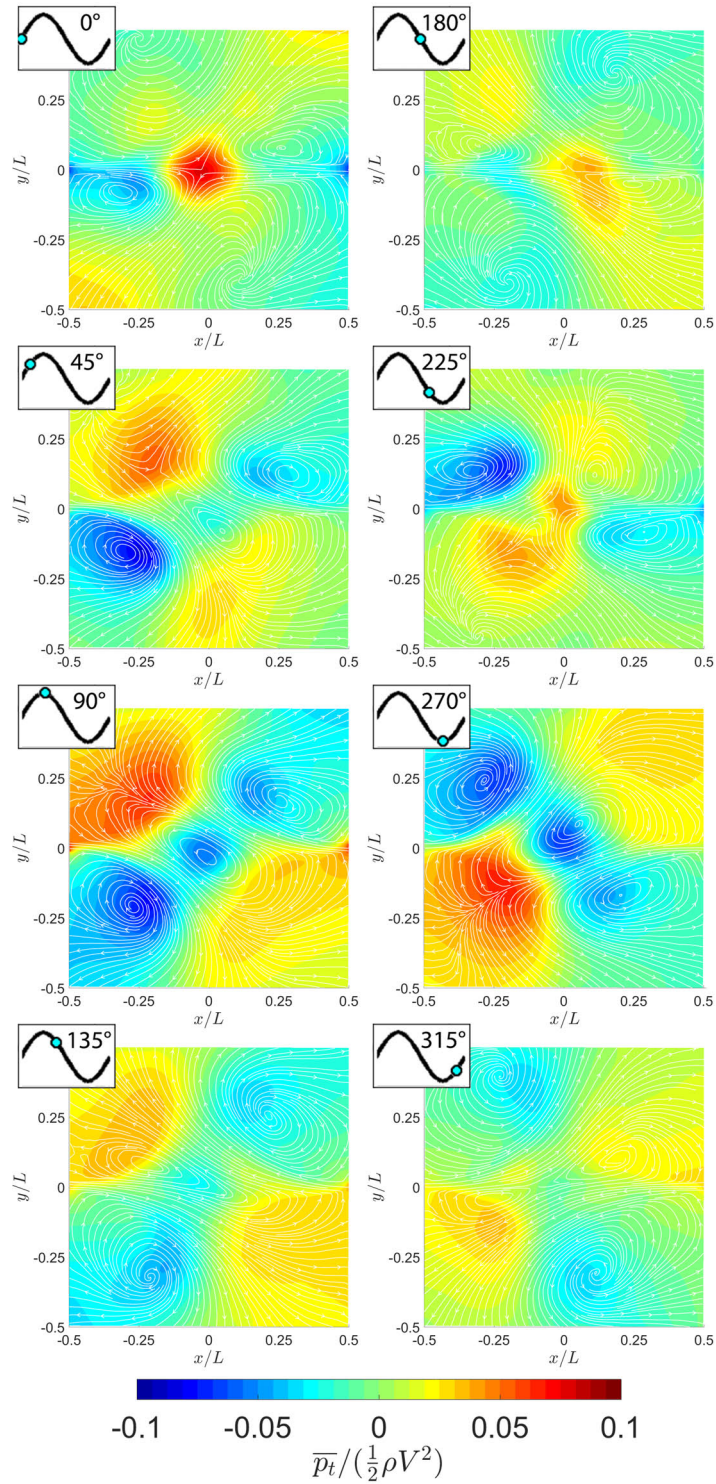
Figure 5.19: Phase-resolved fluctuating pressure field with accompanying streamlines of opposing jets at eight phases in the oscillation cycle

cycle. However, for each jet, as a negative pressure fluctuation is observed on one side of the jet, the opposite side reveals a positive pressure fluctuation. As a result of the asymmetric nature of the pressure field, the sound field associated with the fundamental appears to take the form of a quadrupole.

Similar to the analysis in Section 4.5, the pressure signal extracted from the PIV data at each spatial location in the phase-resolved fluctuating pressure field ($\overline{p_t}$) will be of the form,

$$\overline{p_t} = \sum_{1}^{N} A_i \sin(2\pi i f_n t - \phi_i) \tag{5.4}$$

Where f_n is the fundamental frequency the PIV system is phase-locked to and A_i and ϕ_i are the amplitude and phase components associated with the ith frequency component. This holds true as a result of the phase-resolving nature of the measurement technique which causes only the fundamental frequency being phase-locked to and its associated harmonics to be conserved, while all other time scales will be 'averaged out'. Therefore, Equation 5.4 can be fit to the fluctuating pressure field to find the individual phase and amplitude components for the fundamental and each of the harmonics. The fluctuating pressure field is dominated by the fundamental and first harmonic, as the amplitude of the other higher harmonics are an order of magnitude less than these components. Figure 5.20 reveals the amplitude in subset a) with the phase in subset b) for the fundamental frequency component over the flow field. The fundamental appears to be strongest in each of the four circulation regions as high amplitudes are observed in each quadrant. Moreover, the phase data reveals the upper left and lower right quadrants are in phase with one another, however they are 180° out of phase with the lower left and upper right quadrants. Therefore, as a result of the asymmetric flapping nature of the jet columns, the fundamental tone is produced by a quadrupole source field where the impingement plane ($x = 0 \ mm$) and the jets common centerline ($y = 0 \ mm$)
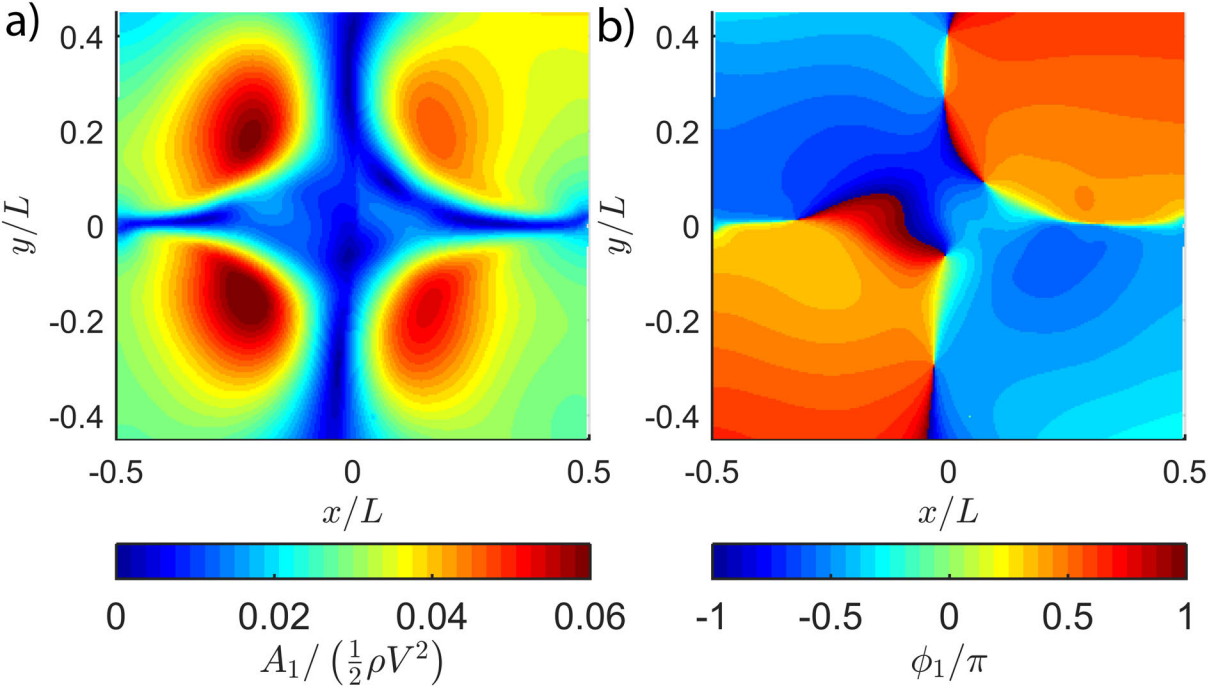
Figure 5.20: a) Amplitude and b) phase associated with fundamental frequency component of fluctuating pressure
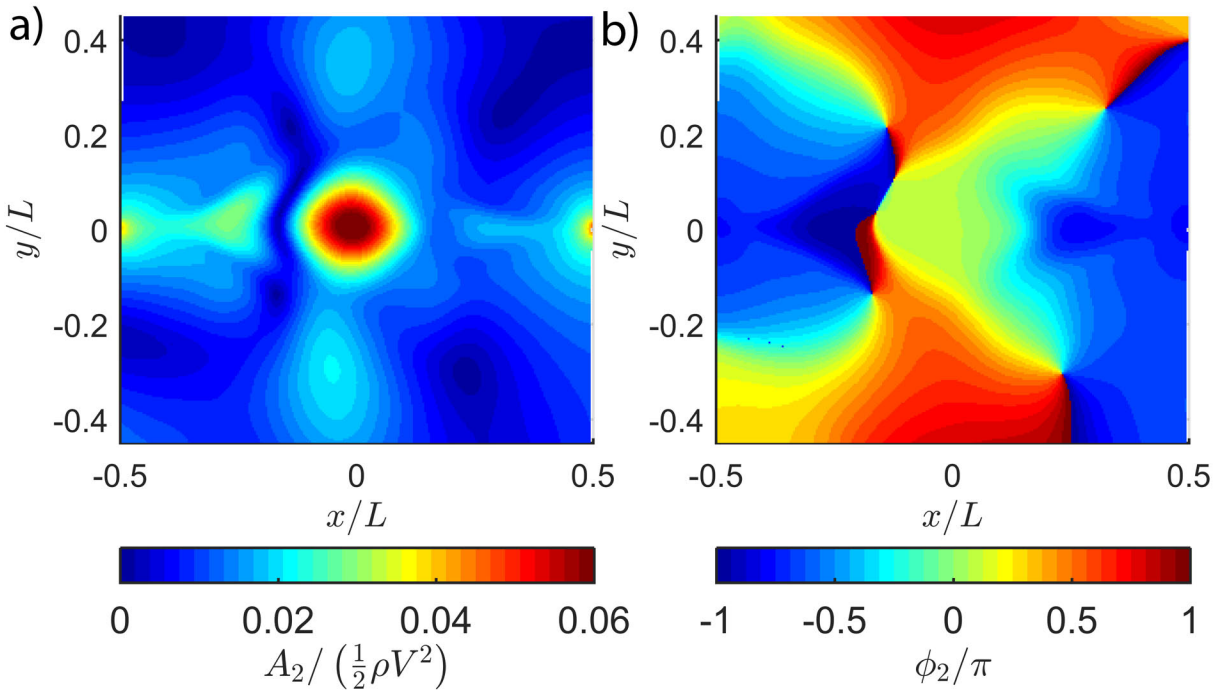
Figure 5.21: a) Amplitude and b) phase associated with first harmonic component of fluctuating pressure

are nodal planes. Figure 5.21 reveals the amplitude and phase data for the first harmonic, as subset a) indicates this frequency has one large amplitude region in the center of the flow field. The phase data in subset b) shows this region is described by a single phase. As such, the pressurizing of the impingement region each half cycle as the jets impinge upon one another creates a first harmonic which is radiated from a monopole source field located in the center of the flow field. While Section 5.1.1 showed microphone measurements which are dominated by the fundamental tone, previous investigations, including that of Hassaballa and Ziada (2015), shows slightly larger harmonic components, relative to the fundamental. However, the measurements are taken along the impingement plane ($x = 0\ mm$), which is the region where the fundamental frequency is much weaker. Therefore, it is not surprising that the first harmonic is observed to be more pronounced, as a result of the weaker fundamental.

5.6   Conclusion

Phase-resolved PIV velocity and pressure measurements are performed on the opposing planar jets. Two important regions of the flow field are revealed; the impingement plane which generates a high-pressure region as the jets impinge upon one another and the circulation zones which create low-pressure regions as the jets deflect. The high-pressure region, in conjunction with the pressure difference across the jets formed by the circulation zones, drives the jets away from the centerline. However, the low-pressure regions are shown to pull the jets back towards, and ultimately across, the centerline. Careful analysis of the pressure fields over the oscillation cycle show that the development of the low-pressure regions leads the jet deflection, resulting in most of the energy being injected into the oscillations in these regions. The acoustic response characteristics for the opposing planar jets is also investigated for a wide range of flow parameters. The Strouhal number based on the jet exit velocity (V), as well as the effective impingement length, measured as the distance between the end of the two jet cores (L_e), is shown to be relatively constant for a given aspect ratio jet. However, increasing the aspect ratio of the jet is shown to consistently reduce the Strouhal number of the oscillations, even as the aspect ratio of the jets gets very large. A number of features are observed in the flow field which correlate with the Strouhal variation, including a larger increase in momentum transfer to the cross-stream direction and formation of circulation zones in regions further away from the centerline as the aspect ratio of the jets increases. While clear trends are observed between the flow field characteristics and the Strouhal number, it is not clear what the root cause of this variation in the flow field is, and further investigations should be performed to help shed light on this interesting trend. Finally, the low-pressure regions which form asymmetrically in each quadrant of the flow are shown to be responsible for creating a quadrupole shaped sound-source field for the fundamental tone.

However, the high-pressure region formed in the impingement plane is shown to generate a monopole shaped sound-source field for the first harmonic. With this understanding of the underlying mechanism, unique mitigation strategies of the opposing planar jet oscillations will now be proposed and investigated.

Chapter 6

Mitigation strategies

The previous chapter discusses a number of unique features associated with the opposing planar jet oscillator with particular focus on their contribution to the self-sustaining mechanism. The importance of the circulation zones is demonstrated as they are responsible for driving the jet columns back and forth. The current chapter will explore potential mitigation strategies of the opposing planar jet oscillator by attempting to disrupt these regions, while only minimally intruding on the remaining regions of the flow field. Specifically, thin splitter plates with varying lengths will be located throughout the flow field to disrupt the flow in this region. It will be shown that even small splitter plates strategically located in the circulation regions are very effective at disrupting the oscillations. The effectiveness of the plates is exacerbated as the circulation flow which passes around the back of the plates is eliminated. Flow visualization is provided to support the findings and offer explanations as to the impact of the splitter plates on the underlying mechanism.
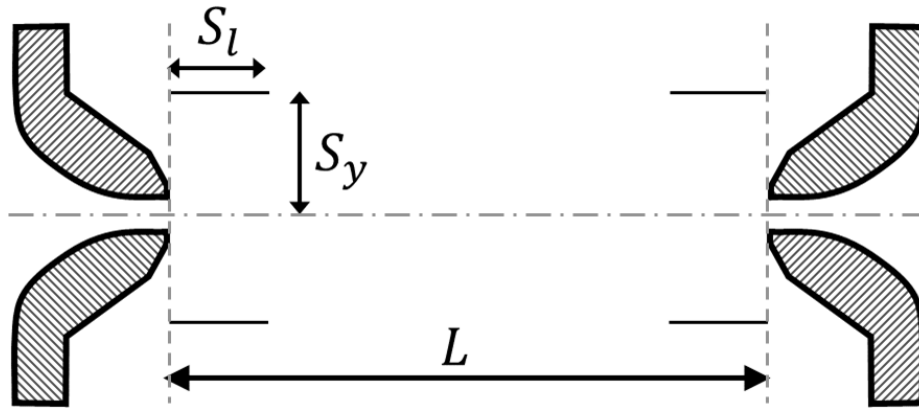
Figure 6.1: Schematic of splitter plate length experiment with opposing planar jets

6.1 Splitter plate methodology

In order to effectively disrupt the oscillations, splitter plates will be introduced to the cir-

culation regions on either side of both jets, far from the impingement region. While long

splitter plates, as well as splitter plates located close to the jet columns, will be investigated,

these are only to demonstrate the trends and effects in the extreme cases. The purpose

of the splitter plate investigation is to attempt to disrupt the circulation zones, while only

minimally intruding on the remainder of the flow field. It is important to focus on the direct

influence of the splitter plates on the flow field far from the jet column and the impingement

plane. This is a result of the number of applications of the opposing planar jets which heav-

ily rely on the impinging jet flow in these regions, such as drying applications and gas-jet

wiping. To examine the effectiveness of the splitter plates, the length of the splitter plates

(S_l), as defined in Figure 6.1, will first be investigated. The experiment is conducted for

the base case, which is comprised of a slot width of 2 mm, impingement distance of 80 mm

and a jet exit velocity of 90 m/s. Splitter plates, made from 16-gauge steel sheets, are si-

multaneously position in each quadrant of the flow field. The plates extend the entire span

of the jets, as well as protrude 25 mm beyond each end of the jets, to ensure the flow field

remains two-dimensional. The plates are clamped in the region above and below the jets using a custom holder, which is attached to a traverse to allow for precise variation in the cross-stream location of the plates (S_y).

Similar to the method discussed in Section 3.2.3, the effectiveness of the splitter plates is evaluated by measuring the average noise spectra at the microphone location. For each measurement, four plates of specified length (S_l) are located at the same cross-stream distance from the centerline (S_y), as shown in Figure 6.1. For each case, the upstream edge of the plates will be located along the jet exit planes ($x = \pm\frac{L}{2}$). Furthermore, the plates will be located in each quadrant of the flow, such that all four circulation zones are equally disrupted. Care is taken to ensure all four plates are the same length and located in the same relative position to one another, such that symmetry is maintained about the impingement plane ($x = 0$ mm) and the jets' common centerline ($y = 0$ mm). The cross-stream location of the splitter plates is varied in 1 mm increments from 2 mm to 30 mm, as well as 5 mm increments from 30 mm to 50 mm, while the length of the plates used varied between 9 mm and 39 mm for most of the investigations. The largest splitter plate case of 39 mm represents the case where the plates are almost touching, but a 2 mm space remains to allow the flow to escape the impingement region. For each splitter length studied, the plates are first translated from the largest cross-stream distance to the smallest, then back to the largest, in order to capture the locations where the oscillations are first disrupted and initiated. This is done three times for each case to find an average representation of the acoustic response. However, throughout all the cases, the cross-stream location of onset is almost precisely the same location where the oscillations are eliminated.

6.2 Effect of splitter plate length

In general, the observed impact of the splitter plates on the acoustic response is a reduction in the frequency and amplitude of the oscillations as the plates get longer and/or move closer to the jets' centerline. The influence of varying the cross-stream location of the splitter plates on the acoustic spectra is shown in Figure 6.2 a), for the case with a splitter plate of length $0.25L$. Similar to previous results, the frequency is presented in Strouhal form, while the RMS pressure amplitude (P_{rms}) is non-dimensionalized using the peak RMS pressure amplitude for the case with no splitter plates (P_{max}). While a consistent decrease in the frequency, amplitude and sharpness of the tones are observed as the plates move closer to the jet columns, the most significant variation occurs for cross-stream distances less than $0.44L$. As the oscillation quality diminishes, the raw time signals show both amplitude and frequency modulation, as the oscillations are unable to sustain themselves in a repeatable and robust manner. Later discussion will demonstrate the influence of the splitter plates on the oscillations, as the circulation zones appear to be unable to form and develop in a consistent manner. Figure 6.2 b) shows the influence of varying the splitter lengths for a cross-stream location of $0.25L$, as a similar reduction in the frequency, amplitude and quality of the oscillations is observed with increasing splitter length. The oscillations are drastically impeded as the splitter plates become longer than $0.19L$ and subsequently, are no longer observable as the plates become $0.38L$ long.

The same analysis is extended to a complete range of splitter plate lengths and cross-stream locations. Figure 6.3 reveals the spectral characteristics observed as the length and cross-stream location of the plates are varied, as subset a) shows the frequency of the oscillations relative to the case with no splitter plates (f_{max}) and subset b) shows the relative pressure amplitude once again. For the shortest splitter plate case shown ($S_l = 0.11L$),
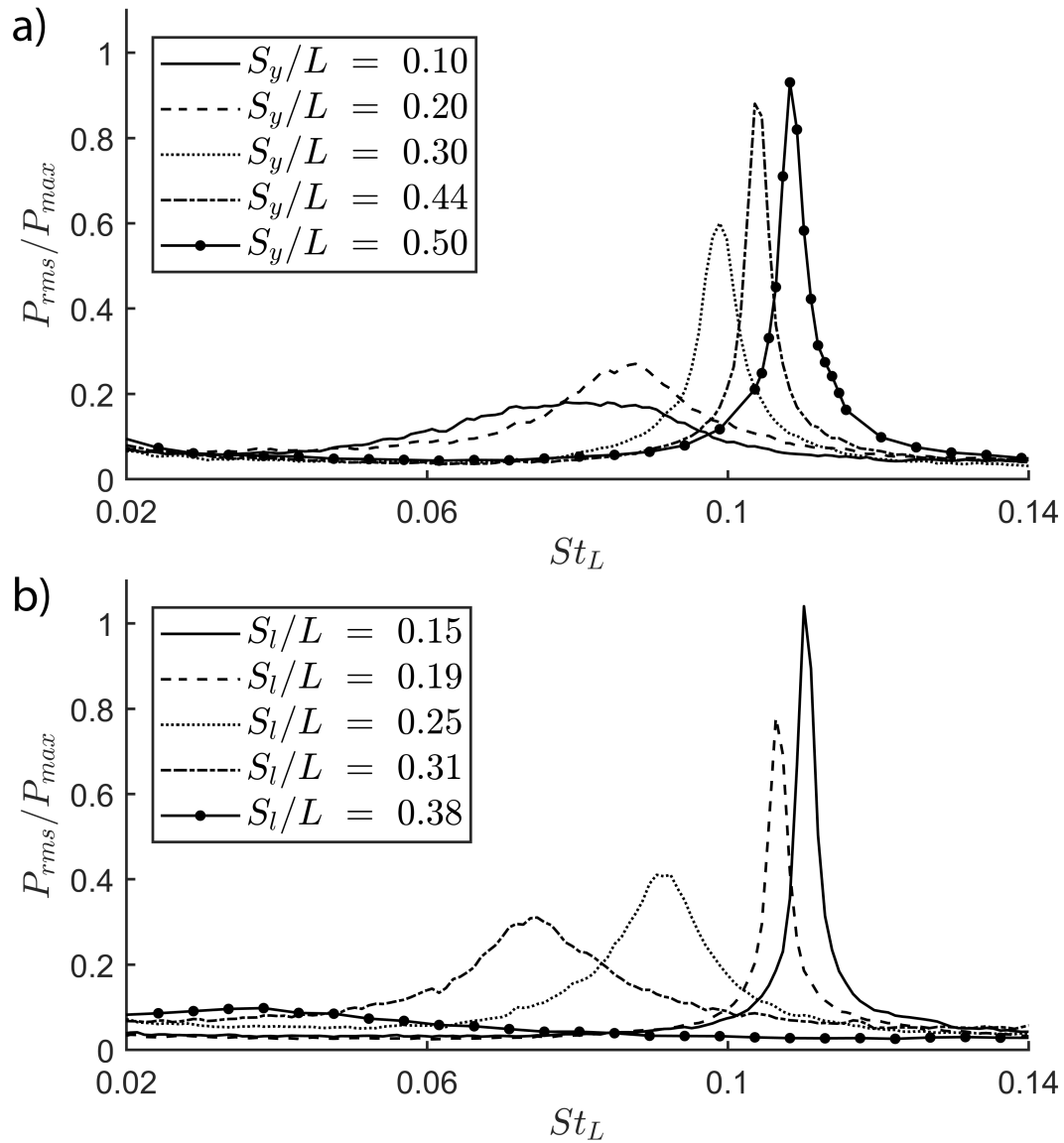
Figure 6.2: Impact of splitter plates on acoustic response spectra for varying a) splitter cross-stream location ($S_l = 0.25L$) and b) splitter length ($S_y = 0.25L$) ($h = 2\ mm$, $L = 80\ mm$, $V = 90\ m/s$)
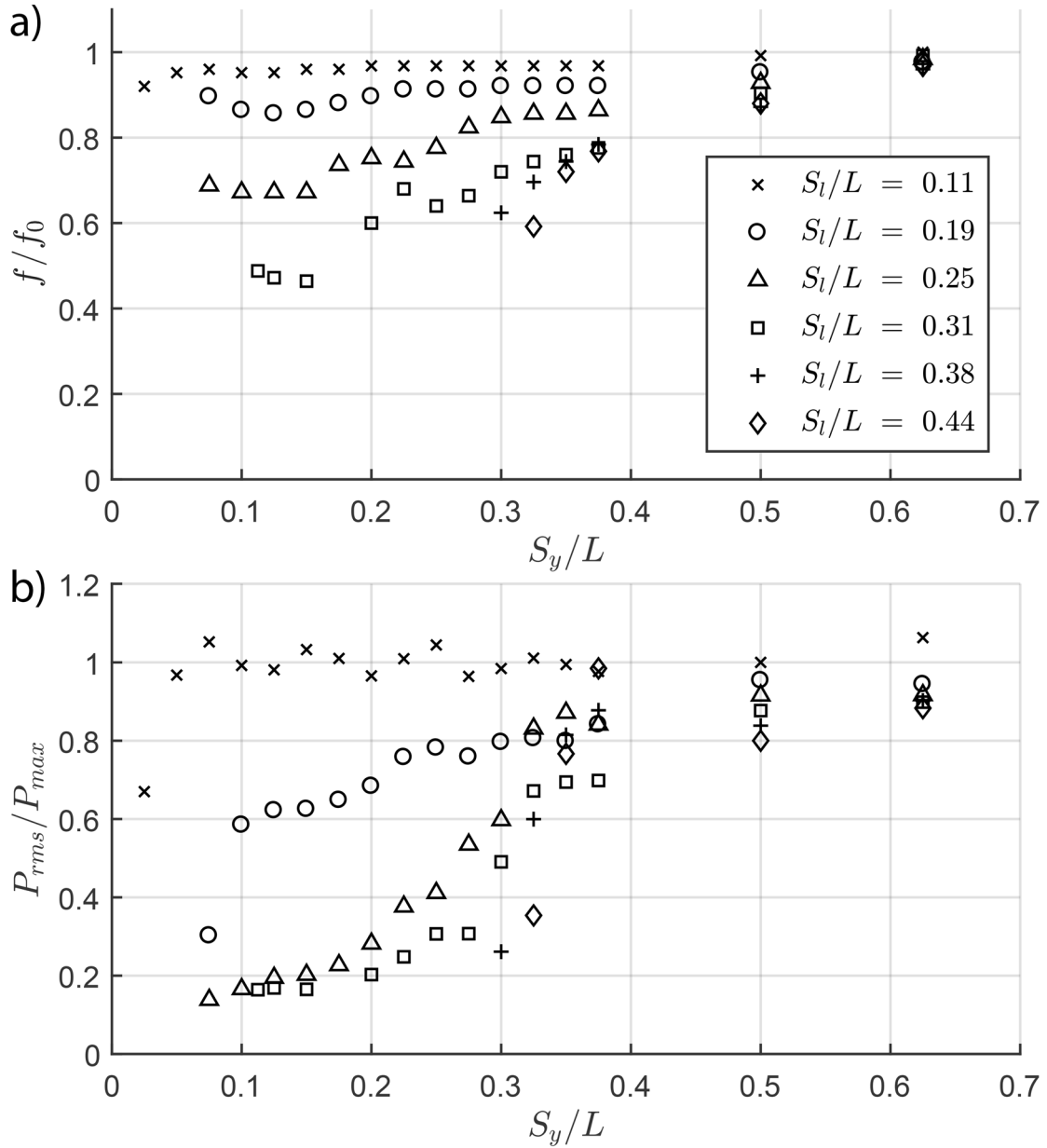
Figure 6.3: Impact of splitter plate length on acoustic response characteristics including a) relative frequency and b) relative amplitude ($h = 2\ mm$, $L = 80\ mm$, $V = 90\ m/s$)
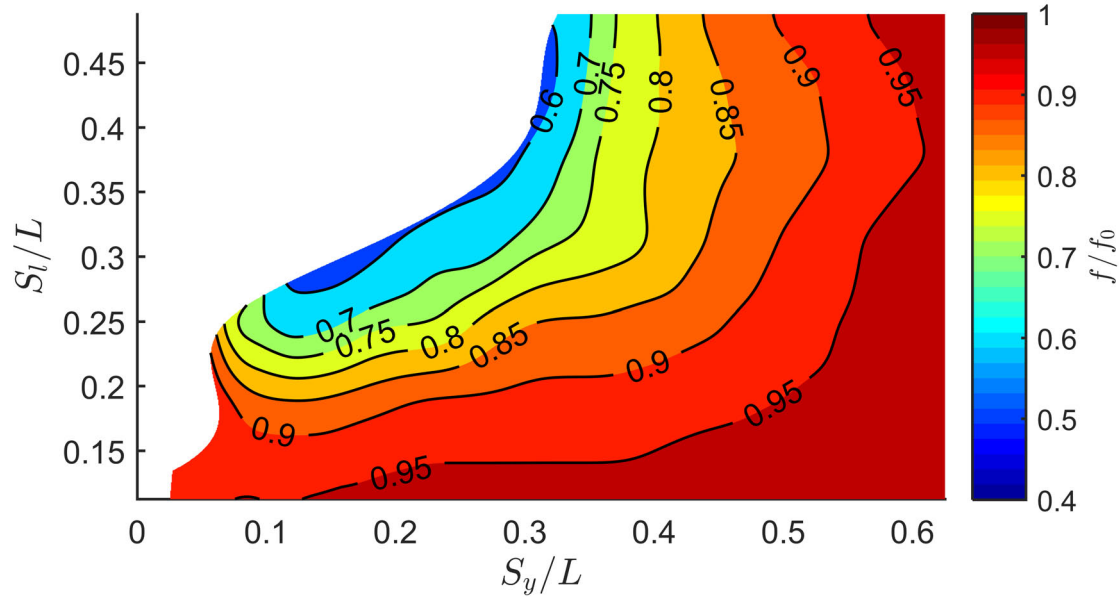
Figure 6.4: Contour plot of impact of splitter plate length on relative frequency ($h = 2\ mm$, $L = 80\ mm$, $V = 90\ m/s$)

there is a very small reduction in the frequency of oscillation ($\approx 4\%$) and negligible amplitude reduction as the plates are moved closer to the jet columns. As the plates are extended to $0.19L$ long, the frequency reduction becomes slightly more sensitive to the cross-stream location and the amplitude is reduced by approximately 40% as the plates move closer to the jets' centerline. Furthermore, the oscillations are no longer observable as the plates are located closer than $0.08L$ from the centerline, which is not surprising, as the plates are impeding directly on the jet columns as they attempt to deflect. The same trend of increasing effectiveness of the splitter plates in reducing the amplitude and frequency for smaller cross-stream distances is observed as the plates continue to get longer. The impact of the splitter plates is most pronounced for all the splitter length cases, as the plates are located closer than $0.4L$ from the jets' centerline. As will be discussed in more depth later, this is precisely the region where the circulation zones are formed.

The same frequency data presented in Figure 6.3 a) can be plotted in contour form for a more meaningful interpretation, as shown in Figure 6.4 The contours reveal two distinct regions with unique variations in the oscillation frequency. The first of which is for smaller cross-stream locations ($S_y < 0.4L$), as the frequency decreases with both an increase in the length of the splitter plates and a decrease in the cross-stream location. The second region occurs for larger cross-stream locations ($S_y > 0.4L$), as the frequency appears to be independent of the splitter length and gradually decreases as the plates get closer to the jet columns. The white region of the figure, which appears for smaller cross-stream locations, represents the region where oscillations are not observed. It is not surprising that the oscillations are disrupted as the splitter plates impede on this region, as this is precisely in the desired path of the jet columns as they deflect. As a result of the splitter plates preventing the jets from deflecting, the oscillations are not self-sustained.

Finally, the frequency reduction data can be plotted on top of the phase-resolved velocity field, for the case with no splitter plates, to better illustrate the influence of the splitter plates. Figure 6.5 shows the frequency reduction contours overlaid with the phase-resolved velocity streamlines at a sample phase in the oscillation cycle. The grey region indicates the regions where the oscillations are not observed, while the black region represents points outside the range of test cases investigated as the shortest splitter plates used are 9 mm long. To illustrate the meaning of the frequency reduction contours, the splitter plates are also plotted (light blue lines) for an example case of $S_l = 0.2L$ and $S_y = 0.3L$, which reduces the frequency to 90% of its initial value. The same can be done for any point along the contour lines, as the plates will always extend from the jet exit plane to the contour line. Figure 6.6 shows four phases in the oscillation cycle over a half cycle, with the phase-resolved velocity streamlines and frequency reduction contour lines. The center of the two circulation zones
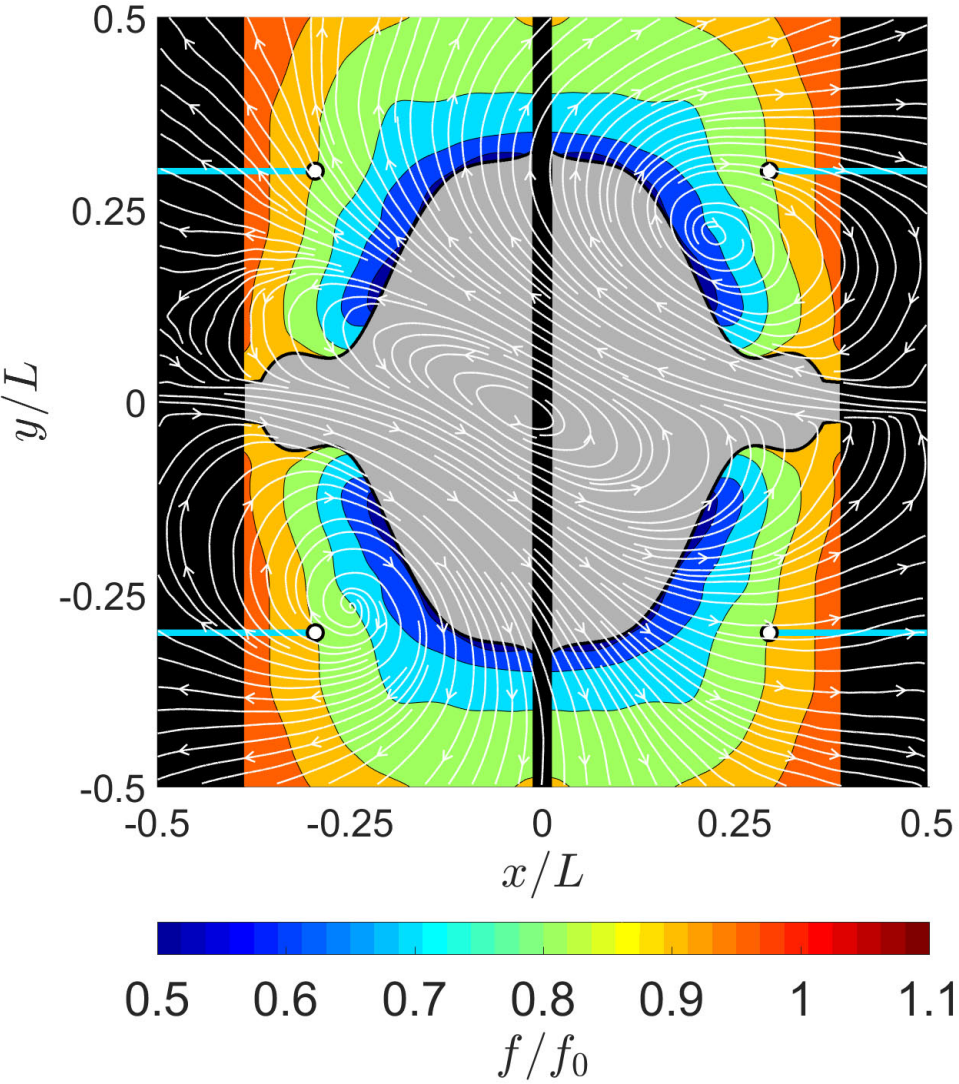
Figure 6.5: Phase-resolved velocity streamlines with example splitter plate length experiment at $S_y = 0.3L$ and $S_l = 0.2L$
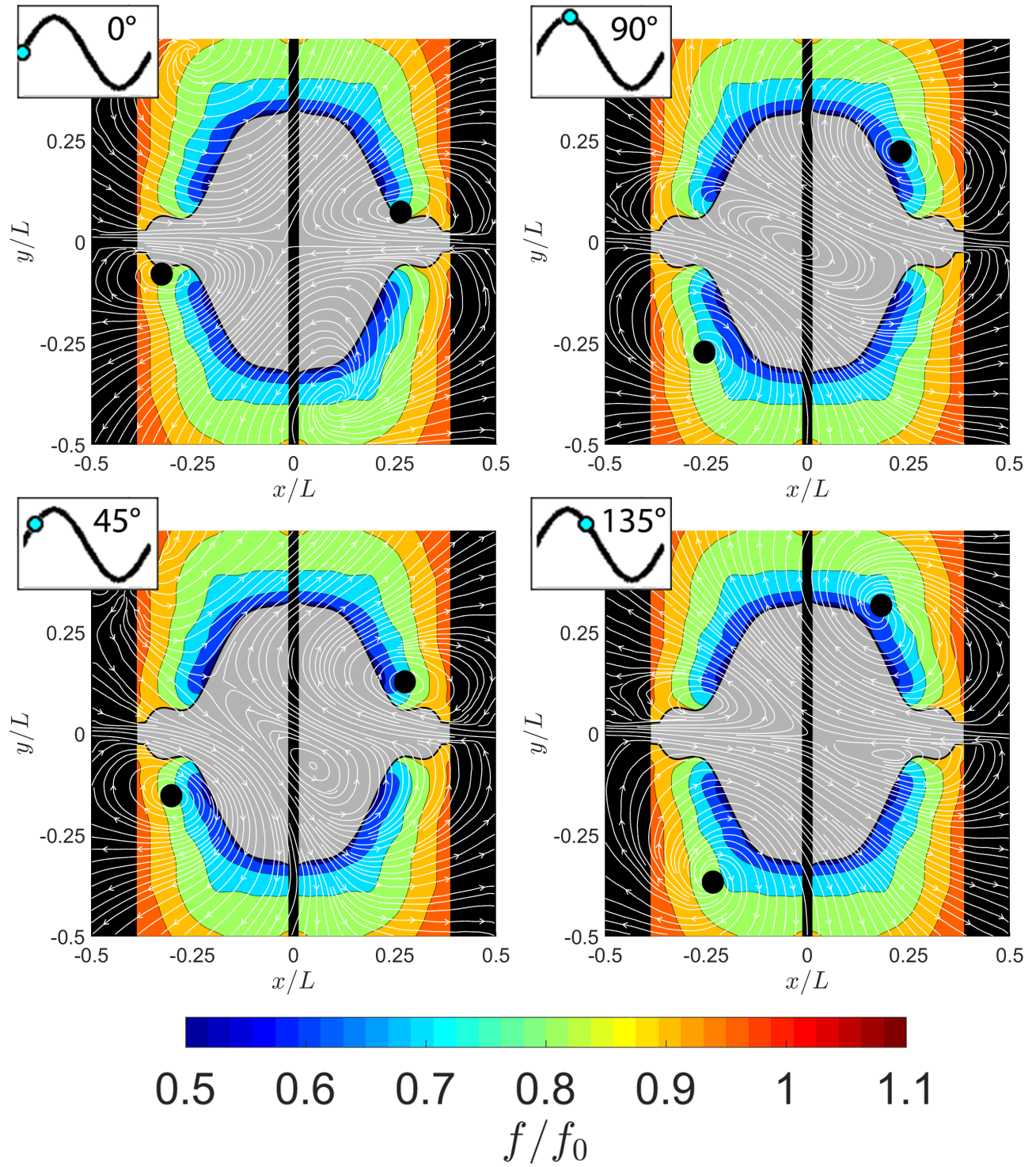
Figure 6.6: Phase-resolved velocity field streamlines with frequency reduction contours for varying splitter plate length ($h = 2\ mm$, $L = 80\ mm$, $V = 90\ m/s$)

which form and convect this half cycle are indicated by the black dots. The influence of the splitter plates is clearly observed in this figure, as the center of the circulation zones in each quadrant of the flow are shown to translate through the flow field almost perfectly parallel to the frequency reduction contour lines. Moreover, the strength and frequency of the oscillations is further reduced as the splitter plates extend further across the circulation zones. In the extreme case, as a set of splitter plates which extends entirely through the desired circulation zone path is used, the oscillations are completely eliminated. Therefore, as the extent the circulation zone development is increasingly restricted, it becomes more difficult for the oscillations to sustain themselves in a repeatable manner. Furthermore, the delay in the development and convection of the circulation zones causes the total period of the oscillations to increase as well. Interestingly, even as the splitter plates become relatively long ($\approx 0.25L$), the oscillations are still observable, albeit considerably weakened, over a range of cross-stream locations. However, it is expected that splitting this region to this extent would result in the circulation zones being unable to coherently form and convect, resulting in the elimination of the oscillations. The ability of the oscillations to persist under these conditions, as well as exploring further countermeasures to increase the effectiveness of the splitter plates, will be discussed in Sections 6.4 and 6.5, respectively.

6.3   Effect of splitter plate location

Similar analysis to that above will now be extended to splitter plates with constant length, however for varying downstream location (S_x). The analysis will once again be conducted for the base case consisting of a slot width of 2 mm, impingement distance of 80 mm and jet exit velocity of 90 m/s. As shown in Figure 6.7, the downstream distance is defined as
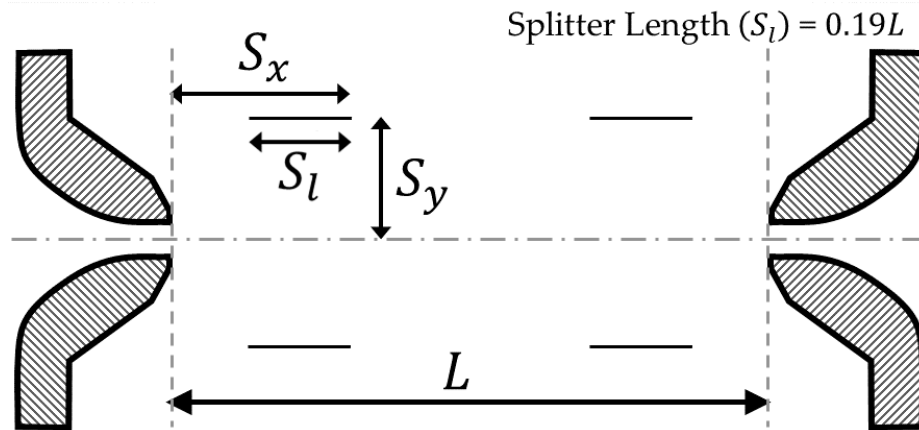
Figure 6.7: Schematic of splitter plate location experiment with opposing planar jets

the distance from the jet exit plane to the leading edge of the splitter plates. The cross-stream location is once again varied, while the splitter plate length is maintained to be 15 mm ($0.19L$). The downstream location is varied from $0.19L$ to $0.50L$, where the lower limit indicates the case where the back edges of plates are aligned with the jet exit plane and the upper limit is where the plates are touching one another in the impingement plane ($x = 0\ mm$). Once again, care is taken to ensure the splitter plates are located symmetrically in each quadrant of the flow.

The frequency of oscillation which results for each splitter plate case, relative to the case with no splitter plates, is shown in Figure 6.8. Similar results to those observed for varying splitter plate lengths are observed, as the frequency of oscillation is reduced as the splitter plates are located in regions where the circulation zones develop and convect. However, for splitter plates cross-stream locations further than $0.25L$ from the centerline, slight increases in the frequency are observed as the downstream distance increases. The phase-resolved velocity field will be presented below with the frequency reduction contours to better understand what the cause of this increase is. For smaller values of cross-stream distance ($< 0.25L$), increasing the downstream distance of the splitter plates reduces the
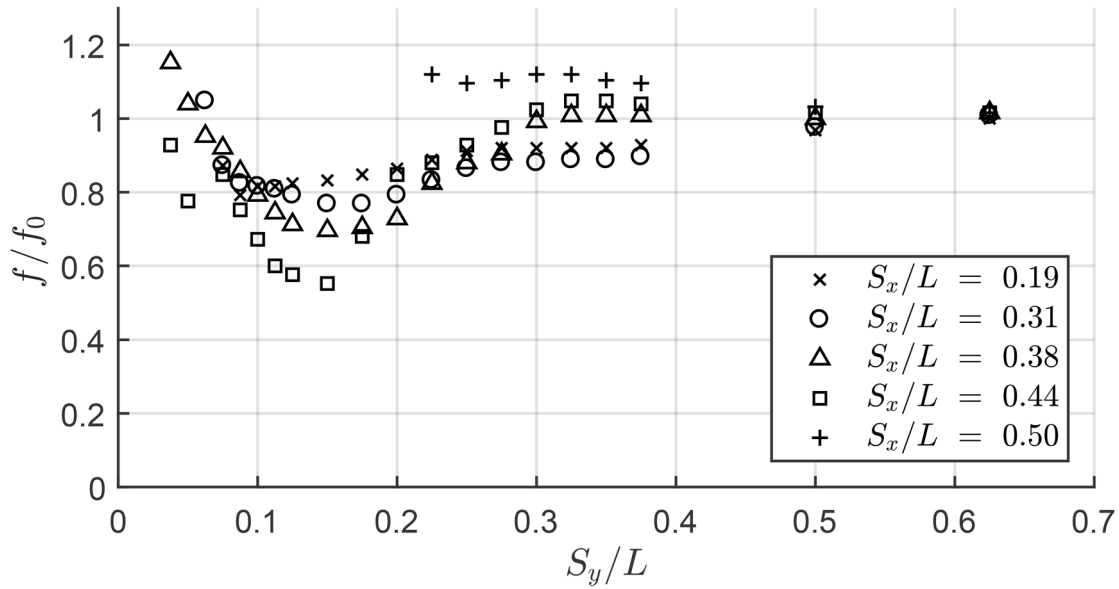
Figure 6.8: Impact of splitter plate location on relative frequency of oscillation ($h = 2\ mm$, $L = 80\ mm$, $V = 90\ m/s$)

frequency of oscillation. For the case of $S_y \approx 0.25L$, the observed frequency of oscillation appears to be independent of the downstream location, as the frequency reduction remains a constant value of approximately 10%. The frequency reduction appears to be maximized at a cross-stream location of $0.15L$. Increasing or decreasing the cross-stream displacement from this location results in an increase in the oscillation frequency. As discussed later, this is a result of the splitter plates being located such that they are centred in the convection path of circulation zones. Finally, for the furthest downstream case ($S_x = 0.5L$), the oscillations cease for cross-stream locations closer than $0.22L$.

The same frequency reduction data can be presented again in contour form, as shown in Figure 6.9. The white area observed for small cross-stream locations, which represents regions where oscillations are not observed, is much smaller than that for the splitter plate length experiment. Even though, in this region, the splitter plates are located near the jet column, the splitter plates do not significantly impede on the desired path of the circulation
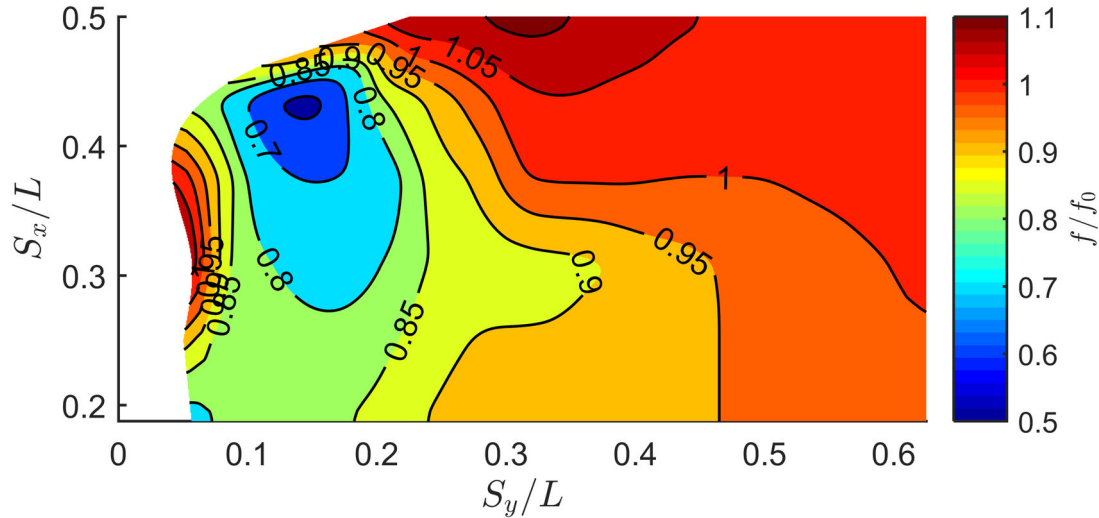
Figure 6.9: Contour plot of impact of splitter plate location on relative frequency of oscillation ($h = 2\ mm$, $L = 80\ mm$, $V = 90\ m/s$)

zones as they form and convect. Furthermore, the large gap between the nozzles and the back of the splitter plates allows the circulation zones to interact with the jet exit regions and thus the oscillations persist, albeit with a reduced frequency and strength. In general, the frequency reduction is observed for cross-stream locations form $0.1L$ to $0.4L$. The maximum reduction in the frequency is observed around $S_x = 0.42L$ and $S_y = 0.14L$. Furthermore, for a cross-stream location of $0.33L$, an increase in the frequency is observed as the plates are located near the impingement plane. This increase in the frequency is likely a result of the flow being prevented from effectively convecting away from the impingement region as the jets deflect. As a result, more streamwise momentum is conserved, which causes the circulation zones to form and grow quicker, effectively decreasing the oscillation period.

The frequency reduction contours are once again plotted with the phase-resolved velocity streamlines for the case with no splitter plates. Figure 6.10 shows a single phase in the oscillation cycle with an example splitter plate case (light blue lines) at $S_x = 0.32L$ and $S_y = 0.34L$, resulting in a 10% frequency reduction. Again, the grey region indicates the
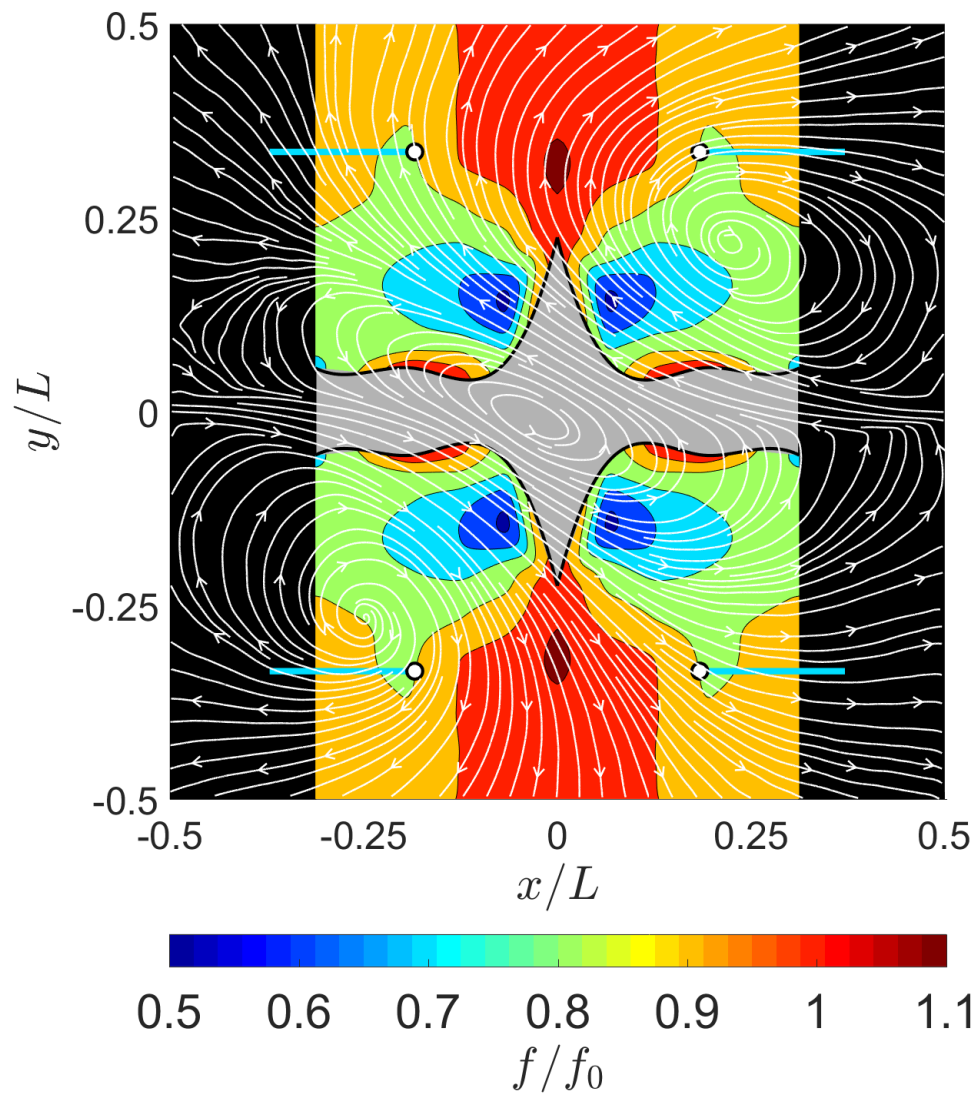
Figure 6.10: Phase-resolved velocity streamlines with example splitter plate location experiment at $S_y = 0.34L$ and $S_x = 0.32L$

regions where the oscillations are not observed and the black regions represent points outside the range of possible test cases as the smallest downstream location of $S_x = 0.19L$ represents the case where the back edge of the splitter plates meets the jet exit plane ($x = \pm L/2$). Figure 6.11 shows the velocity streamlines over four phases in the oscillation cycle, accompanied by the frequency reduction contours. Again, the center of the circulation zones which are formed and convect this half cycle are indicated by the black dots. The splitter plates appear to be most effective as they are located across the region where the circulation zones convect. Moreover, the effectiveness is exacerbated for smaller cross-stream locations, where the circulation zones form and grow rapidly. By disrupting the convection of the circulation zones, the time required for it to grow and translate away from the jet columns is increased, and so too is the total period of oscillations. An increase in the frequency is observed for larger downstream distances at cross-stream locations between $0.25L$ and $0.40L$. In this region, the frequency of oscillation increases above what is observed for the case with no splitter plates. This is likely a result of the plates being located far enough downstream that they do not significantly affect the circulation zone development or convection, but limit the maximum deflection of the jets and prevent the flow from effectively convecting away from the impingement region in the cross-stream direction. The result is more streamwise-momentum preserved, causing a decrease in the time required for the circulation zones to form. Finally, for cases with large downstream distances and cross-stream locations greater than $0.40L$, the impact of the splitter plates on the oscillations is negligible. Therefore, similar to the case with varying splitter plate length, the more the splitter plates impede on the development and convection of the circulation zones, a larger decrease in the strength and frequency of the oscillations is observed.
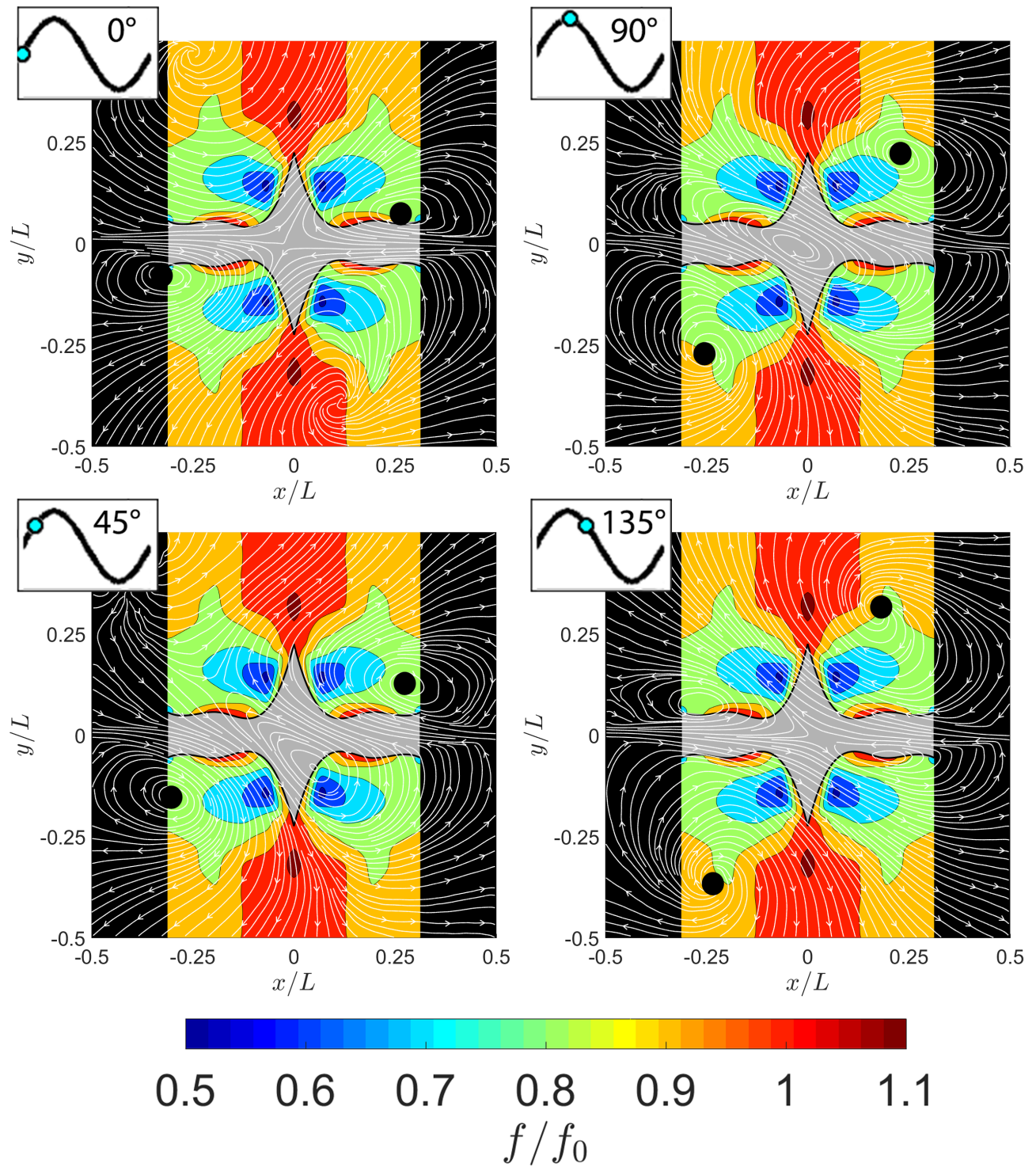
Figure 6.11: Phase-resolved velocity field streamlines with frequency reduction contours for varying splitter plate location ($h = 2\ mm$, $L = 80\ mm$, $V = 90\ m/s$, $S_l = 0.19L$)

6.4   Impact on self-sustaining mechanism

In general, the influence of the splitter plates on the opposing planar jet oscillations is to reduce the frequency and strength of the oscillations. The extent of this influence appears to depend on the degree of obstruction imposed on the path of the circulation zones as they develop and convect away from the jet columns. While previous analysis compared the splitter plates effectiveness with respect to the case with no splitter plates, an example case will now be presented to directly observe the influence of the splitter plates on the flow field characteristics. Phase-locked flow visualization is conducted for the base case with splitter plates of length of $0.20L$ and cross-stream location $0.13L$. Similar to the splitter plate length experiments, the back edges of the plates are aligned with the jet exit plane. Eight phases of the phase-resolved velocity field are shown in Figure 6.12, with the grey regions indicating the location of the splitter plates and the red regions identifying the small areas of the flow field which are outside of the field of view as a result of the existence of the splitter plates. The splitter plates are made of 3 mm acrylic and are clamped at the top and bottom using a custom holder.

The quality of the oscillations is significantly reduced as a result of the existence of the splitter plates in the flow field, resulting in a reduction in the consistency of the oscillations from one cycle to the next. As a result of the phase-resolved measurements depicting an averaged representation of the oscillations, some of the less coherent features of the flow field may not be as clearly observed. Nonetheless, two key aspects of the flow oscillations can be detected. The first of which is the circulation zones are forced to form much further away from the jet exits. Consequently, the ability of the circulation zones to effectively drive the jet columns back and forth is significantly hindered. Secondly, as the circulation zones convect away from the jets, they appear to remain attached to the downstream edge of the
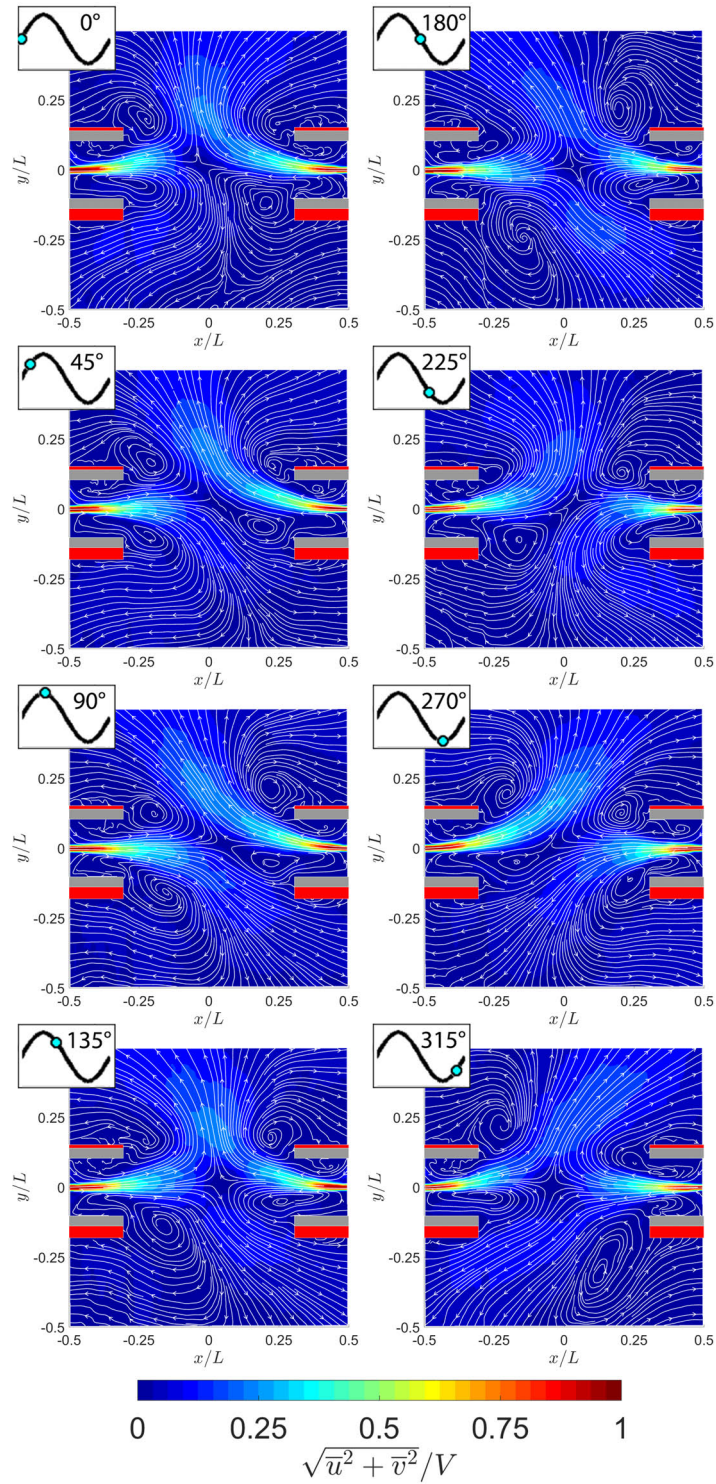
Figure 6.12: Phase-resolved velocity field showing impact of splitter plate on the flow field ($h = 2$ mm, $L = 80$ mm, $V = 90$ m/s, $S_l = 0.20L$, $S_y = 0.13L$) (grey = splitter plate, red = out of field of view)

155

splitter plate until they quickly disperse and are generally not observed for cross-stream distances greater than $0.25L$. However, reviewing each set of phase-locked instantaneous PIV measurements, the circulation zones are observed at larger cross-stream locations, but they are considerably weakened and follow varying trajectories. Therefore, the circulation zones no longer convect in a repeatable trajectory from one cycle to the next, and as a result they are 'averaged out' of the phase-resolved images. Both observations of the flow field indicate the severity to which the splitter plates are impeding the consistent development and convection of the circulation zones, which the self-sustaining mechanism relies upon. Furthermore, while care is taken to ensure the splitter plates are located symmetrically in the flow field, the flow field appears to be highly sensitive to slight variation in the relative locations, as even slight asymmetries drastically influences the flow field. Even after considerable effort is directed towards aligning the plates at precisely the same relative location in each quadrant of the flow field, the flow field shown in Figure 6.12 is still slightly skewed upward. While the skewness is small, it can be observed for the phases in the oscillation cycle where the jets impinge directly on one another (0° and 180°), as the momentum of both jets is oriented slightly upward after impingement. This is not surprising as a result of the unstable nature of the impinging jet flow and the high sensitivity of the circulation zone convection with the cross-stream location of the splitter plates. Circulation around the outer edges of the plates is also observed in the phase-resolved images as the streamlines pass around the plates and back towards the gaps between the plates and the nozzle faces. The flow which passes around the plates and through the gaps behind the plates will be shown to play a vital role in the splitter plates' influence, as its impact on the jet deflection process will be the primary focus of the following section.
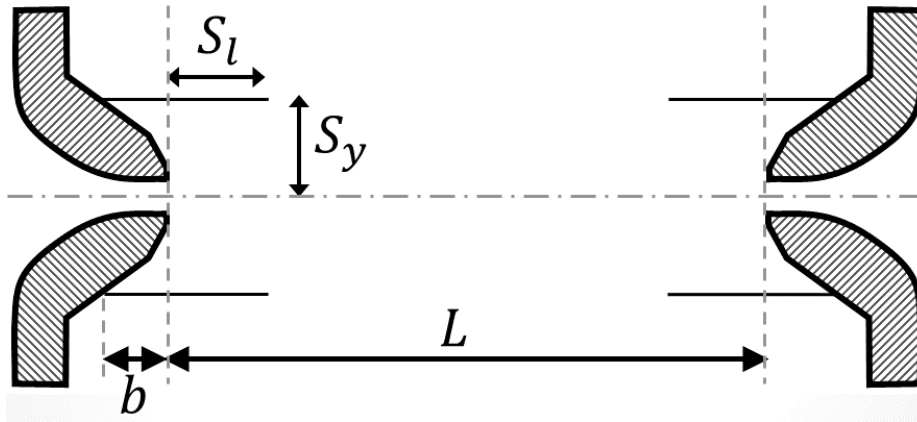
Figure 6.13: Schematic of gaps closed splitter plate length experiment with opposing planar jets

6.5   Effect of gap between nozzle and plate

While the previous splitter plate arrangements effectively disrupted the oscillations, it is surprising that the oscillations persisted even as the splitter plates became long enough to impede on a significant portion of the desired path of the circulation zones. Careful analysis of these splitter plate cases reveals small gaps between the upstream edge of the plates and the nozzle surfaces. Figure 6.13 shows a schematic of the same splitter plate length experiment as that discussed previously, but for the case with the gaps closed. Again, the cross-stream location (S_y) is defined as the distance from the jets' common centerline to the plate, while the length of the splitter plates (S_l) is the length the plates extend downstream of the jet exit plane and the gap (b) is distance between the nozzles and the upstream edge of the plates. The base case of a slot width of 2 mm, impingement distance of 80 mm and jet exit velocity of 90 m/s is used once again. To close off the gaps, the plates are extended upstream to the nozzle face and tape is used to ensure the gaps between the plates and the nozzles are completely sealed. The tapered shape of the nozzle results in varying total length of the plates used as a result of the increased size of the gap behind the jet exit plane for
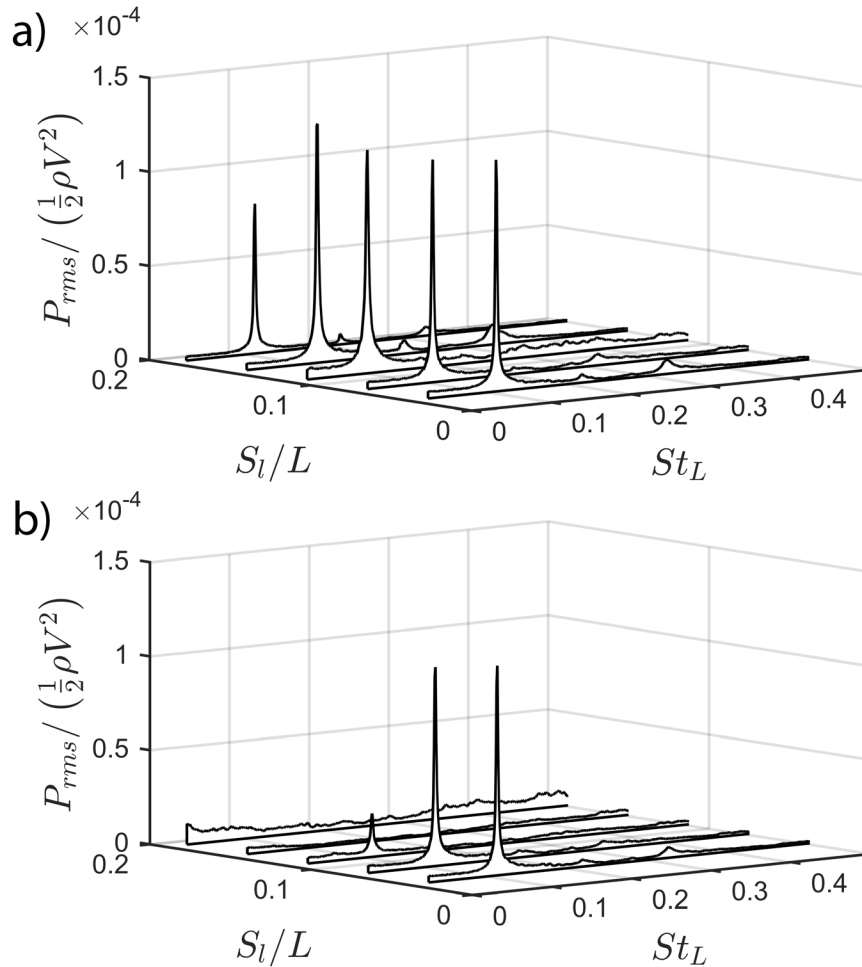
Figure 6.14: Impact of splitter plate gap on acoustic response spectra for a) gaps open and b) gaps closed ($h = 2\ mm$, $L = 80\ mm$, $V = 90\ m/s$, $S_y = 0.16L$)

larger cross-stream distances. Therefore, only a limited range of cross-stream location are investigated to ensure the plates are of similar total length.

The effect of the splitter plate gap on the acoustic response characteristics is revealed in Figure 6.14, for various splitter plate lengths at a cross-stream location of $0.16L$. Subset a) shows the cases with the gaps open and subset b) shows the cases with the gaps closed. The splitter plate lengths varied from $3\ mm$ to $15\ mm$ in increments of $3\ mm$. For the gaps open cases, the spectra, including both frequency and amplitude, remained fairly consistent

for all the cases shown, as a result of the relatively short splitter plates used. Even though the splitter plates appear to be relatively ineffective over this range when the gaps are open, the same cases with the gaps closed prove to be much more effective. For the shortest plates ($< 0.11L$), there does not appear to be a large impact on the oscillations. However, once the splitter plates became $0.11L$ long, the oscillations almost suddenly disappeared. A small peak is observed for the case of $0.11L$, as the signal is very intermittent. Oscillations are not observed for most of the recording time, except short instances every few seconds where they randomly initiate with weak amplitudes and then disappear again.

The same analysis can be conducted for a variety of impingement distances and jet exit velocities. Figure 6.15 shows spectra for a range of parameters with splitter plates consistently of length $0.20L$ and cross-stream location $0.13L$. Each plot shows the acoustic response for the case with no splitter plates, as well as splitter plates with the gaps open and closed. For each case, the addition of the splitter plates with the gaps open show a consistent decrease in the frequency and amplitude, while closing off the gaps eliminated the oscillations completely. It is apparent that short splitter plates with the gaps closed are very effective at disrupting the oscillations even though the plates are located in the circulation zones, away from the jet column and impingement region. This splitter plate location and length is chosen as it effectively disrupts the region where the circulation zones first form.

The influence of the splitter plates on the flow field characteristics associated with the oscillations, in particular the development and convection of the circulation zones, is apparent in the phase-resolved images presented previously for the gaps open. However, it is not as obvious for the case with the gaps closed as a result of the oscillations being completely eliminated. To effectively compare the flow fields between the cases with the gaps open and closed, the steady-mean velocity field must be compared. The steady velocity field is
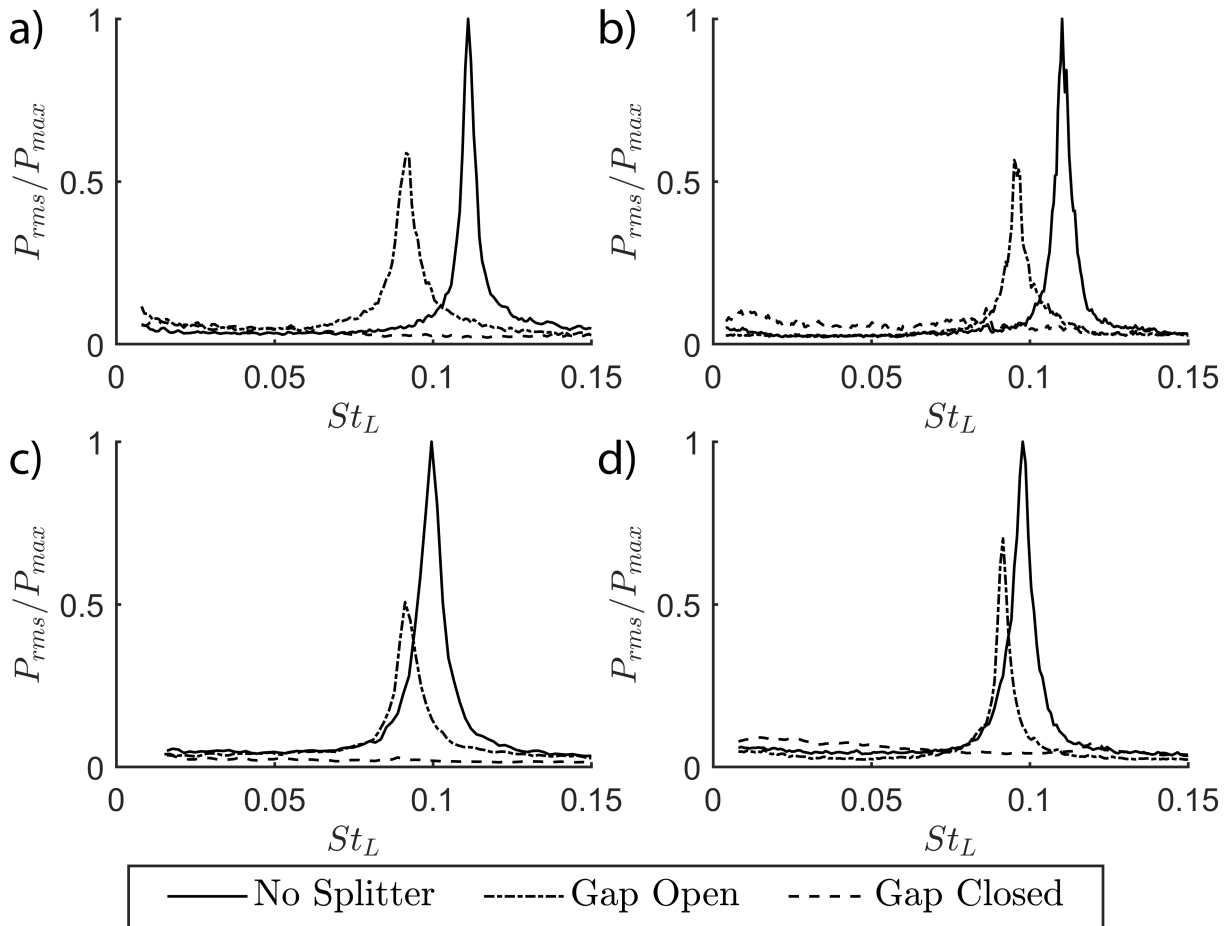
Figure 6.15: Impact of gaps between splitter plates and nozzles on acoustic spectra for a) $L = 80\ mm$, $V = 90\ m/s$, b) $L = 80\ mm$, $V = 180\ m/s$, c) $L = 160\ mm$, $V = 90\ m/s$ and d) $L = 160\ mm$, $V = 180\ m/s$ ($h = 2\ mm$, $S_l = 0.2L$, $S_y = 0.13L$)
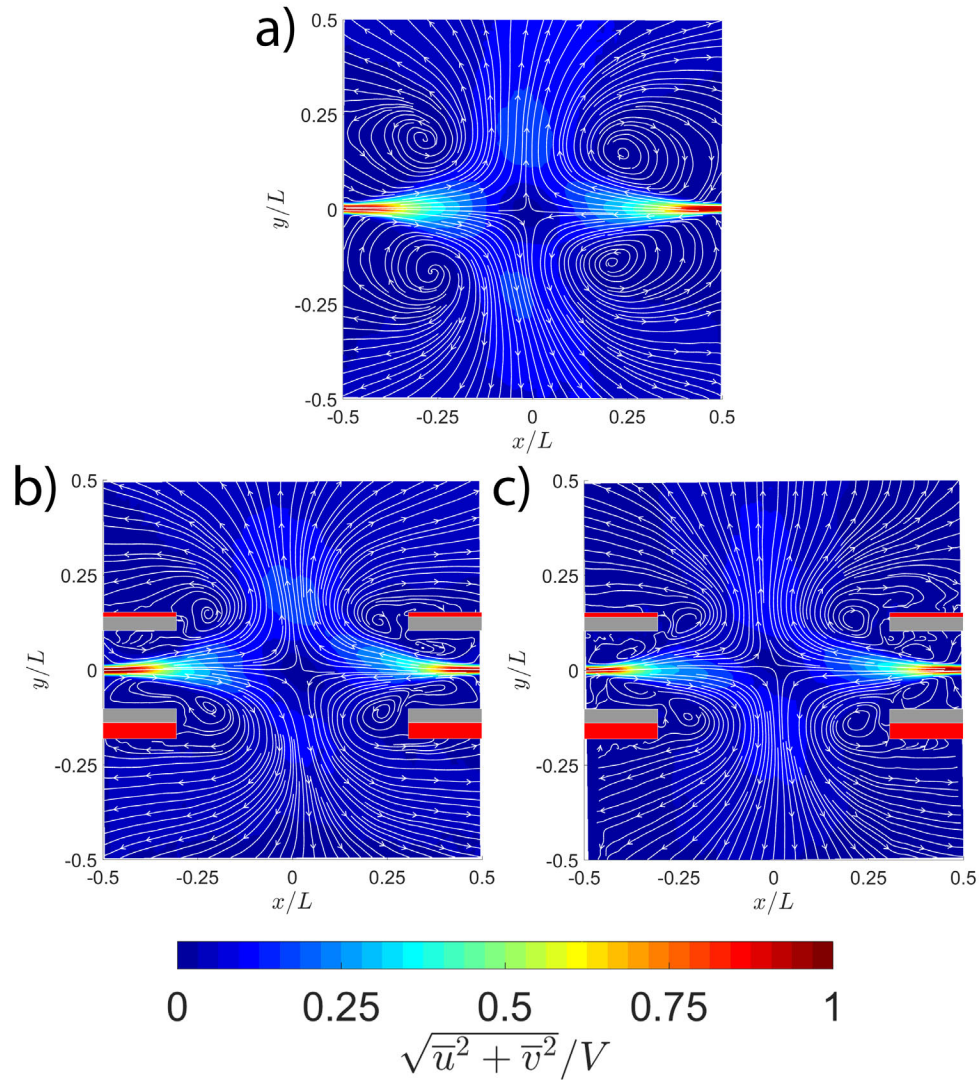
Figure 6.16: Time-averaged velocity field for a) no splitter plate and splitter plates with b) gaps open and c) gaps closed ($h = 2\ mm$, $L = 80\ mm$, $V = 90\ m/s$, $S_l = 0.20L$, $S_y = 0.13L$) (grey = splitter plate, red = out of field of view)

presented in Figure 6.16 for the cases with no splitter plates and splitter plates with the gaps open and closed. The same base case with splitter plates of length $0.20L$ and cross-stream location of $0.13L$ is used. Again, the grey regions indicates the location of the splitter plates, while the red regions are areas outside the field of view of the PIV. The impact of the splitter plates as they are added to the flow with the gaps open is most apparent, as the location and size of the circulation zones are significantly impacted. However, as the gaps are closed, very little variation in the steady mean velocity field is observed. Subtle differences can be detected as the flow which passes around the back of the plates, towards the jet exits, is observed by the streamlines for the case with the gaps open. As well, the circulation structures around the outer edges of the plates appear to be more coherent in the case with the gaps open, as indicated by the streamlines. However, with the exception of this subtle difference, no key indicators of the gaps' influence on the oscillations are observed in the steady-mean velocity fields, and little insight is provided as to why the oscillations are eliminated.

In addition to the steady-mean velocity field, the instantaneous velocity fields can also be analysed for each case. In particular, the variation in the deflection angle of the jets over a series of instantaneous measurements taken randomly throughout the oscillation cycle can be examined. Figure 6.17 shows the probability distribution of the instantaneous jet deflection angle over a series of 1500 images taken randomly for the case with no splitter and with splitter plates where the gaps are open and closed. Very interesting trends in the deflection angle distribution are observed. For the case with no splitter plates, the deflection angle distribution shows a large maximum near a deflection angle of $0°$, and a quick decay in the probability as the deflection angle increases. As the splitter plates are added with the gaps open, the distribution becomes wider as the jets are deflected away
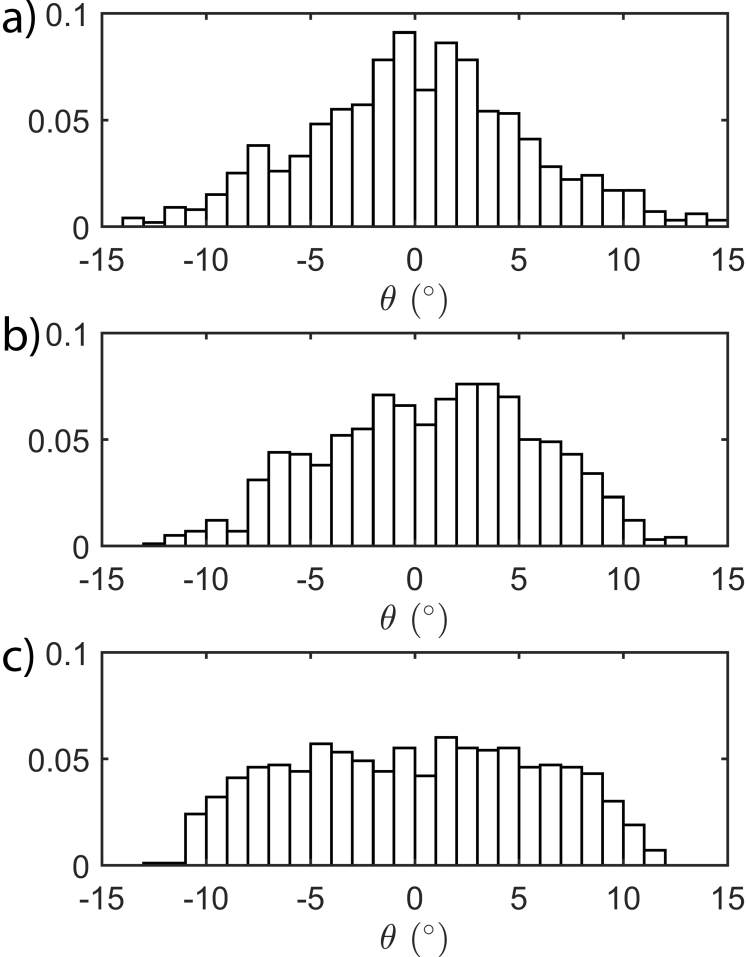
Figure 6.17: Probability distribution of jet instantaneous deflection angle over sample of instantaneous velocity fields for cases with a) no splitter plate and splitter plates with b) gaps open and c) gaps closed

from the centerline for longer portions of the oscillation cycle. Finally, as the gaps are completely closed, the probability distribution is almost uniform over the range of deflection angles observed. Interestingly, the more the circulation flow around the back of the plates is restricted, the more chaotic the jet column oscillations are. As the interaction of the circulation flow with the jet exit region is completely eliminated, the jets no longer generate coherent oscillations and thus the self-sustaining mechanism is suppressed. Many of the applications where these oscillations generate unwanted part defects or process inefficiencies can be considerably improved through use of splitter plates in the circulation zones.

6.6   Conclusion

Splitter plates are found to be an effective device to mitigate the opposing planar jet oscillations. This is achieved by locating splitter plates in the circulation regions of the flow field, away from the jets, such that they do not directly interact with the jet columns nor the impingement region. By disrupting the development and convection of these circulation zones, which are essential to the self-sustaining mechanism, the oscillations are severely hindered. The more the splitter plates impede on the desired path of the circulation zones as they develop and convect away from the jets, the more severely the oscillations are affected. In particular, the frequency, amplitude and quality of the tones produced are diminished, and in many cases, the oscillations are eliminated altogether. Flow visualization showed a case where the splitter plates disrupted the convection and dissipating process of the circulation zones and delayed the jets from returning to the centerline in a repeatable and robust manner. Therefore, the jets require more time to complete a full oscillation cycle and the period of the oscillations is extended. Even though the circulation zones are considerably disturbed in a variety of cases with longer splitter plates, many still resulted in oscillations

being observed, albeit weak. To improve the effectiveness of the splitter plates, the gaps between the back of the plates and nozzles are closed. This results in the circulation flow around the splitter plates to be completely eliminated, and as a result, the mechanism in which the circulation zones are able to dissipate repeatedly is also disrupted. Consequently, no coherent oscillations are observed as the jets chaotically flipped orientation. Closing off the gaps proved effective at eliminating the oscillations, even as the splitter plate lengths became relatively short. For example, a set of splitter plates consisting of a length $0.20L$ and a cross-stream location of $0.13L$ eliminated the oscillations for a range of parametric cases. The ability of the splitter plates to effectively eliminate the coherent oscillations makes them a viable solution for a wide range of applications where the oscillations are unwanted.

Chapter 7

Conclusion

7.1   Summary and conclusions

A fundamental investigation of the opposing planar jet oscillator has been presented, which includes the aeroacoustic response characteristics, the role of pressure in the self-sustaining mechanism and the establishment of effective countermeasures. However, in order to detail the time-varying pressure field which drives the jet oscillations, the development and benchmarking of an original PIV pressure field mapping technique was necessary. The developed technique relies on the ability to decompose the flow field into a periodic mean component, which follows the oscillations, and a fluctuating component away from this mean motion. While the proposed technique is applicable only for flow phenomena which contain dominant periodic features, it offers a number of unique benefits over existing methodologies. One of the most notable benefits of the proposed technique, is its ability to resolve detailed time-varying data in a reliable and precise manner, without the need for expensive and often unattainable PIV systems and techniques. The ability of the proposed technique to isolate the phase-resolved velocity and pressure features which are directly linked to the periodic

flow being investigated, and remove other flow features which follow different time scales, allows one to more easily study the kinematic and dynamic aspects of the fluid oscillations of interest. This is particularly valuable in the areas of fluid-structure-interaction and aeroacoustics, where these flow features often prove very difficult to simulate and existing experimental methodologies do not reliably provide a time-varying description of the entire pressure field. While in the present investigation, microphone and transducer signals are used to reliably trigger the PIV measurements, the developed technique will be extremely effective in cases where external excitation is introduced (i.e periodic forcing or acoustic excitation). In these cases, the synthetic signal used to apply the force can be utilized to precisely and repeatedly phase-lock the PIV measurements and the resulting flow features can be investigated. The technique is benchmarked against traditional pressure measurement methodologies for the case of the planar jet impinging on a v-shaped plate. Specifically, time and spectral characteristics of the PIV pressure field are evaluated against fast-response transducer data recorded at various locations along the plate, and excellent agreement is observed.

The acoustic response of the opposing planar jets is then investigated for a more comprehensive set of flow parameters. This ultimately allows for a more complete understanding of the opposing planar jet oscillations, while also helping to draw links between the various existing studies in the literature which reported a range of Strouhal numbers, each for relatively narrow ranges of parameters. Because significant variation in the Strouhal number over the flow parameters investigated is observed in the literature, an effective impingement length is introduced to help resolve the variation in the Strouhal number for a given jet aspect ratio. However, a very unique trend is observed, as the Strouhal number of the oscillations is shown to decrease as the aspect ratio of the jets increases, even as the aspect

ratio of the jets extends into a region which is well documented to generate two-dimensional flow. Flow visualization shows that increasing the aspect ratio of the jets resulted in an increased momentum transfer to the cross-stream direction and circulation zones which form further from the jets' common centerline. While the root cause of the variations in the flow features for varying aspect ratio is unknown, it appears that larger aspect ratio jets generate larger circulation zones which ultimately take longer to develop and dissipate, resulting in an extended oscillation period.

To gain further insight into the self-sustaining mechanism of the opposing planar jet oscillator, the PIV-based pressure field mapping technique developed in this thesis is used to detail the time-varying pressure field. Phase-resolved velocity and pressure measurements are presented and unique flow features associated with the jet oscillations are investigated. A high-pressure region is shown to form in the impingement plane which drives the jets away from one another, however the low-pressure regions which periodically develop and dissipate in each quadrant of the flow are shown to drive the jet columns back toward, and across, the centerline. Careful analysis of the pressure field over the oscillation cycle shows the pressure field is powering the oscillations through the low-pressure regions and minimal net energy is exchanged in the impingement region. This is a result of the high pressure in the impingement region growing in strength as the jets approach the centerline, which creates a force which prevents the jets from returning to the centerline. However, the ability of the low-pressure regions on either side of the jets to grow quickly during this process overcomes the resisting force generated in the impingement region and allows the jets to return to the centerline in a repeatable and organized fashion. Furthermore, the fundamental tone radiated from the opposing planar jet flow field is radiated from a quadrupole source field with the nodal planes along the jets' common centerline and impingement plane. This is a

result of the asymmetrical growing and dissipating of the circulation zones in each quadrant of the flow field. However, the high-pressure region which forms in the impingement plane each half cycle as the jets impinge upon one another creates a monopole shaped sound-source field for the first harmonic. The higher harmonics are shown to generate pressure pulsations over an order of magnitude lower, and thus the acoustic response characteristics are dominated by the fundamental and first harmonic frequency components.

In an attempt to disrupt the development and convection of the circulation zones, which are an essential feature to sustaining the oscillations, splitter plates are introduced to the flow field in these regions. The more the splitter plates are shown to impede on the development and convection path the circulation zones, the larger the observed impact is on the oscillation characteristics. Specifically, the frequency, amplitude and quality of the tones produced are reduced, and in many cases the oscillations are eliminated all together. By disrupting the development and dissipation process of the circulation zones, the ability of the jets to deflect and return to the centerline in a repeatable and robust manner is hindered. Consequently, the coherence of the oscillations is reduced and the time required for the jets to complete a full oscillation in each direction is extended. The effectiveness of the splitter plates is shown to increase drastically as the gaps between the nozzles and the back of the plates, near the jet exits, is closed. Even for many short splitter plate cases, no coherent oscillations are observed as the jets chaotically flip orientation. Results are shown to be consistent for the wide range of investigated jet parameters. The splitter plates located in the circulation regions are shown to be a very effective mitigation strategy of the opposing planar jet oscillator and is applicable in a wide range of applications as a result of the ability to disrupt the oscillations while not intruding directly on the jet flow and the impingement plane, which many applications rely upon.

7.2   Contributions to the state of knowledge

The present investigation has resulted in a more substantial understanding of the opposing planar jet oscillator and the associated self-sustaining mechanism. An original PIV-based pressure field mapping technique was also introduced and benchmarked to resolve the need for a detailed depiction of the complex time-varying pressure field which drives the jet oscillations. The main contributions which have arisen from the present work include;

1. Detailing the underlying mechanism which drives the jet columns away and back towards the centerline in a repeatable and robust manner. Demonstrating the necessity of the circulation zones and associated low-pressure regions in this process.

2. Establishment of effective countermeasures in suppressing the opposing planar jet oscillations using relatively non-intrusive and industrially applicable means.

3. Development and benchmarking of an original PIV-based pressure field mapping technique which effectively determines the time-varying pressure field which are synchronized with flow oscillations. The method can be extended to a variety of fields, especially in the area of fluid-structure-interaction and aeroacoustics where understanding the detailed pressure field is often a necessary and difficult challenge.

4. Examination of the unique impact of the jet aspect ratio on the oscillation frequency, as well as the associated flow dynamics, which helps explain much of the discrepancy in the Strouhal number reported in the literature.

5. Response characterization of the opposing planar jets over a more complete range of impingement ratios, slot widths and jet exit velocities.

6. Demonstration of the influence of the jet cores on the oscillation frequency and the introduction of an effective impingement length to help reduce variation in reported Strouhal numbers.

7. Characterization of the source field of the acoustic tones which are radiated from the opposing planar jet oscillator.

7.3   Recommendations

While this thesis does provide a fundamental understanding of the self-sustaining mechanism of the opposing planar jet oscillator, it also reveals a number of areas where further research is necessary. Two recommendations which are proposed for future work include an investigation into the root cause of the variation in the oscillation characteristics with the aspect ratio of the jets, as well as the effect of asymmetry on the opposing planar jet oscillations as it pertains to practical applications. Variation in the aspect ratio of the jets is shown to have a significant impact on the Strouhal number of the oscillations. Analysis of the flow field indicated that an increased aspect ratio caused an increase in the size of the circulation zones, as well as the amount of momentum transferred to the cross-stream direction. The increased time required for these regions to develop and dissipate resulted in a reduced frequency of oscillation. However, it is not clear what the root cause of the variation in the flow field dynamics is. A variety of possible explanations are proposed in Appendix C.

The second recommendation pertains to the impact of asymmetry on the opposing planar jet oscillations. Care is taken in this work to ensure the jets directly opposed one another and no variation in the exit velocities or slot widths are presented between the two jets. However, in most practical applications this is not necessarily the case, as variations in the momentum

of each jet may be observed, as well as the jets may be offset (in the cross-stream direction) from one another and/or oriented on slight angles relative to one another. Preliminary work has shown that as the jet angles and offset are varied, typically there are conditions where the jet oscillations suddenly onset or disappear as the jets are oriented closer or further from each other, respectively. Furthermore, the points at which the oscillations onset and disappear are often not the same. For example, as the jets are oriented directly on one another and the offset is slowly increased, the oscillations suddenly disappear as the offset increases above a specific threshold. However, as the offset is slowly decreased and the jets approach one another, the oscillations onset at a smaller offset distance. The nature of the flow conditions which are present when the jet oscillations onset and disappear will provide valuable insight into the necessary conditions for the oscillations to persist. Furthermore, a collection of design recommendations which suggest the required asymmetry to control and/or prevent the oscillations from persisting will provide considerable value for engineers implementing opposing planar jets for practical means.

Appendix A

Uncertainty analysis

This appendix reviews the major sources of error regarding the measurement equipment and techniques utilized throughout the course of this investigation. The error propagation in each measurement is determined using the Kline and McClintock method where the uncertainty of the dependent variable (δY) is determined by the square sum of the uncertainties associated with each independent variable (δX_i),

$$\delta Y = \sqrt{\sum_i \left(\frac{\partial Y}{\partial X_i} \delta X_i \right)^2} \tag{A.1}$$

The geometric parameters of this investigation, including the slot width (h), initial impingement distance (L), the location of the splitter plates $(S_x$ and $S_y)$, are measured using high precision feeler gauges which result in a maximum uncertainty of ± 0.01 mm. While the initial impingement distance and splitter plate locations are set using feeler gauges, the location is controlled using a Velmex RS232 controller with a Vexta PK266-03A stepper motor (630 $steps/mm$) in full stepping mode, which corresponds to an uncertainty of 1.6 μm. The splitter plates are machined such that the accuracy of the splitter plates lengths (S_l) is

within 5 μm. The jet exit velocity (V) is controlled by measuring the plenum pressure using Validyne DP15 pressure transducers in conjunction with Validyne CD23 signal conditioners, resulting in a maximum uncertainty of $\pm 2.5\%$, then relating it to the exit velocity using the isentropic nozzle equation presented as Equation 3.1. The range of pressure measurements varies from 5.0 kPa at a velocity of 90 m/s to 20.9 kPa at a velocity of 180 m/s. The plenum pressure for the small subset of experiments conducted at lower flow velocities is measured using a Fluke 922 micromanometer ($\pm 1\%$). Care is taken to ensure the fluctuations in the pressure signal throughout the course of the investigation are within ($\pm 0.9\%$). The isentropic efficiency (η) is known to be a minimum of 88.5% throughout the range of velocities studied and thus no correction factor is applied, resulting in an uncertainty of 1.5%. The speed of sound of air is determined as,

$$c = \sqrt{(\gamma R T)} \tag{A.2}$$

Where γ is the ratio of specific heats (1.400), R is the ideal gas constant (287.04 J/kgK) and T is the absolute temperature in Kelvin. While the variations in the ratio of specific heats is small, the temperature is measured for each experiment using a thermocouple in the airline immediately upstream of the jet assemblies. Time is allowed prior to each set of experiments for the temperature of the airline to reach steady-state. As a result of the enclosures around the experimental facility, the ambient temperature drops to that of the airline, and thus the airline temperature is used. The maximum variations of the temperature over all the measurements is observed to be $\pm 2K$. Ambient pressure (P_∞) is determined using a digital barometer and is determined to vary within 0.2 kPa. Using Kline and McClintock method,

the error in the velocity measurements is determined as,

$$\delta V = \sqrt{\left(\frac{\partial V}{\partial \eta}\delta \eta\right)^2 + \left(\frac{\partial V}{\partial c}\frac{\partial c}{\partial T}\delta T\right)^2 + \left(\frac{\partial V}{\partial P}\delta P\right)^2 + \left(\frac{\partial V}{\partial P_\infty}\delta P_\infty\right)^2} \qquad \text{(A.3)}$$

Which is used to determine the relative uncertainty of the velocity measurements as,

$$\frac{\delta V}{V} = \sqrt{\left(\frac{\delta \eta}{\eta}\right)^2 + \left(\frac{\delta T}{2T}\right)^2 + \left(\frac{\gamma - 1}{2\gamma}\right)^2 \left(\frac{\left(\frac{\delta P}{P_\infty}\right)^2 + \left(\frac{P\delta P_\infty}{P_\infty^2}\right)^2}{\left[\left(\frac{P+P_\infty}{P_\infty}\right) - \left(\frac{P+P_\infty}{P_\infty}\right)^{\frac{1}{\gamma}}\right]^2}\right)} \qquad \text{(A.4)}$$

The maximum relative uncertainty occurred at the maximum measured velocity of 180 m/s and is determined to be $\pm 1.6\%$.

The acoustic measurements are recored using a Type 40BP condenser microphone, Type 26AB preamplifier and a Type 12AA power supply which corresponds to a uncertainty of the RMS pressure amplitudes (P_{rms}) of 3%. As a result of Fast-Fourier Transforms being applied to 1 s samples of the microphone signal, the resolution of the frequency content is within ± 0.5 Hz. The resulting relative uncertainty of the Strouhal number and reduced pressure amplitude are thus determined to be,

$$\frac{\delta St_L}{St_L} = \sqrt{\left(\frac{\delta L}{L}\right)^2 + \left(\frac{\delta V}{V}\right)^2 + \left(\frac{\delta f}{f}\right)^2} \quad \text{and,} \qquad \text{(A.5)}$$

$$\frac{\delta P_r}{P_r} = \sqrt{\left(\frac{\delta P_{rms}}{P_{rms}}\right)^2 + \left(\frac{2\delta V}{V}\right)^2} \qquad \text{(A.6)}$$

The maximum relative uncertainty occurred for the case of minimum velocity (45 m/s) and impingement length (12 mm). For the minimum measured frequency of oscillation (55 Hz), the relative uncertainty is 1.6% for the Strouhal number and 3.9% for the reduced

pressure amplitude. Similar analysis is conducted for the fluctuating pressure measurements using PCB model 112A21 high resolution ICP dynamic pressure transducers. While the uncertainty in the frequency content is similar, the uncertainty in the reduced pressure amplitudes is considerably less (2.5%).

PIV is performed for a variety of cases using the system and procedure outlined in Section 3.3. In addition to the particle tracking error discussed in this section, the main source of error in the PIV investigation is derived from resolving the large displacement gradients of the strong shear flows under investigation. Scarano and Riethmuller (2000) performed extensive analysis of the uncertainty in a PIV study for a similar processing scheme and as such, as similar analysis is employed here. A sample calculation of the uncertainty will now be performed for the 'base case' ($h = 2\ mm$, $L = 80\ mm$ and $V = 90\ m/s$), which is used throughout the course of this investigation. The velocity profile along the planes which observed the maximum displacement gradient in each of the $\overline{u}$ and $\overline{v}$ velocity components are presented in Figure A.1 a) and b), respectively. The maximum $\frac{\partial \overline{u}}{\partial y}$ displacement gradient is observed along the $x = -0.48L$ plane. Through the use of the deformation interpolation scheme with a final window size of 16 $pixels\ square$ and a 50% overlap, a maximum displacement gradient of 0.19 $pixels/pixel$ is observed. This corresponds to a RMS error (ϵ_u) of 0.07 $pixels$, resulting in a relative uncertainty ($\frac{\epsilon_u}{V}$) of 1.7% (Scarano and Riethmuller, 2000). The same analysis is conduced for the $\frac{\partial \overline{v}}{\partial x}$ displacement gradient and the maximum, which is observed along the $y = 0.18L$ plane, of .09 $pixels/pixel$ is observed, corresponding to a RMS error (ϵ_v) of 0.03 $pixels$ and a relative uncertainty ($\frac{\epsilon_v}{V}$) of 0.1%. A list of the PIV uncertainties for all of the cases investigated is presented in Table A.1.

The PIV measurements are then used in the calculation of the pressure fields. De Kat and Van Oudheusden (2012) developed criteria to estimate the uncertainty in the pressure
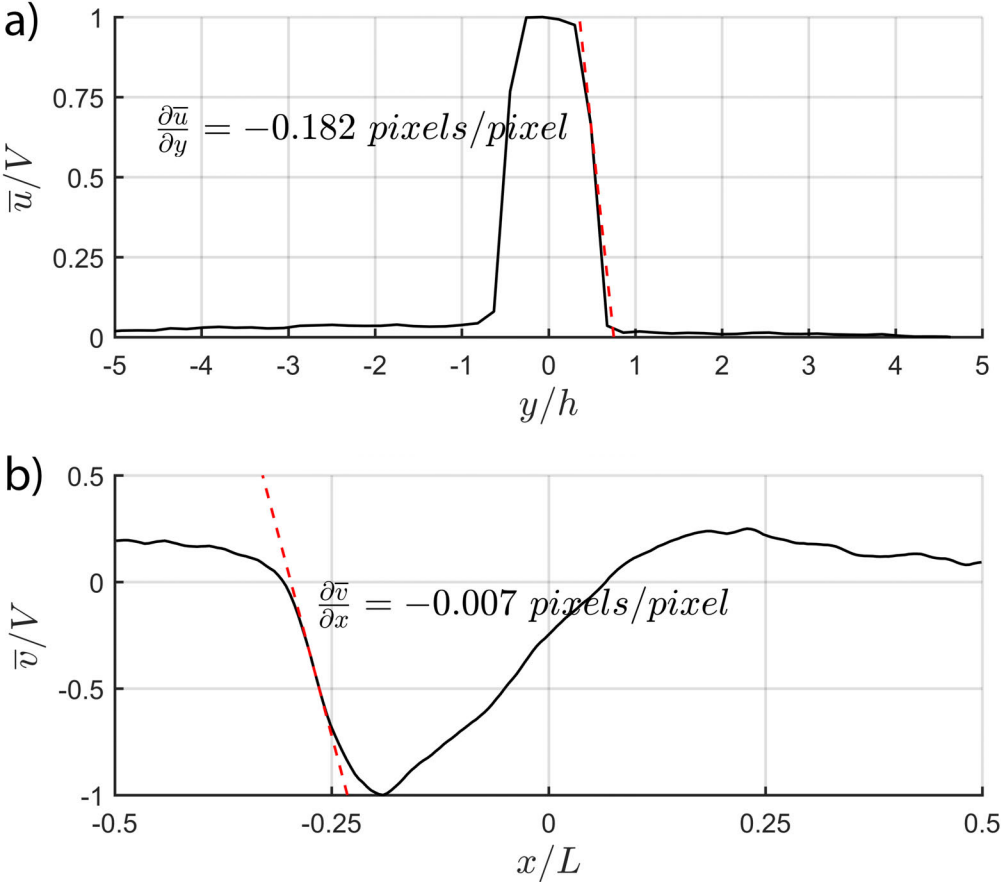
Figure A.1: Sample of maximum displacement gradients observed throughout the flow field for a) $\frac{\partial \overline{u}}{\partial y}$ ($x = -0.48L\ plane$) and b) $\frac{\partial \overline{v}}{\partial x}$ ($y = 0.18L\ plane$)

Table A.1: Summary of uncertainty for each PIV investigation (** jet impinging on v-shaped plate)

h (mm)	L (mm)	V (m/s)	$\frac{\partial \overline{u}}{\partial y}$ ($pixels/pixel$)	$\frac{\partial \overline{v}}{\partial x}$ ($pixels/pixel$)	ϵ_u ($pixels$)	ϵ_v ($pixels$)	$\frac{\epsilon_u}{V}$	$\frac{\epsilon_v}{V}$	
1	40	45	0.134	0.008	0.047	0.006	1.2%	0.1%	
1	80	90	0.172	0.004	0.058	0.005	1.9%	0.2%	
2	40	45	0.116	0.004	0.041	0.005	1.0%	0.1%	
2	40	90	0.129	0.005	0.045	0.005	1.1%	0.1%	
2	80	45	0.165	0.007	0.056	0.005	1.9%	0.2%	
2	80	90	0.182	0.007	0.060	0.005	1.7%	0.1%	
2	80	135	0.178	0.006	0.059	0.005	1.7%	0.1%	
2	120	90	0.189	0.005	0.062	0.005	1.6%	0.1%	
2	120	135	0.184	0.007	0.061	0.006	1.5%	0.1%	
2	160	90	0.177	0.006	0.059	0.005	2.1%	0.2%	
2	160	180	0.121	0.003	0.042	0.005	1.5%	0.2%	
3	80	90	0.134	0.005	0.047	0.005	1.5%	0.2%	
3	120	135	0.169	0.011	0.057	0.006	2.0%	0.2%	
4	80	90	0.083	0.003	0.028	0.005	0.9%	0.2%	
4	160	180	0.144	0.007	0.050	0.005	1.9%	0.2%	
2	40	90	0.114	0.007	0.041	0.005	1.0%	0.1%	**

calculation for *instantaneous* pressure fields. While the current analysis is performed for *phase-resolved* pressure fields, the analysis can be extended to the current investigation. However, as a result of the phase-resolved nature of the proposed technique in the current thesis, the determination of the dependence on the time resolution between consecutive velocity measurements is no longer necessary. As such, the error in the current investigation as it pertains to the spatial gradients in the PIV measurements can be approximated as,

$$\epsilon_p \approx \rho \epsilon_u \sqrt{\left|\frac{\partial \overline{u}}{\partial y}\right|^2 h_r^2 + \frac{|\overline{u}|^2}{2}} \tag{A.7}$$

For the base case, the resulting uncertainty is 71 Pa, corresponding to a relative uncertainty of 12.1%.

The impact of the time dependence of the phase-resolved velocity field on the uncertainty of the analysis has been minimized due to the unique approach of the proposed method in interpolating the time gradients using the model shown in Equation 4.17. The ability of

this equation to accurately resolve the time gradients depends mostly on the ability to repeatedly trigger the PIV system at the same point in the oscillation cycle. By reviewing samples of the microphone and trigger signals taken for each PIV case, the precision of the triggering system can be evaluated. A bandpass filter is applied to the microphone signal around the fundamental frequency and the time difference between the time when the signal is intended to be fired and when it is actually fired is measured. In addition, the increased uncertainty associated with frequency modulation over an oscillation period is also considered. The maximum uncertainty corresponding to triggering process is determined to be $\pm 80 \ \mu s$, which corresponds to approximately $\pm 4°$ in the oscillation cycle for the highest frequency case investigated. While it is difficult to quantify this error in terms of the resulting pressure values, Section 4.5 provides a direct comparison with transducer measurements, as excellent agreement is observed.

Appendix B

Phase-resolved pressure Poisson equation derivation

This appendix provides a more thorough derivation of the phase-resolved pressure Poisson equation used in the proposed PIV pressure field mapping technique. The only assumption made in this model surround the governing equations is incompressible flow. The resulting continuity and Navier-Stokes equations are thus,

$$\frac{\partial u}{\partial x} + \frac{\partial v}{\partial y} = 0 \tag{B.1}$$

$$\rho \left(\frac{\partial u}{\partial t} + u \frac{\partial u}{\partial x} + v \frac{\partial u}{\partial y} \right) = -\frac{\partial p}{\partial x} + \mu \left(\frac{\partial^2 u}{\partial x^2} + \frac{\partial^2 u}{\partial y^2} \right) \tag{B.2}$$

$$\rho \left(\frac{\partial v}{\partial t} + u \frac{\partial v}{\partial x} + v \frac{\partial v}{\partial y} \right) = -\frac{\partial p}{\partial y} + \mu \left(\frac{\partial^2 v}{\partial x^2} + \frac{\partial^2 v}{\partial y^2} \right) \tag{B.3}$$

By taking the divergence of the Navier-Stokes equations (i.e $\frac{\partial}{\partial x}$ of Equation B.2 + $\frac{\partial}{\partial y}$ of

Equation B.3), the following can be determined,

$$-\left(\frac{\partial^2 p}{\partial x^2} + \frac{\partial^2 p}{\partial y^2}\right) = \rho\left[\frac{\partial}{\partial t}\left(\frac{\partial u}{\partial x} + \frac{\partial v}{\partial y}\right) + u\frac{\partial}{\partial x}\left(\frac{\partial u}{\partial x} + \frac{\partial v}{\partial y}\right) + v\frac{\partial}{\partial y}\left(\frac{\partial u}{\partial x} + \frac{\partial v}{\partial y}\right)\right]$$
$$+ \rho\left[\left(\frac{\partial u}{\partial x}\right)^2 + 2\frac{\partial u}{\partial y}\frac{\partial v}{\partial x} + \left(\frac{\partial v}{\partial y}\right)^2\right] - \mu\left[\frac{\partial^2}{\partial x^2}\left(\frac{\partial u}{\partial x} + \frac{\partial v}{\partial y}\right) + \frac{\partial^2}{\partial y^2}\left(\frac{\partial u}{\partial x} + \frac{\partial v}{\partial y}\right)\right] \quad \text{(B.4)}$$

Introducing Equation B.1 to Equation B.4 reveals the pressure Poisson equation,

$$-\nabla^2 p = \rho\left[\left(\frac{\partial u}{\partial x}\right)^2 + 2\frac{\partial u}{\partial y}\frac{\partial v}{\partial x} + \left(\frac{\partial v}{\partial y}\right)^2\right] \quad \text{(B.5)}$$

As discussed in Section 4.2, the velocity and pressure fields can be broken up into a steady mean component $(\overline{u_s})$, a periodic mean component $(\overline{u_t})$ and fluctuations away from this mean field (u'). Each of these components are depicted in Figure 4.6.

$$u = \overline{u} + u' = \overline{u_s} + \overline{u_t} + u' \quad \text{(B.6)}$$

$$v = \overline{v} + v' = \overline{v_s} + \overline{v_t} + v' \quad \text{(B.7)}$$

$$p = \overline{p} + p' = \overline{p_s} + \overline{p_t} + p' \quad \text{(B.8)}$$

Substituting these equations into Equation B.5 reveals,

$$-\nabla^2\overline{p} = \rho\left[\left(\frac{\partial\overline{u}}{\partial x}\right)^2 + 2\frac{\partial\overline{u}}{\partial y}\frac{\partial\overline{v}}{\partial x} + \left(\frac{\partial\overline{v}}{\partial y}\right)^2 + \left(\frac{\partial u'}{\partial x}\right)^2 + 2\frac{\partial u'}{\partial y}\frac{\partial v'}{\partial x} + \left(\frac{\partial v'}{\partial y}\right)^2\right] \quad \text{(B.9)}$$

The first three terms on the right hand side of Equation B.9 can be resolved by the PIV,

however the last three have to be rearranged first,

$$= \left(\frac{\partial u'}{\partial x}\right)^2 + 2\frac{\partial u'}{\partial y}\frac{\partial v'}{\partial x} + \left(\frac{\partial v'}{\partial y}\right)^2$$

$$= \left(\frac{\partial u'}{\partial x}\right)^2 + 2\frac{\partial u'}{\partial y}\frac{\partial v'}{\partial x} + \left(\frac{\partial v'}{\partial y}\right)^2 + u'\frac{\partial}{\partial x}\left(\frac{\partial u'}{\partial x} + \frac{\partial v'}{\partial y}\right) + v'\frac{\partial}{\partial y}\left(\frac{\partial u'}{\partial x} + \frac{\partial v'}{\partial y}\right)$$

$$= \left[\left(\frac{\partial u'}{\partial x}\right)^2 + u'\frac{\partial^2 u'}{\partial x^2}\right] + \left[\frac{\partial u'}{\partial y}\frac{\partial v'}{\partial x} + v'\frac{\partial^2 u}{\partial x \partial y}\right] + \left[\left(\frac{\partial v'}{\partial y}\right)^2 + v'\frac{\partial^2 v'}{\partial y^2}\right] + \left[\frac{\partial u'}{\partial y}\frac{\partial v'}{\partial x} + u'\frac{\partial^2 v}{\partial x \partial y}\right]$$

$$= \frac{\partial}{\partial x}\left[u'\frac{\partial u'}{\partial x} + v'\frac{\partial u'}{\partial y}\right] + \frac{\partial}{\partial y}\left[v'\frac{\partial v'}{\partial y} + u'\frac{\partial v'}{\partial x}\right]$$

$$\qquad\qquad + \frac{\partial}{\partial x}\left[u\left(\frac{\partial u'}{\partial x} + \frac{\partial v'}{\partial y}\right)\right] + \frac{\partial}{\partial y}\left[v\left(\frac{\partial u'}{\partial x} + \frac{\partial v'}{\partial y}\right)\right]$$

$$= \frac{\partial}{\partial x}\left[2u'\frac{\partial u'}{\partial x} + \left(u'\frac{\partial v'}{\partial y} + v'\frac{\partial u'}{\partial y}\right)\right] + \frac{\partial}{\partial y}\left[2v'\frac{\partial v'}{\partial y} + \left(u'\frac{\partial v'}{\partial x} + v'\frac{\partial u'}{\partial x}\right)\right]$$

$$= \frac{\partial^2 u'^2}{\partial x^2} + 2\frac{\partial^2 u'v'}{\partial x \partial y} + \frac{\partial^2 v'^2}{\partial y^2} \tag{B.10}$$

Introducing Equation B.10 to Equation B.9 and Reynolds averaging results in the phase-resolved form of the pressure Poisson equation,

$$-\nabla^2 \overline{p} = \rho\left[\left(\frac{\partial \overline{u}}{\partial x}\right)^2 + 2\frac{\partial \overline{u}}{\partial y}\frac{\partial \overline{v}}{\partial x} + \left(\frac{\partial \overline{v}}{\partial y}\right)^2 + \frac{\partial^2 u'^2}{\partial x^2} + 2\frac{\partial^2 u'v'}{\partial x \partial y} + \frac{\partial^2 v'^2}{\partial y^2}\right] \tag{B.11}$$

Appendix C

Influence of jet aspect ratio on opposing planar jet oscillations

While there does appear to be a clear trend between the amount of momentum transferred to the cross-stream direction and the Strouhal number, as shown in Figure 5.18, it is not clear what causes the increased spread for increasing jet aspect ratio. One possible explanation is the impact on the exit profiles of the jets caused by variation in the aspect ratio of the jets. However, Arthurs and Ziada (2012) reviewed the exit profiles for the jets used in the current investigation over the same range of aspect ratios and saw negligible variation in the jet characteristics. Furthermore, the impact of the aspect ratio is most apparent at larger impingement ratios, while variations in the jet exit profiles and the core length would be most pronounced at smaller impingement ratios. The length of the core has been measured for each of the cases listed in Table 5.1 and the length is consistently in the range of $2.3h$ to $2.9h$, which would not create enough variation to impact the Strouhal number to the extent observed.

Another possible explanation surrounds the shape of the exterior of the jet nozzles. As

previously discussed, the exterior of the nozzles is tapered such that the distance between the nozzle faces increases for cross-stream locations further from the jets' centerline. Tu *et al.* (2014a) investigated the effect of confinement by introducing a plate behind each jet exit and orienting it in the cross-stream direction. It is shown that introducing this confinement slightly decreased the oscillation frequency of the opposing planar jets. Similar observations are observed here as the aspect ratio is varied. For example, if the slot width, impingement distance and jet exit velocities are all increased together, the taper of the nozzles will effectively create less confinement behind the jet exits which is accompanied with an increase in the Strouhal number. However, Tu *et al.* (2014a) drastically varied the confinement from no boundary to a solid boundary immediately upstream of the jets and only observed a small variation in the Strouhal number ($\approx 15\%$). In the current investigation, the amount of confinement observed by the jets has only slightly increased as the aspect ratio decreased and a large variation in the Strouhal number is observed, as it is reduced by almost 50%. Therefore, while the nozzle shape may have a slight impact on the development and convection of the circulation zones, it is not likely to account for the majority of the observed variation in the Strouhal number of the oscillations.

A third possible explanation for the impact of the jet aspect ratio on the Strouhal number may arise from the three-dimensionality of the flow field, likely a result of increased three-dimensional behavior near the ends of the jets' span. While many authors have studied the aspect ratios and downstream distances over which free and impinging planar jets may be assumed to be two-dimensional, and this investigation is conducted well within this range, the opposing planar jets are a unique case. With the large variation in the stagnation pressure formed at impingement of the two jets, as well as the large deflection oscillations of the jets causing variation in the shape and orientation of the impingement plane, it is possible that

end effects may still be playing a significant role. However, even for the very large jet aspect ratios investigated in the current study, the Strouhal number does not appear to converge to a unified value. Furthermore, for smaller impingement ratios, where the three-dimensional effects are minimized, the location of the circulation zones is still significantly influenced by the aspect ratio of the jets. Therefore, it does not seem likely that the three-dimensionality of the flow field would cause such a drastic variation in the Strouhal number.

Finally, it does appear possible that the variation of the Strouhal number with the aspect ratio may be a physical phenomenon which exists in the two-dimensional flow field. The premise surrounds breaking the flow field into two separate components; the jet column containing the majority of the momentum of the flow and the circulation zones which drive the jet columns back and forth. It is possible that varying the aspect ratio of the jet will vary the percent of energy transferred to each of these regions of the flow. In particular, varying the aspect ratio, by for example varying the slot width, causes the momentum of the jet to scale accordingly. However, the flow dynamics of the circulation zones may not be significantly impacted as a result of the boundary conditions of this region largely remaining the same, with a high-speed flow on one side and quiescent fluid on the other. Therefore, it is possible that increasing the slot width, and thus decreasing the aspect ratio, will cause the momentum of the jet to increase significantly, while only a small increase in the energy transferred to the circulation zones will be observed. Thus, the low-pressure regions will be of similar strength and the increased momentum of the jet will cause the percent of momentum transferred to the cross-stream direction to be reduced. Consequently, the reduced momentum transfer will result in shorter oscillation periods, indicated by the observed higher Strouhal number. Nonetheless, while the variations in the Strouhal number and flow field dynamics are unique and help explain at least some of the discrepancy reported

in the literature, further investigations are required to determine if this is truly a physically two-dimensional phenomenon or another phenomenon is playing a role, such as the nozzle shape or three-dimensional effects.

Bibliography

Antonia, R., Browne, L., Rajagopalan, S., and Chambers, A. (1983). On the organized motion of a turbulent plane jet. *Journal of fluid mechanics*, **134**, 49–66.

Arthurs, D. and Ziada, S. (2012). Self-excited oscillations of a high-speed impinging planar jet. *Journal of Fluids and Structures*, **34**, 236–258.

Arthurs, D. and Ziada, S. (2014). Development of a feedback model for the self-excited impinging planar jet. In *Fluid-Structure-Sound Interactions and Control*, pages 39–44. Springer.

Auteri, F., Carini, M., Zagaglia, D., Montagnani, D., Gibertini, G., Merz, C., and Zanotti, A. (2015). A novel approach for reconstructing pressure from piv velocity measurements. *Experiments in Fluids*, **56**(2), 45.

Bajaj, A. and Garg, V. (1977). Linear stability of jet flows. *Journal of Applied Mechanics*, **44**(3), 378–384.

Baur, T. and Kongeter, J. (1999). Piv with high temporal resolution for the determination of local pressure reductions from coherent turbulence phenomena. *3rd Int. Workshop on Particle Image Velocimetry (Santa Barbara)*.

Brown, G. L. and Roshko, A. (1974). On density effects and large structure in turbulent mixing layers. *Journal of Fluid Mechanics*, **64**(04), 775–816.

Charonko, J. J., King, C. V., Smith, B. L., and Vlachos, P. P. (2010). Assessment of pressure field calculations from particle image velocimetry measurements. *Measurement Science and technology*, **21**(10), 105401.

Crighton, D. (1992). The jet edge-tone feedback cycle; linear theory for the operating stages. *Journal of Fluid Mechanics*, **234**, 361–391.

Crow, S. C. and Champagne, F. (1971). Orderly structure in jet turbulence. *J. Fluid Mech*, **48**(3), 547–591.

Dabiri, J. O., Bose, S., Gemmell, B. J., Colin, S. P., and Costello, J. H. (2014). An algorithm to estimate unsteady and quasi-steady pressure fields from velocity field measurements. *Journal of Experimental Biology*, pages jeb–092767.

de Gortari, J. C. and Goldschmidt, V. (1981). The apparent flapping motion of a turbulent plane jet—further experimental results. *Journal of Fluids Engineering*, **103**(1), 119–126.

de Kat, R. and Ganapathisubramani, B. (2012). Pressure from particle image velocimetry for convective flows: a taylor's hypothesis approach. *Measurement Science and Technology*, **24**(2), 024002.

De Kat, R. and Van Oudheusden, B. (2012). Instantaneous planar pressure determination from piv in turbulent flow. *Experiments in fluids*, **52**(5), 1089–1106.

Denshchikov, V., Kondrat'ev, V., and Romashov, A. (1978). Interaction between two opposed jets. *Fluid Dynamics*, **13**(6), 924–926.

Denshchikov, V., Kondrat'Ev, V., Romashov, A., and Chubarov, V. (1983). Auto-oscillations of planar colliding jets. *Fluid Dynamics*, **18**(3), 460–462.

Deo, R. C., Mi, J., and Nathan, G. J. (2007). The influence of nozzle aspect ratio on plane jets. *Experimental thermal and fluid science*, **31**(8), 825–838.

Freymuth, P. (1966). On transition in a separated laminar boundary layer. *Journal of Fluid Mechanics*, **25**(04), 683–704.

Fujisawa, N., Tanahashi, S., and Srinivas, K. (2005). Evaluation of pressure field and fluid forces on a circular cylinder with and without rotational oscillation using velocity data from piv measurement. *Measurement Science and Technology*, **16**(4), 989.

Ghaemi, S., Ragni, D., and Scarano, F. (2012). Piv-based pressure fluctuations in the turbulent boundary layer. *Experiments in fluids*, **53**(6), 1823–1840.

Goldschmidt, V. and Bradshaw, P. (1973). Flapping of a plane jet. *Physics of Fluids (1958-1988)*, **16**(3), 354–355.

Goldschmidt, V., Moallemi, M., and Oler, J. (1983). Structures and flow reversal in turbulent plane jets. *Physics of Fluids (1958-1988)*, **26**(2), 428–432.

Gurka, R., Liberzon, A., Hefetz, D., Rubinstein, D., and Shavit, U. (1999). Computation of pressure distribution using piv velocity data. In *Workshop on particle image velocimetry*, volume 2.

Gutmark, E. and Ho, C.-M. (1983). Preferred modes and the spreading rates of jets. *Physics of Fluids (1958-1988)*, **26**(10), 2932–2938.

Hassaballa, M. and Ziada, S. (2015). Self-excited oscillations of two opposing planar air jets. *Physics of Fluids (1994-present)*, **27**(1), 014109.

Ho, C.-M. and Hsiao, F. (1983). Evolution of coherent structures in a lip jet. *Structure of Complex Turbulent Shear Flow*, pages 121–136.

Ho, C.-M. and Huerre, P. (1984). Perturbed free shear layers. *Annual Review of Fluid Mechanics*, **16**(1), 365–422.

Ho, C.-M. and Nosseir, N. S. (1981). Dynamics of an impinging jet. part 1. the feedback phenomenon. *Journal of Fluid Mechanics*, **105**, 119–142.

Holger, D. K., Wilson, T. A., and Beavers, G. S. (1977). Fluid mechanics of the edgetone. *The Journal of the Acoustical Society of America*, **62**(5), 1116–1128.

Holger, D. K., Wilson, T. A., and Beavers, G. S. (1980). The amplitude of edgetone sound. *The Journal of the Acoustical Society of America*, **67**(5), 1507–1511.

Husain, Z. and Hussain, A. (1983). Natural instability of free shear layers. *AIAA journal*, **21**(11), 1512–1517.

Hussain, A. and Zaman, K. (1978). The free shear layer tone phenomenon and probe interference. *Journal of Fluid Mechanics*, **87**(02), 349–383.

Imaichi, K. and Ohmi, K. (1983). Numerical processing of flow-visualization pictures–measurement of two-dimensional vortex flow. *Journal of Fluid Mechanics*, **129**, 283–311.

Jakobsen, M., Dewhirst, T., and Greated, C. (1997). Particle image velocimetry for predictions of acceleration fields and force within fluid flows. *Measurement Science and Technology*, **8**(12), 1502.

Jensen, A. and Pedersen, G. K. (2004). Optimization of acceleration measurements using piv. *Measurement Science and Technology*, **15**(11), 2275.

Johnson, D. A. and Wood, P. E. (2000). Self-sustained oscillations in opposed impinging jets in an enclosure. *The Canadian Journal of Chemical Engineering*, **78**(5), 867–875.

Kaykayoglu, R. and Rockwell, D. (1986a). Unstable jet–edge interaction. part 1. instantaneous pressure fields at a single frequency. *Journal of Fluid Mechanics*, **169**, 125–149.

Kaykayoglu, R. and Rockwell, D. (1986b). Unstable jet–edge interaction part 2: Multiple frequency pressure fields. *Journal of Fluid Mechanics*, **169**, 151–172.

Kim, S. J., Cho, J. W., Ahn, K. J., and Chung, M. K. (2003). Numerical analysis of edge over-coating in continuous hot-dip galvanizing. *ISIJ international*, **43**(10), 1495–1501.

Kostiuk, L., Bray, K., and Cheng, R. (1993a). Experimental study of premixed turbulent combustion in opposed streams. part ii—reacting flow field and extinction. *Combustion and flame*, **92**(4), 396–409.

Kostiuk, L., Bray, K., and Cheng, R. (1993b). Experimental study of premixed turbulent combustion in opposed streams. part i—nonreacting flow field. *Combustion and flame*, **92**(4), 377–395.

Kudra, T. and Mujumdar, A. S. (2009). *Advanced drying technologies*. CRC Press.

Li, W.-F., Yao, T.-L., Liu, H.-F., and Wang, F.-C. (2011). Experimental investigation of flow regimes of axisymmetric and planar opposed jets. *AIChE Journal*, **57**(6), 1434–1445.

Li, W.-F., Huang, G.-F., Tu, G.-Y., Liu, H.-F., and Wang, F.-C. (2013). Experimental study

of planar opposed jets with acoustic excitation. *Physics of Fluids (1994-present)*, **25**(1), 014108.

Lin, C.-K., Hsiao, F.-B., and Sheu, S.-S. (1993). Flapping motion of a planar jet impinging on a v-shaped plate. *Journal of aircraft*, **30**(3), 320–325.

Lin, J.-C. and Rockwell, D. (2001). Oscillations of a turbulent jet incident upon an edge. *Journal of fluids and structures*, **15**(6), 791–829.

Liu, X. and Katz, J. (2006). Instantaneous pressure and material acceleration measurements using a four-exposure piv system. *Experiments in Fluids*, **41**(2), 227.

Lucas, M. and Rockwell, D. (1984). Self-excited jet: upstream modulation and multiple frequencies. *Journal of Fluid Mechanics*, **147**, 333–352.

Lucas, M. J., Noreen, R., Southerland, L., Cole III, J., and Junger, M. (1995). The acoustic characteristics of turbomachinery cavities.

McClure, J. and Yarusevych, S. (2017). Optimization of planar piv-based pressure estimates in laminar and turbulent wakes. *Experiments in Fluids*, **58**(5), 62.

Melling, A. (1997). Tracer particles and seeding for particle image velocimetry. *Measurement Science and Technology*, **8**(12), 1406.

Murai, Y., Nakada, T., Suzuki, T., and Yamamoto, F. (2007). Particle tracking velocimetry applied to estimate the pressure field around a savonius turbine. *Measurement Science and Technology*, **18**(8), 2491.

Murray, N., Ukeiley, L., and Raspet, R. (2007). Calculating surface pressure fluctuations

from piv data using poisson's equation. In *45th AIAA Aerospace Sciences Meeting and Exhibit*, page 1306.

Nosseir, N. S. and Ho, C.-M. (1982). Dynamics of an impinging jet. part 2. the noise generation. *Journal of fluid mechanics*, **116**, 379–391.

Orr, W. M. (1907a). The stability or instability of the steady motions of a perfect liquid and of a viscous liquid. part i: A perfect liquid. In *Proceedings of the Royal Irish Academy. Section A: Mathematical and Physical Sciences*, volume 27, pages 9–68. JSTOR.

Orr, W. M. (1907b). The stability or instability of the steady motions of a perfect liquid and of a viscous liquid. part ii: A viscous liquid. In *Proceedings of the Royal Irish Academy. Section A: Mathematical and Physical Sciences*, volume 27, pages 69–138. JSTOR.

Pan, Z., Whitehead, J., Thomson, S., and Truscott, T. (2016). Error propagation dynamics of piv-based pressure field calculations: How well does the pressure poisson solver perform inherently? *Measurement Science and Technology*, **27**(8), 084012.

Pawlowski, R., Salinger, A., Shadid, J., and Mountziaris, T. (2006). Bifurcation and stability analysis of laminar isothermal counterflowing jets. *Journal of Fluid Mechanics*, **551**, 117–139.

Powell, A. (1961). On the edgetone. *The Journal of the Acoustical Society of America*, **33**(4), 395–409.

Ragni, D., Van Oudheusden, B., and Scarano, F. (2012). 3d pressure imaging of an aircraft propeller blade-tip flow by phase-locked stereoscopic piv. *Experiments in fluids*, **52**(2), 463–477.

Rayleigh, L. (1880). On the stability, or instability, of certain fluid motions. *Proc. London Math. Soc.*, **11**, 57.

Rockwell, D. (1983). Oscillations of impinging shear layers. *AIAA journal*, **21**(5), 645–664.

Rockwell, D. (1998). Vortex-body interactions. *Annual review of fluid mechanics*, **30**(1), 199–229.

Rockwell, D. and Naudascher, E. (1979). Self-sustained oscillations of impinging free shear layers. *Annual Review of Fluid Mechanics*, **11**(1), 67–94.

Santos, R. J. and Sultan, M. A. (2013). State of the art of mini/micro jet reactors. *Chemical Engineering & Technology*, **36**(6), 937–949.

Santos, R. J., Teixeira, A. M., and Lopes, J. C. B. (2005). Study of mixing and chemical reaction in rim. *Chemical Engineering Science*, **60**(8), 2381–2398.

Sathapornprasath, K., Devahastin, S., and Soponronnarit, S. (2007). Performance evaluation of an impinging stream dryer for particulate materials. *Drying Technology*, **25**(6), 1111–1118.

Sato, H. (1960). The stability and transition of a two-dimensional jet. *Journal of Fluid Mechanics*, **7**(01), 53–80.

Scarano, F. and Riethmuller, M. L. (2000). Advances in iterative multigrid piv image processing. *Experiments in Fluids*, **29**(1), S051–S060.

Sommerfield, A. (1908). Ein beitrag zur hydrodynamischen erklarung der turbulenten flussigkeisbewegung. *Atti Congr. Int. Math. 4th.*

Staubli, T. and Rockwell, D. (1987). Interaction of an unstable planar jet with an oscillating leading edge. *Journal of fluid mechanics*, **176**, 135–167.

Tamir, A. (2014). *Impinging-stream reactors: fundamentals and applications*. Elsevier.

Tesař, V. (2009). Oscillator micromixer. *Chemical Engineering Journal*, **155**(3), 789–799.

Thomas, F. and Goldschmidt, V. (1986). Structural characteristics of a developing turbulent planar jet. *Journal of Fluid Mechanics*, **163**, 227–256.

Tu, G., Li, W., Du, K., Huang, G., and Wang, F. (2014a). Onset and influencing factors of deflecting oscillation in planar opposed jets. *Chemical Engineering Journal*, **247**, 125–133.

Tu, G.-y., Li, W.-f., Du, K.-j., and Wang, F.-c. (2014b). Experimental investigation of deflecting oscillation in t-jets reactor. *Chemical Engineering Science*, **116**, 734–744.

Van Oudheusden, B. (2013). Piv-based pressure measurement. *Measurement Science and Technology*, **24**(3), 032001.

Villegas, A. and Diez, F. (2014). Evaluation of unsteady pressure fields and forces in rotating airfoils from time-resolved piv. *Experiments in fluids*, **55**(4), 1697.

Violato, D., Moore, P., and Scarano, F. (2011). Lagrangian and eulerian pressure field evaluation of rod-airfoil flow from time-resolved tomographic piv. *Experiments in fluids*, **50**(4), 1057–1070.

Walker, J., Smith, C., Cerra, A., and Doligalski, T. (1987). The impact of a vortex ring on a wall. *Journal of Fluid Mechanics*, **181**(1), 99–140.

Wang, F., Zhou, Z., Dai, Z., Gong, X., Yu, G., Liu, H., Wang, Y., and Yu, Z. (2007). Development and demonstration plant operation of an opposed multi-burner coal-water

slurry gasification technology. *Frontiers of Energy and Power Engineering in China*, **1**(3), 251–258.

Ziada, S. (1995). Feedback control of globally unstable flows: impinging shear flows. *Journal of Fluids and Structures*, **9**(8), 907–923.

Ziada, S. and Rockwell, D. (1982a). Oscillations of an unstable mixing layer impinging upon an edge. *Journal of fluid mechanics*, **124**, 307–334.

Ziada, S. and Rockwell, D. (1982b). Vortex–leading-edge interaction. *Journal of Fluid Mechanics*, **118**, 79–107.